

MASTER THESIS

Calibration methods for material measurements

Department of Electrical and Information Technology, Faculty of
Engineering, LTH, Lund University SE-221 00 Lund, Sweden



LUND
UNIVERSITY

Author:
CHRISTIAN NELSON

Supervisors:
DANIEL SJÖBERG
CHRISTER LARSSON

February 1, 2016

Abstract

This master thesis investigates different algorithms that can be used to calibrate a vector network analyzer (VNA). These methods are possibly a good alternative when altering the measurement setup by inserting standards or moving the ports is difficult or not even a possibility.

Measurements with a VNA at microwave frequencies most often result in a scattering matrix. As no actual setup was available, simulations were carried out. These matrices contain the data that the algorithms will use to compensate for the errors in the setup, e.g. phase shift due to propagation and power loss due to imperfect connections.

The simulations of three different setups were performed using the commercial software COMSOL Multiphysics. The setups that were simulated were: a parallel plate waveguide, a straight coaxial fixture, and a tapered coaxial fixture. The parallel plate waveguide is a big setup (1 m \times 1.5 m) compared to the wavelengths that were simulated (0.015 to 0.30 m), thus making the problem difficult to solve. Due to the amount of memory needed during calculations, only a simplified 2D model was built. For the coaxial fixtures, full 3D simulations were performed.

Three different algorithms were implemented; LNN (Line-Network-Network), Extended LNN, and TTN (Through-Through-Network). The methods are self-calibration methods, which means that the device under test (DUT) can be used as one of the calibration standards. All three methods assume that the DUT is symmetric and reciprocal. The first algorithm that was implemented and examined was the LNN method. This method places the DUT at three different positions in the setup. The separations l_1 and l_2 between these positions must be equal, i.e. $l_1 = l_2$. The second algorithm implemented was the Extended LNN. This method allows $l_1 \neq l_2$ which makes the method less sensitive for misplacement of the calibration network. The last method to be investigated was the TTN. This method should be the easiest to perform since the three measurements that need to be done are relatively simple. However, this simplicity comes with a price: the setup has to be fairly long and has to have a very flat frequency response.

Next the Nicolson-Ross-Weir (NRW) algorithm was applied to the calibrated scattering matrix. The NRW calculates the material parameters ϵ_r and μ_r .

When all the algorithms had been implemented and tested, different errors (random errors, wrong guesses, noise) were injected to try the stability of the different methods.

All methods look promising and some of the intrinsic difficulties of the algorithms seem fairly easy to work around. For the LNN and Extended LNN, the length of the measurement setup does not play a big role which implies that these methods can be used in small fixtures. The TTN has the drawback that the length of the setup has to be quite long. Since this method is most suitable for free space measurements, where the antennas are often placed at a fixed distance from each other, the length constraint should not be a significant practical problem.

Contents

Abstract	i
Table of Contents	iii
Acknowledgments	v
1 Introduction	1
1.1 Background	1
1.2 Scope	3
1.3 Goal	3
1.4 Approach	3
2 Electromagnetic Fields and Microwave Theory	5
2.1 Maxwell's equations	5
2.2 Guided waves	10
2.3 2-port networks	14
3 Errors and calibration	17
3.1 Network Analyzers	17
3.2 Error sources and error coefficients	17
3.3 Random noise	21
4 Extraction of the material parameters, ϵ_r and μ_r	23
4.1 The Nicolson-Ross-Weir Algorithm	23
5 The algorithms	27
5.1 Calibration standards	27
5.2 Line-Network-Network	28
5.3 Extended Line-Network-Network	30
5.4 Through-Through-Network	32
5.5 Choosing signs	34
6 Computer simulation models	35
6.1 Parallel plate waveguide	35
6.2 Tapered coaxial fixture	39
6.3 Straight coaxial cable	40
7 Simulated samples	41
8 NRW applied on scattering parameters	43
9 Results and discussion	45
9.1 General	45
9.2 LNN and Extended LNN	46
9.3 TTN	48
9.4 Statistics	49

9.5	Discussion of the self-calibrations	51
9.6	Post calibration DUT	52
9.7	Conclusions	53
Bibliography		54
A LNN		59
A.1	Straight coaxial cable or fixture	59
A.2	Tapered coaxial cable	62
A.3	Parallel plates	65
B Extended LNN		69
B.1	Straight coaxial cable or fixture	69
B.2	Tapered coaxial cable	72
B.3	Parallel plates	75
C TTN		79
C.1	Straight coaxial cable or fixture	79
C.2	Tapered coaxial cable	82
C.3	Parallel plates	84

Acknowledgments

This project was carried out at the department of electrical- and information technology at Lund University. First I would give my sincerest appreciation to my supervisors; Professor Daniel Sjöberg at Lund University and to adjunct Professor Christer Larsson at SAAB. You have inspired me to work hard and to treat every challenge or problem as an opportunity to learn something new. I would also like to extend a big thank you to M.Sc. Andreas Ericsson for his encouragement and our long discussions on the subject. Finally a thank you to everyone who have provided me with feedback, it has been invaluable.

1

Introduction

1.1 Background

A vector network analyzer (VNA, picture in Figure 1.1) is a tool for measuring network parameters of an electrical network, such as a material or an electronic device, for which an electromagnetic wave is to propagate through. The first commercial network analyzers were developed at Hewlett-Packard (HP) in the 1960's [1, 2]. The VNA was first mentioned in 1968 in [3], when it was called an automatic network analyzer (ANA). Two years later, HP introduced the first commercial ANA, HP Model 8540A/8542A [4]. It could perform measurements from 0.11 GHz up to 12.4 GHz, or 18 GHz with a frequency-stabilized signal source. At present time it is possible to buy a VNA (from e.g. Keysight Technologies) that can measure at a frequency as low as 5 Hz or at frequencies just over 1 THz.



Figure 1.1: Agilent Technologies N5245A PNA-X vector network analyzers. Used with permission under the public domain [5].

The result of a measurement with a VNA is most often the so called scattering matrix [6,7], which is a mathematical description of a material or a device (also called a network). The matrix contains information about how much of an incident wave is reflected back and how much propagates through the sample and is transmitted. It is a complete description of a network and contains information about amplitude and phase of the wave.

There are many occasions when a VNA is a useful tool, e.g. when measuring reflection and transmission of a device under test, from which the material parameters ϵ_r and μ_r can be extracted [8–16].

A VNA is often used to verify the construction of metamaterials or other electronic devices, e.g. [17–21]. All these cases have in common the investigation of the behavior of a network at high frequencies.

Using waveguides (e.g. coaxial cables and rectangular waveguides) one can sustain and guide the propagating wave from the VNA to a material or device on which a measurement is to be carried out. Imperfections in e.g. the connections will reflect parts of the wave back to the VNA. The phase shift from the wave propagating in the waveguides is also an error that has to be taken into account. All these errors will affect the result of the measurement (cf. left Figure 1.2).

To get rid of these errors in the measurement setup, and obtain the correct scattering matrix, a calibration has to be done [22–26], cf. Figure 1.2 where the left plot shows the uncalibrated scattering parameters and the right plot shows the scattering parameters after a calibration have been performed. The purpose of a calibration is to remove errors from the measurement. This is achieved by measuring on networks with a known response, like an (almost) ideal reflection, or an extra line with known length.

There already exists well known calibration techniques, like the TRL (Through-Reflect-Line) [27] and the SOLT (Short-Open-Load-Through) [23]. All of these assume that the measurement setup can be modified during calibration, e.g. the ability to extend the setup with an additional coaxial cable or connecting the ports directly to each other. Sometimes it is not possible to move the different parts, e.g. when two horn antennas are used as ports and are positioned at a fixed distance from one another. Another drawback of these established calibration methods is that the standards that are going to be used during calibration have to be very well-known and of very high quality, which often leads to expensive parts.

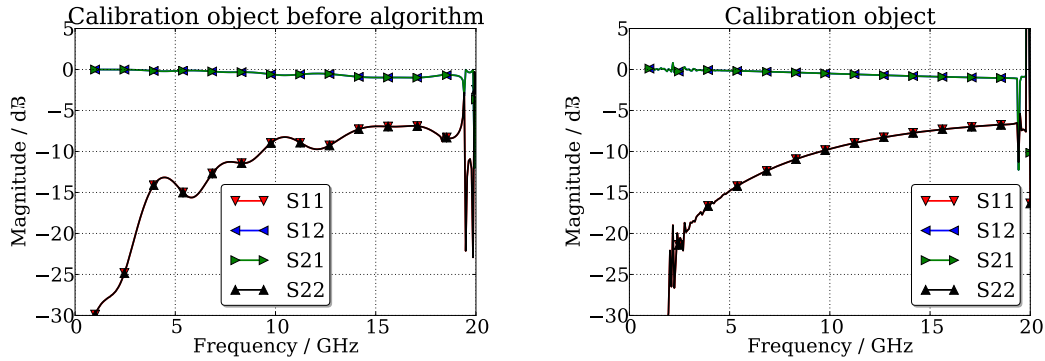


Figure 1.2: The scattering parameters for a slab. The left shows uncalibrated scattering parameters and on the right calibrated scattering parameters.

1.2 Scope

A VNA is used to measure the scattering parameters of a material slab, placed at different locations between two antennas with fixed positions, hence earlier mentioned calibration methods are not an option for this setup. This thesis presents three methods which implement self-calibration, i.e. the DUT/MUT (Device/Material Under Test) is one of the standards. Other standards used in this project are Line and Through. With the use of these three standards one eliminates the need for expensive well-known standards. Intrinsic for all methods is redundancy of information which leads to that all the standards do not have to be exactly known since they will be characterized during calibration [26].

Despite the redundancy, these methods do require certain a-priori knowledge since some of the equations that are obtained are of second order and thus signs have to be chosen. The a-priori knowledge can be information like the approximate refractive index of the sample, or if the material has magnetic properties etc.

1.3 Goal

The aim of this thesis is to investigate three self-calibration methods which can be used in situations when methods like TRL and SOLT can not be performed. The studied algorithms are; LNN (Line-Network-Network) [28–30], Extended LNN [30,31], and TTN (Through-Through-Network) [32]. The goal is to compare the different methods to check if any of them is more stable than another in different setups. It will also be investigated how important the a-priori knowledge is for the end result. After the investigated calibration algorithm has been applied to the measured or simulated data, the material parameters of the slab will be extracted.

1.4 Approach

Unfortunately there were no possibility to perform scattering measurements on a real material slab, hence the first part of the thesis was to perform simulations of different setups using the commercial program COMSOL, which uses a finite element method (FEM) [33] solver. There exist several different numerical methods to solve Maxwell's equations. Others are e.g. the FDTD (Finite Difference Time Domain) [34] and MoM

(Method of Moments) [35]. This thesis will not go in to detail how the exact methods work, but since they all use the exact formulation of Maxwell's equations they can be rather time consuming, of course depending on the problem at hand. Since numerical methods were not the main topic of this thesis, neither were the aspect of optimizing the simulation time, the choice to use COMSOL and hence FEM was that it was readily available and was a familiar framework.

A COMSOL simulation can generate a Touchstone file [36, 37] which contain the scattering parameters for all the simulated frequencies. Then the three algorithms (LNN, Extended LNN, and TTN) were implemented with python, where the Touchstone files are used as input. Different python modules (packages) were used to simplify the implementation e.g. `scipy` [38] and `scikit-rf` [39]. To induce error in the simulations, random errors were added to scattering matrices. The implementation could have been done in any other programming language for instance Matlab. The reason python was used, except the obvious reason that it is free, is the availability of good modules like `scikit-rf` which loads Touchstone files out of the box and it models electrical networks. `Scikit-rf` also have an implemented calibration routine which is easy to apply that extracts all the error coefficients.

2

Electromagnetic Fields and Microwave Theory

In this chapter the theory needed in this thesis is explained briefly. Some basic electromagnetic theory of Maxwell's equations in free space and in a dielectric medium is covered. This leads to the discussion of constitutive relations and the definition of the relative permittivity (ϵ_r) and relative permeability (μ_r) which are two key concepts in this thesis.

A discussion on guided waves is presented to reach a basic understanding of how waves can be controlled. Waveguide theory is a subject that is not studied in detail in this thesis, but an understanding of how waveguides work is important in this context.

When working with microwaves the concept of 2-port networks is a very helpful tool. The definition of a 2-port network is explained, and then different ways to characterize or describe networks are discussed, e.g. the scattering matrix. The vector network analyzer, is the tool used for measurements of the scattering matrix. The importance of calibration and control over the reference planes are described. A more complete discussion about these subjects can be found in other literature e.g. [40–43].

The Nicolson-Ross-Weir (NRW) algorithm is explained since it is used to extract the material properties from the scattering parameters (measured or simulated). Care needs to be taken when using the algorithm due to analytical instabilities and this problem is going to be discussed.

2.1 Maxwell's equations

The electromagnetic interaction is one of the four fundamental interactions in nature; the other three are the weak force, the strong force, and gravitation [42]. The interaction is described by Maxwell's equations which are the partial differential equations that describes phenomena on a macroscopic scale. Today it is known that these equations are a good approximation to the more recent Quantum Electro Dynamics (QED) developed in the 1940s. The deviations only get significant when discussing the interaction of a few photons (the electromagnetic force carriers). For the purpose of this thesis we only need to consider the usual Maxwell's equations.

Electromagnetic waves exist all around us, in telecommunication (TV, WiFi, cellular

phones etc.), kitchens (microwave ovens) and in nature as light and lightning just to name a few examples. The theory was developed during the 19th century by different physicists and mathematicians including Faraday, Ampère, Hertz, Gauss and finally Maxwell. The equations in strong form are [44, p. 273]:

$$\nabla \times \mathbf{E}(\mathbf{r}, t) = \frac{-\partial \mathbf{B}(\mathbf{r}, t)}{\partial t}, \quad \text{Faraday's law} \quad (2.1a)$$

$$\nabla \times \mathbf{H}(\mathbf{r}, t) = \frac{\partial \mathbf{D}(\mathbf{r}, t)}{\partial t} + \mathbf{J}(\mathbf{r}, t), \quad \text{Ampère's law with corrections} \quad (2.1b)$$

$$\nabla \cdot \mathbf{D}(\mathbf{r}, t) = \rho(\mathbf{r}, t), \quad \text{Gauss' law} \quad (2.1c)$$

$$\nabla \cdot \mathbf{B}(\mathbf{r}, t) = 0. \quad (2.1d)$$

Here, the vector fields \mathbf{E} , \mathbf{H} , \mathbf{D} , \mathbf{B} , \mathbf{M} , \mathbf{J} and the scalar field ρ are

\mathbf{E} is the electric field, [V/m]

\mathbf{H} is the magnetic field, [A/m]

\mathbf{D} is the electric flux density, [As/m²]

\mathbf{B} is the magnetic flux density, [Vs/m²]

\mathbf{J} is the electric current density, [A/m²]

ρ is the electric charge density, [As/m³]

The electric charge density ρ is related to the electric current density \mathbf{J} through the law of conservation of charges. It is a fundamental assumption in physics that electric charges can not be destroyed or created, i.e. the sum of all charges will always be constant. With mathematics it is expressed as

$$\nabla \cdot \mathbf{J}(\mathbf{r}, t) + \frac{\partial \rho(\mathbf{r}, t)}{\partial t} = 0. \quad (2.2)$$

A magnetic current density does not exist since there have been no proof of the existence of magnetic charges (ρ_m) in nature [44, p. 273]. But sometimes it is a good mathematical tool to introduce when for example calculating excitation of fields in waveguides. Assuming that \mathbf{J} is known, the four vector quantities \mathbf{E} , \mathbf{D} , \mathbf{B} and \mathbf{H} yield one unknown for each spatial direction, thus resulting in a total of 12 unknowns. But they only contain 6 different scalar equations, i.e. right now the system of equations (2.1) is under-determined.

Since no magnetic monopoles exist in nature the source to all the electromagnetic fields are the electric current density and the electric charge density. Hence, the real source for the magnetic field is a loop of electric current and not a current of magnetic charges [42].

2.1.1 Waves solving Maxwell's equations

Before solving the problem of the under-determined system, (2.1), a brief discussion is needed to simplify the solution of the system for time harmonic signals. It is known that

the solution to Maxwell's equations consists of waves. There are different types of waves that solve the equations but in this thesis we consider time-harmonic plane waves. When assuming time-harmonic waves we can express the fields in phasor-notation:

$$\mathbf{E}(\mathbf{r}, t) = \text{Re}\{\mathbf{E}(\mathbf{r}, \omega) e^{j\omega t}\}, \quad (2.3)$$

with

$$\mathbf{E}(\mathbf{r}, \omega) = \sum_{n=1}^3 \hat{\mathbf{u}}_n A_n(\mathbf{r}, \omega) e^{j\phi_n(\mathbf{r}, \omega)}, \quad (2.4)$$

where $\hat{\mathbf{u}}_n$ are the coordinate unit vectors (e.g. $\hat{\mathbf{x}}$, $\hat{\mathbf{y}}$, and $\hat{\mathbf{z}}$), A_n is the amplitude which can depend on both the location \mathbf{r} and the frequency ω , and ϕ_n is the phase.

2.1.2 Constitutive relations

To solve the under-determined system (2.1), constitutive relations must be introduced. It relates two pairs of fields, e.g. [43]

$$\begin{Bmatrix} \mathbf{B} \\ \mathbf{D} \end{Bmatrix} = \mathbf{F} \left(\begin{Bmatrix} \mathbf{H} \\ \mathbf{E} \end{Bmatrix} \right). \quad (2.5)$$

In free space it takes the form,

$$\mathbf{B}(\mathbf{r}, t) = \mu_0 \mathbf{H}(\mathbf{r}, t), \quad (2.6a)$$

$$\mathbf{D}(\mathbf{r}, t) = \epsilon_0 \mathbf{E}(\mathbf{r}, t), \quad (2.6b)$$

with (where $c_0 = 1/\sqrt{\epsilon_0 \mu_0}$ is the speed of light in vacuum)

$$\mu_0 = 4\pi \cdot 10^{-7} \text{ Vs/Am}$$

$$\epsilon_0 = 1/(c_0^2 \mu_0) \approx 8.854 \cdot 10^{-12} \text{ As/Vm}.$$

In this section we work with phasor representation of the waves that was introduced in section 2.1.1. The reason for this is that the material has a "memory" and this is represented with a convolution in the constitutive relations in the time domain. But the Fourier transform of a convolution is just the product of each function's Fourier transform in the frequency domain. This makes modeling of material properties much easier.

The building blocks of a material are its atoms or molecules. These will be affected by an applied external electric field. The heavy nucleus will remain relatively unchanged but the much lighter electron cloud will slightly change its position relative the nucleus and thus induce an electric dipole moment that will increase the total displacement flux \mathbf{D} .

This is called the *electrical polarization* of the material and it is described by \mathbf{P} . The relation between \mathbf{D} and \mathbf{E} takes the form:

$$\mathbf{D}(\mathbf{r}, \omega) = \epsilon_0 \mathbf{E}(\mathbf{r}, \omega) + \mathbf{P}(\mathbf{r}, \omega). \quad (2.7)$$

The vectors \mathbf{D} and \mathbf{E} do not need to be parallel (isotropic) nor linear in a material. The non-linearity is often not a problem since these effects require a quite high field intensity

(e.g. in lasers). In a linear medium the electric polarization is related to the electric field through

$$\mathbf{P} = \epsilon_0 \chi_e \mathbf{E}, \quad (2.8)$$

where χ_e is called the *electric susceptibility* and is a complex tensor of rank 2 i.e. a 3×3 matrix in this case. Inserting (2.8) into (2.7) yields the matrix multiplication

$$\mathbf{D} = \epsilon \mathbf{E} \quad (2.9)$$

with

$$\epsilon = \epsilon_0 (\mathbf{I} + \chi_e) = \epsilon_0 \epsilon_r = \epsilon_0 (\epsilon'_r - j\epsilon''_r). \quad (2.10)$$

On matrix form it looks as follows

$$\begin{pmatrix} D_x \\ D_y \\ D_z \end{pmatrix} = \begin{pmatrix} \epsilon_{xx} & \epsilon_{xy} & \epsilon_{xz} \\ \epsilon_{yx} & \epsilon_{yy} & \epsilon_{yz} \\ \epsilon_{zx} & \epsilon_{zy} & \epsilon_{zz} \end{pmatrix} \begin{pmatrix} E_x \\ E_y \\ E_z \end{pmatrix}. \quad (2.11)$$

The anisotropic property is due to the structure of the material at a microscopic level, and in this case the different elements of the tensor can take different values. But materials that are independent of orientation and thus have the same properties no matter how the wave enters the material, are called isotropic. Then the tensor becomes diagonal with the same value at all three positions.

$$\epsilon = \begin{pmatrix} \epsilon & 0 & 0 \\ 0 & \epsilon & 0 \\ 0 & 0 & \epsilon \end{pmatrix} = \epsilon_0 \epsilon_r \begin{pmatrix} 1 & 0 & 0 \\ 0 & 1 & 0 \\ 0 & 0 & 1 \end{pmatrix} \quad (2.12)$$

which leads to (notice that ϵ_r now is a complex number)

$$\mathbf{D} = \epsilon_0 \epsilon_r \mathbf{E}. \quad (2.13)$$

It is this *relative permittivity*, ϵ_r , that this project aims to extract from scattering measurements on different materials. In equation 2.10 it is easily seen that ϵ_r can be complex. The imaginary part represents the losses (heating) in the material due to the damping of the oscillations of the dipoles.

For magnetic fields the analogy holds, i.e. if a material has magnetic properties the atoms or molecules that exhibit a magnetic dipole moment will try to align themselves with an external applied magnetic field. This creates a *magnetic polarization* (or *magnetization*) \mathbf{M} . In a linear and isotropic situation the constitutive relation takes the form

$$\mathbf{B} = \mu_0 (\mathbf{H} + \mathbf{M}) \quad (2.14)$$

with

$$\mathbf{M} = \chi_m \mathbf{H}. \quad (2.15)$$

Combining (2.14) and (2.15) yields

$$\mathbf{B} = \mu_0 (1 + \chi_m) \mathbf{H} = \mu_0 \mu_r \mathbf{H} = \mu \mathbf{H}. \quad (2.16)$$

Similarly, it is the *relative permeability*, μ_r , that we aim to characterize.

2.1.3 Boundary conditions

With the constitutive relations we almost have a complete system of equations. The missing ingredients are the boundary conditions. Even when the fields are calculated in free space, there exist boundaries. In the case of free space the boundary describes what happens in infinity. The boundaries can not be described arbitrarily. Either the potential or the charge distribution, i.e. the normal derivative of the field, is known at the boundary.

A proper set of boundary conditions (see Figure 2.1) can fully describe a certain (macroscopic) situation and it can be shown that the solution is unique (which is a nontrivial mathematical problem). At a boundary between two different media some components

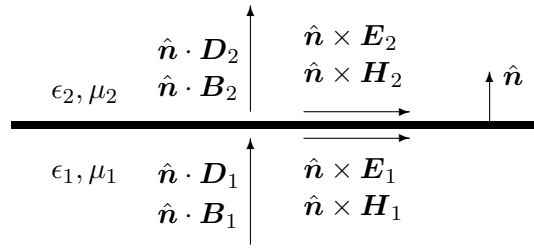


Figure 2.1: Boundary between two media.

of the fields are discontinuous [42, p. 12]. In this thesis only stationary boundaries will be considered.

$$\hat{n} \cdot (\mathbf{D}_2 - \mathbf{D}_1) = \rho_S \quad (2.17a)$$

$$\hat{n} \cdot (\mathbf{B}_2 - \mathbf{B}_1) = 0 \quad (2.17b)$$

$$\hat{n} \times (\mathbf{E}_2 - \mathbf{E}_1) = 0 \quad (2.17c)$$

$$\hat{n} \times (\mathbf{H}_2 - \mathbf{H}_1) = \mathbf{J}_S \quad (2.17d)$$

Many problems treat a boundary where one of the materials is a good conductor (e.g. a metal) which can be approximated by a PEC (Perfect Electric Conductor) which implies that all fields vanish inside the PEC. When this is the case the boundary conditions take the form

$$\hat{n} \cdot \mathbf{B} = 0, \quad (2.18a)$$

$$\hat{n} \times \mathbf{E} = 0. \quad (2.18b)$$

Analogous to the PEC there exists a PMC (Perfect Magnetic Conductor) which does not exist in practice. The reason to introduce this boundary condition in the thesis is that it will be used in COMSOL when modeling a parallel plate waveguide when utilizing symmetry in the setup. The tangential part of the magnetic field is then forced to be zero,

$$\hat{n} \cdot \mathbf{D} = 0, \quad (2.19a)$$

$$\hat{n} \times \mathbf{H} = 0. \quad (2.19b)$$

2.1.4 The Fourier transform of Maxwell's equations

When going to the frequency domain with the time harmonic expression of the solution presented in equation (2.3), Maxwell's equations takes a slightly different and simpler form. Every time derivative gets replaced by a multiplication of the factor $j\omega$:

$$\nabla \times \mathbf{E}(\mathbf{r}, \omega) = -j\omega \mathbf{B}(\mathbf{r}, \omega) \quad (2.20a)$$

$$\nabla \times \mathbf{H}(\mathbf{r}, \omega) = j\omega \mathbf{D}(\mathbf{r}, \omega) + \mathbf{J}(\mathbf{r}, \omega) \quad (2.20b)$$

$$\nabla \cdot \mathbf{D}(\mathbf{r}, \omega) = \rho(\omega) \quad (2.20c)$$

$$\nabla \cdot \mathbf{B}(\mathbf{r}, \omega) = 0. \quad (2.20d)$$

2.1.5 Wave impedance

The wave impedance Z of electromagnetic waves is defined as the ratio of the transverse parts of the electric and magnetic fields [42, 43]. The free-space wave impedance is $\eta_0 = \sqrt{\mu_0/\epsilon_0}$.

2.2 Guided waves

The discussion in this section is well covered in [42–44]. Waveguides are used to guide waves along a direction that we control and are used with high frequencies and they exhibit low losses. Different geometries of the cross section will affect which waves (called modes) that can propagate and their cut-off frequencies (the lowest frequency required). The waveguides presented here are hollow, i.e. they have metallic walls enclosing the region where the wave propagates. The direction of propagation is taken to be $+\hat{z}$. It will also be assumed that the waveguides are source free.

If assuming that the material inside the waveguide is isotropic and that the geometry along the propagating axis is non-varying, it is possible to divide the fields in a transverse part (\hat{x} and \hat{y}) and a longitudinal part (\hat{z}) which also is the propagating direction. Then it is shown in chapter 6 in [43] that it is only needed to solve the problem along the longitudinal direction, since the rest of the field components can be derived from it. The problems that need to be solved are the Helmholtz equations (here $\nabla_t^2 = \partial^2/\partial x^2 + \partial^2/\partial y^2$):

$$\nabla_t^2 E_z + k_c^2 E_z = 0 \quad (2.21a)$$

$$\nabla_t^2 H_z + k_c^2 H_z = 0, \quad (2.21b)$$

where $k_c = \omega\sqrt{\mu\epsilon}$ is the *propagation constant* (or *wave number*, *phase constant*) and if the wave propagates in a media which is not lossless, then k_c is a complex number since both ϵ and μ may take complex values.

By solving eqs. (2.21) inside the source-free volume bounded by a surface with proper boundary conditions we can determine which modes that can propagate in the given geometry. Inside an infinitely long hollow waveguide with PEC-walls the boundary conditions are

$$\begin{cases} E_z = 0 \\ \frac{\partial H_z}{\partial z} = 0. \end{cases}$$

Two types of waveguides will be presented, first the parallel plate and then the coaxial cable. The reason for choosing these two is that the two real setups that are being modeled in COMSOL are of these types. The particular parallel plate setup is described in detail in [21]. The coaxial cable is used because of the ability it brings to use relatively low frequencies.

The parallel plate and the coaxial cable have in common the ability to contain TEM (Transverse Electric Magnetic field) modes since they both consist of two separate conductors. As will be explained in coming sections, TEM modes have a DC cut-off frequency, i.e. $f_c = 0$. There exist two more modes of waves that need to be investigated; TE (Transverse Electric) and TM (Transverse Magnetic). Ideally in our setup only one propagating mode is desired.

2.2.1 TE and TM modes

Both the parallel plate and the coaxial cable can sustain the TE and TM modes and they can become a problem in a real setup. To determine the TE and TM modes it boils down to solving the eigenvalue problem (2.21) where the eigenvalues are denoted by k_c (in [43] called k_t). The corresponding eigenfunctions are the different modes that can propagate inside the waveguide. The eigenvalue problem takes different form depending on which mode you are solving for, see table 2.1.

The eigenvalues are the *cut-off wave number* (or *transverse wave number*) and the *cut-off frequency* is:

$$f_c = \frac{c_0 k_c}{2\pi \sqrt{\mu_r \epsilon_r}}. \quad (2.22)$$

In the propagation direction, \hat{z} , we have the so called *propagation constant* β (or the longitudinal wave number k_z) which is related to the cut-off wave number through [43, p.86]:

$$k^2 = k_c^2 + \beta^2. \quad (2.23)$$

TE	TM
$E_z = 0$	$E_z \neq 0$
$H_z \neq 0$	$H_z = 0$
$Z_{\text{TE}} = \frac{k\eta}{\beta}$	$Z_{\text{TM}} = \frac{\beta}{k\eta}$

Table 2.1: The TE and TM mode differences.

2.2.2 TEM modes

The TEM mode has both \hat{z} components equal to 0, i.e.

$$E_z(\mathbf{r}, \omega) = H_z(\mathbf{r}, \omega) = 0. \quad (2.24)$$

When solving the TEM problem it can be shown that you end up with the electrostatic problem, i.e. solving Laplace's equation in the transverse field components [42, p. 98]:

$$\nabla_t^2 \mathbf{E}_t = 0 \quad (2.25a)$$

$$\nabla_t^2 \mathbf{H}_t = 0. \quad (2.25b)$$

The TEM wave is the same as a static field between the two conductors. This can be used to argue that TEM waves can only exist when two or more conductors are present.

The wave impedance for a TEM-mode wave is the same as a plane wave propagating in the current material but without any boundaries. A TEM wave does not have any cut-off frequency since the propagation constant β is equal to the wave number k in the material. Furthermore, the wave impedance is:

$$Z_{\text{TEM}} = \sqrt{\frac{\mu}{\epsilon}} = \eta. \quad (2.26)$$

2.2.3 Parallel plates

The simplest waveguide is the parallel plate waveguide (see Figure 2.2). Even though it is an approximation it is an important waveguide to understand. The plates are big enough ($W \gg d$) so that fringing fields can be neglected and the field is non-varying in \hat{x}

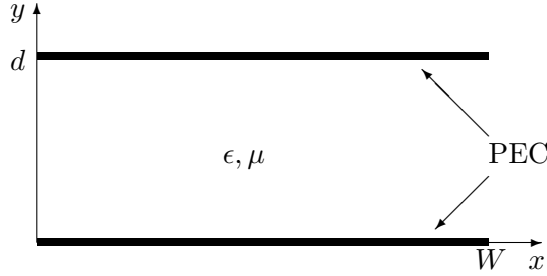


Figure 2.2: Parallel plate waveguide.

The parallel plate waveguide can sustain all three kinds of waves. The one we are interested in is the TEM mode. The higher order modes (TE and TM) can be suppressed by choosing the distance d between the plates. The cut-off wavenumbers and cut-off frequencies for both the TE_n and the TM_n modes are

$$k_c = n\pi/d \quad \Leftrightarrow \quad f_c = \frac{n}{2d\sqrt{\epsilon\mu}}. \quad (2.27)$$

In our setup $W = 1$ m and $d = 2$ cm. This leads to the first higher order modes (TE_1 and TM_1) will start to propagate at 7.5 GHz. In this thesis no real measurements have been done on this setup, only simulations using COMSOL. When simulating only a 2D model has been used, thus the problem of higher modes is not present. A more elaborate discussion about the waveguide at hand can be found in [21].

2.2.4 Coaxial cable

A coaxial cable is also a waveguide with two conductors. It can be studied with transmission line theory i.e. working with currents and voltages, or one can use the full Maxwell's equations with boundary conditions. Since it has two conductors it can also have TEM waves propagating.

The characteristic impedance of the coaxial cable (not to be confused with the wave impedance) is [42, p. 56]

$$Z_0 = \sqrt{\frac{\mu}{\epsilon}} \frac{\ln(b/a)}{2\pi}, \quad (2.28)$$

where a and b are the inner and outer radius of the conductors (cf. Figure 2.3).

The coaxial cable can of course also have TE- and TM-mode waves propagating. The first higher order mode in a coaxial is the TE_{11} mode which has the cut-off wavenumber k_c that satisfies [42, p. 132]

$$J'_n(k_c a) Y'_n(k_c b) = J'_n(k_c b) Y'_n(k_c a), \quad (2.29)$$

where J is the Bessel function of first kind and Y is the Bessel function of second kind. Find the solution for k_c numerically then insert it in eq. (2.22).

In this thesis two different coaxial fixtures has been simulated. The first fixture is a straight standard cable with the dimensions $a = 3.05$ mm and $b = 6.97$ mm (cf. Figure 2.3). The cable is air filled i.e. $\epsilon_r = \mu_r \approx 1$.

The second is a so-called tapered coaxial fixture. This means that it has a and b that varies, see Figure 2.4. The simulated tapered coaxial fixture had the following dimensions:

- $a_1 = 3.05$ mm
- $b_1 = 6.97$ mm
- $a_2 = 2a_1 = 6.10$ mm
- $b_2 = 2b_1 = 13.94$ mm.

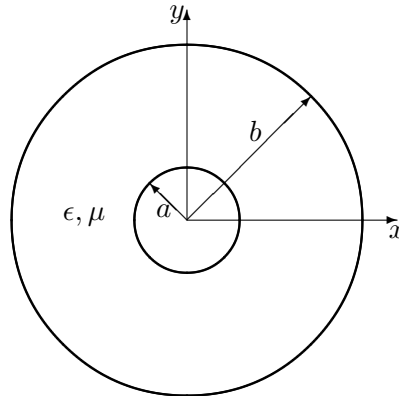


Figure 2.3: Cross section of a coaxial cable.

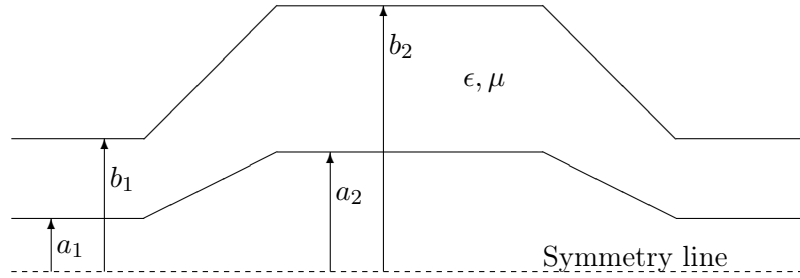


Figure 2.4: A longitudinal cross section of a tapered coaxial cable.

2.3 2-port networks

The theory discussed in this section is thoroughly explained in [6, 7, 40, 42, 43] to name a few. The theory here is limited to 2 ports, but is easily generalized to N -port networks.

Classical circuit theory is no longer sufficient when working with waves in the microwave regime (cm-waves to mm-waves), since the wavelength is not long compared to the physical size of the equipment. One way to take this into consideration is to use transmission line theory. Sometimes this can get very cumbersome if e.g. there are a lot of different components in the circuit. Then you can treat everything as black box with ports.

A 2-port network is an electric circuit or a model of a setup as an electric circuit. It consists of four terminals, or rather two ports (see Figure 2.5). In the following subsections two types of matrix representations ($[\mathbf{S}]$ and $[\mathbf{T}]$) will be introduced which relates one of the ports to the other. Only linear and passive networks will be considered e.g. it may contain resistors, capacitors and inductors but not amplifiers and generators.

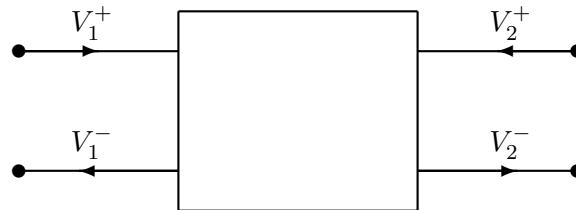


Figure 2.5: A two-port network with incoming and outgoing waves. The networks are assumed to be linear and passive.

2.3.1 The scattering matrix, $[\mathbf{S}]$

When working with microwaves (cm- to mm-waves) it is difficult to define voltages and currents for non-TEM waves. Then it is more convenient to work with waves, i.e. incident, reflected and transmitted waves. This is exactly how the scattering matrix is defined. The $[\mathbf{S}]$ matrix is easily measured with a Vector Network Analyzer (VNA), and once obtained it contains a complete description of the network. With the notation in Figure 2.5 we get:

$$\begin{pmatrix} V_1^- \\ V_2^- \end{pmatrix} = \begin{pmatrix} S_{11} & S_{12} \\ S_{21} & S_{22} \end{pmatrix} \begin{pmatrix} V_1^+ \\ V_2^+ \end{pmatrix}, \quad (2.30)$$

where the scattering matrix is defined as:

$$[\mathbf{S}] = \begin{pmatrix} S_{11} & S_{12} \\ S_{21} & S_{22} \end{pmatrix}. \quad (2.31)$$

So the scattering matrix relates the reflected and transmitted waves to the incident waves at each port, e.g. S_{11} is the reflection from port 1 when there is an incident wave at port 1 and a matched load at port 2.

If the network under consideration is reciprocal then $S_{12} = S_{21}$ and if the network is symmetric then $S_{11} = S_{22}$. The reciprocity makes the $[\mathbf{S}]$ matrix symmetric, i.e.

$$[\mathbf{S}] = [\mathbf{S}]^t, \quad (2.32)$$

where t denotes the transpose [42, 43].

2.3.2 The transmission matrix, $[\mathbf{T}]$

Often you work with a cascade of networks. Then it is more convenient to use the transmission matrix (sometimes called the scattering transfer matrix). This representation relates the incident and reflected waves at each port, whereas the scattering matrix relates the incident waves to the reflected waves. The definition takes the form

$$\begin{pmatrix} V_1^+ \\ V_1^- \end{pmatrix} = \begin{pmatrix} T_{11} & T_{12} \\ T_{21} & T_{22} \end{pmatrix} \begin{pmatrix} V_2^- \\ V_2^+ \end{pmatrix}, \quad (2.33)$$

where the Transmission matrix is defined as

$$[\mathbf{T}] = \begin{pmatrix} T_{11} & T_{12} \\ T_{21} & T_{22} \end{pmatrix}. \quad (2.34)$$

The symmetry and reciprocal conditions for scattering matrices using the relations above takes the form:

$$\begin{aligned} T_{12} &= -T_{21} && \text{Symmetric,} \\ \det([\mathbf{T}]) &= T_{11}T_{22} - T_{12}T_{21} = 1 && \text{Reciprocal.} \end{aligned}$$

In eq. (2.33), when defining the transmission matrix, care has to be taken that the definition might differ in different books and programs. It has to do with the defined directions of the waves in Figure 2.5.

2.3.3 Relation between $[\mathbf{S}]$ and $[\mathbf{T}]$

The $[\mathbf{S}]$ and $[\mathbf{T}]$ matrices are closely related and it can be shown by solving (2.30) and (2.33) that

$$\begin{aligned} T_{11} &= \frac{-\det([\mathbf{S}])}{S_{21}} && T_{12} = \frac{S_{11}}{S_{21}}, \\ T_{21} &= \frac{-S_{22}}{S_{21}} && T_{22} = \frac{1}{S_{21}}. \end{aligned}$$

There are similar relations that transform the T -parameters to S -parameters

$$\begin{aligned} S_{11} &= \frac{T_{12}}{T_{22}} & S_{12} &= \frac{\det([\mathbf{T}])}{T_{22}}, \\ S_{21} &= \frac{1}{T_{22}} & S_{22} &= \frac{-T_{21}}{T_{22}}. \end{aligned}$$

2.3.4 Moving the reference planes

Sometimes you might have an additional transmission line cable or waveguide that transports the wave to and from the ports. Then the wave accumulates phase which needs to be taken care of. This section shows how the scattering parameters transform when shifting the reference planes to a new location.

If the original locations are set to be $z_1 = z_2 = 0$ then the new locations of reference planes at port 1 and 2 are $z_1 = l_1$ and $z_2 = l_2$ (see Figure 2.6) where l_1 and l_2 are the physical lengths. Then the waves have accumulated the phases $\theta_1 = \beta l_1$ and $\theta_2 = \beta l_2$, where β is the phase constant introduced in section 2.2.



Figure 2.6: A two-port network with incoming and outgoing waves. The reference planes are moved from the ports.

If the scattering matrix at the new positions is denoted be $[\mathbf{S}']$ then it relates to $[\mathbf{S}]$ through [42]

$$[\mathbf{S}'] = \begin{pmatrix} e^{-j\theta_1} & 0 \\ 0 & e^{-j\theta_2} \end{pmatrix} [\mathbf{S}] \begin{pmatrix} e^{-j\theta_1} & 0 \\ 0 & e^{-j\theta_2} \end{pmatrix}. \quad (2.38)$$

$$[\mathbf{S}'] = \begin{pmatrix} S_{11}e^{-2j\theta_1} & S_{12}e^{-j(\theta_1+\theta_2)} \\ S_{21}e^{-j(\theta_1+\theta_2)} & S_{22}e^{-2j\theta_2} \end{pmatrix}. \quad (2.39)$$

Similar relations hold for a N -port network.

3

Errors and calibration

3.1 Network Analyzers

A network analyzer is an instrument which is used when measuring the $[\mathbf{S}]$ matrix because of the ease of measuring reflection and transmission at high frequencies. There exist two types of network analyzers, Scalar Network Analyzer (SNA) and Vector Network Analyzer (VNA).

The SNA only measures the amplitudes of the waves whereas the VNA also measures the phases. To cover in detail the inner workings of a network analyzer is outside the scope of this thesis but in [42, p. 188] a good (simplified) block diagram and description of a VNA is presented. The basic idea is that it has a RF source which creates the electromagnetic wave to be sent through the DUT and then measures the scattered waves. Each physical port of the VNA is a part of a 4-port network which contains the directional couplers or bridges to separate the incident and reflected waves.

3.2 Error sources and error coefficients

A VNA is already calibrated once after fabrication and it is easy to confuse this calibration with the one that is being performed in this thesis. This means that at the ports of the VNA the amplitude and phase of the signal is well known, but when e.g. a coaxial cable is connected to the VNA the created electromagnetic wave has a further distance to propagate. This extra length changes the phase and thus the measurements lose accuracy since the original calibration has its reference planes at the VNA ports. Thus, another calibration (or *error correction*) is needed to move the reference planes to the end of the coaxial cables where a device or material will be measured. But if these cables in turn are connected to some other device (e.g. waveguides) through which the wave propagates before reaching the DUT the planes must be moved further to compensate this change in phase.

It is not only the phase of the measured signal that may be affected. Through cable connections and transition from cable to waveguide impedance mismatch may occur, hence some a part of the wave will be reflected. These kinds of mismatch errors must also be corrected for.

3.2.1 Sources of error

Sources of error are divided into three groups [23]:

1. Random errors,
2. Drift errors,
3. Systematic errors.

Random errors, as described by the name, vary over time in a non-predictable manner. The random nature of the errors makes them impossible to eliminate through calibration. The main source of random errors comes from instrument noise.

Drift errors are when the system's performance changes over time after a calibration has been performed. The primary source of drifting comes from temperature fluctuations. To avoid this the setup should be placed in a room or environment that is temperature controlled or has stable ambient temperature.

Systematic errors are caused by imperfections in the setup and are related to signal leakage, signal reflections and frequency response. There are six types of systematic error which are described as [23, p. 3]:

- Directivity and crosstalk errors relating to signal leakage,
- Source and load impedance mismatches relating to reflections,
- Frequency response errors caused by reflection and transmission tracking within the test receivers.

3.2.2 Error coefficients

12-term model

If the errors do not vary over time they can be removed through calibration. In a two-port setup these six errors of course occur in both directions (forward and backwards i.e. from port 1-2 and 2-1). Thus, to do a full two-port calibration there are 12 terms to be determined.

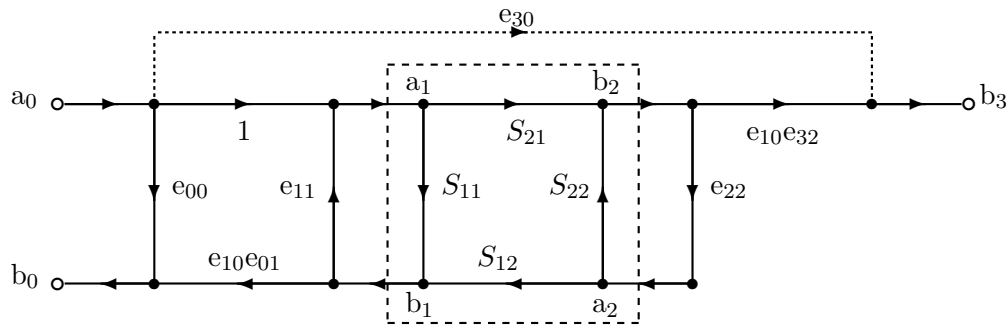


Figure 3.1: Forward diagram of the 12-term error model. The part in the middle represents the DUT, i.e. the desired scattering parameters. The six different error coefficients that are going to be characterized through calibration. An identical model for the other direction (backwards) is also defined but with different error coefficients. [45]

In Figure 3.1 the six different errors are represented. They are:

$$\begin{aligned}
 e_{00} &= \text{Directivity}, & e_{11} &= \text{Port-1 match}, \\
 e_{10}e_{01} &= \text{Reflection tracking}, & e_{10}e_{32} &= \text{Transmission tracking}, \\
 e_{22} &= \text{Port-2 match}, & e_{30} &= \text{Crosstalk leakage}.
 \end{aligned}$$

8-term model

If the crosstalk leakage is assumed to be zero, or can be calibrated in a separate step, and the switch (the mechanism that selects which port is the transmitting and which is the receiving) is assumed to be perfect (i.e. it will not change the port match of the network when it is switched from forward to reversed), then one can derive the 8-term model from the 12-term model (see Figure 3.2) [45]. The assumption that the switch is perfect is only valid if the four measurement channels are on the DUT side of the switch.

Using transfer parameters (the $[\mathbf{T}]$ -matrix) and cascading the matrices in Figure 3.2 one gets

$$[\mathbf{T}_M] = [\mathbf{T}_X] [\mathbf{T}] [\mathbf{T}_Y], \quad (3.2)$$

where \mathbf{X} and \mathbf{Y} are the error networks on the left and right side of the DUT. $[\mathbf{T}_M]$ is the measured transfer scattering parameters and $[\mathbf{T}]$ is the transfer scattering parameters of the DUT. From section 2.3.2 and eq. (2.36) the different matrices are (where Δ denotes the *determinant* operation in linear algebra):

$$\begin{aligned}
 [\mathbf{T}_M] &= \frac{1}{S_{21M}} \begin{pmatrix} -\Delta_M & S_{11M} \\ -S_{22M} & 1 \end{pmatrix} & [\mathbf{T}] &= \frac{1}{S_{21}} \begin{pmatrix} -\Delta_S & S_{11} \\ -S_{22} & 1 \end{pmatrix} \\
 [\mathbf{T}_X] &= \frac{1}{e_{10}} \begin{pmatrix} -\Delta_X & e_{00} \\ -e_{11} & 1 \end{pmatrix} & [\mathbf{T}_Y] &= \frac{1}{e_{32}} \begin{pmatrix} -\Delta_Y & e_{22} \\ -e_{33} & 1 \end{pmatrix}
 \end{aligned}$$

With a slightly different mathematical formulation where we consider the error adapter as just one located between the perfect measurement system (VNA) and the DUT it looks like [45]:

$$\begin{bmatrix} b_0 \\ b_3 \\ a_0 \\ a_3 \end{bmatrix} = \left[\begin{array}{c|c} \mathbf{T}_1 & \mathbf{T}_2 \\ \hline \mathbf{T}_3 & \mathbf{T}_4 \end{array} \right] \begin{bmatrix} b_1 \\ b_2 \\ a_1 \\ a_2 \end{bmatrix} \quad (3.4)$$

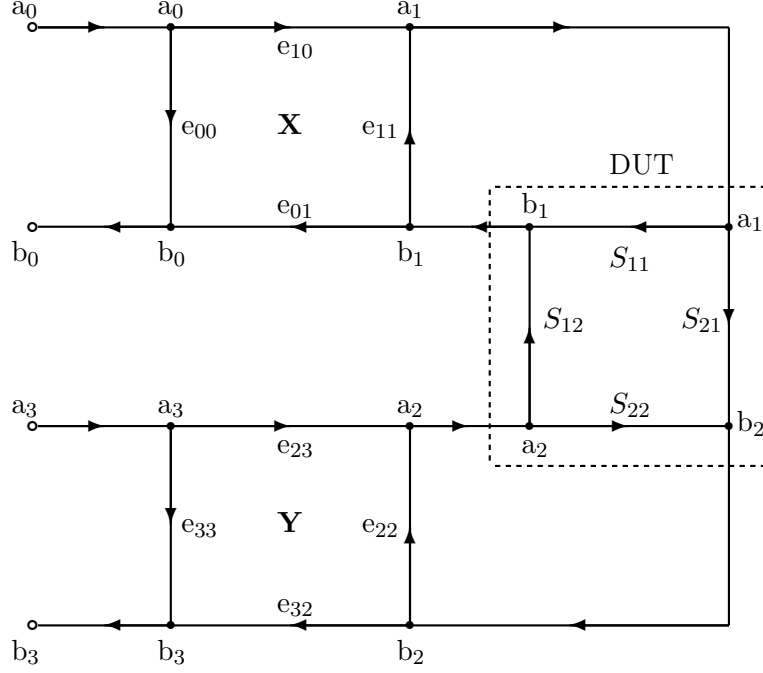


Figure 3.2: Flow graph for the 8-term error model. The number of error terms is reduced to 7 since they can be normalized.

with

$$\begin{aligned} \mathbf{T}_1 &= \begin{pmatrix} -\Delta_X & 0 \\ 0 & -k\Delta_Y \end{pmatrix} & \mathbf{T}_2 &= \begin{pmatrix} e_{00} & 0 \\ 0 & ke_{33} \end{pmatrix} \\ \mathbf{T}_3 &= \begin{pmatrix} -e_{11} & 0 \\ 0 & -ke_{22} \end{pmatrix} & \mathbf{T}_4 &= \begin{pmatrix} 1 & 0 \\ 0 & k \end{pmatrix} \\ k &= \frac{e_{10}}{e_{23}} \end{aligned}$$

The 7 error terms are now Δ_X , $k\Delta_Y$, e_{00} , ke_{33} , e_{11} , ke_{22} and k . Once these 7 terms have been determined through calibration with different known standards measurements can be done on a DUT where the actual $[\mathbf{T}]$ matrix can be de-embedded from eq. (3.2) and then transformed back to scattering parameters.

There are several methods for doing this kind of calibration, many of them using well known standards. Well known methods are SOLT (Short-Open-Load-Through), TRL (Through-Reflect-Line) and TLN (Through-Line-Network) [23, 24].

The term *self-calibration* means that the object on which you are measuring is used during the calibration as an unknown standard. This reduces the need for well known (and expensive) standards. All the algorithms treated in this report are of self-calibration kind. In all three algorithms a material slab is being used to calibrate the set-up, but after the calibration we have not only determined the error coefficients but also extracted the scattering matrix for the slab.

3.3 Random noise

Since in this thesis the means of obtaining scattering parameters is to use simulations there will be no presence of white noise. White noise is a random signal that originates from e.g. signal sources and other electrical components. To add this source of error to the simulated data a function for adding small random numbers was written. To get a good approximation of the amplitude a through measurement on a VNA was performed. Then it is known that the S_{21} parameter should be constant 1. The mean deviation around 1 is taken as the amplitude of the white noise, see Figure 3.3.

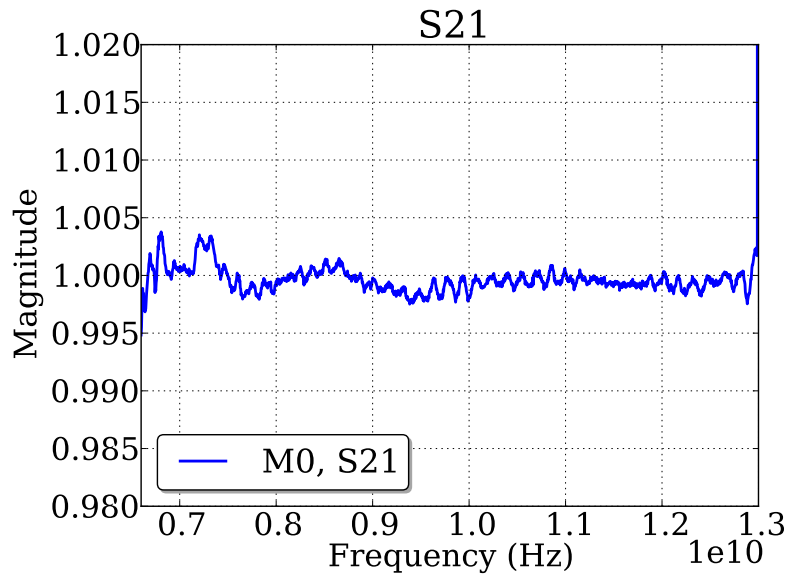


Figure 3.3: A through measurement on a calibrated VNA.

Extraction of the material parameters, ϵ_r and μ_r

4.1 The Nicolson-Ross-Weir Algorithm

The Nicolson-Ross-Weir algorithm [8,9] is a method to extract material parameters from a scattering measurement of a planar, linear, homogeneous and isotropic material slab. From section 2.1.2 we know that isotropic and linear materials has a constitutive relation described by a scalar, ϵ_r . The same holds for magnetic materials. The equations behind the algorithm will be presented and then the intrinsic problems with the algorithm will be discussed. The quantities to be determined are

$$\epsilon = (\epsilon'_r - j\epsilon''_r)\epsilon_0, \quad \mu = (\mu'_r - j\mu''_r)\mu_0. \quad (4.1)$$

The reflection coefficient for a slab can be written as

$$\Gamma = \chi \pm \sqrt{\chi^2 - 1}, \quad (4.2)$$

where

$$\chi = \frac{S_{11}^2 - S_{21}^2 + 1}{2S_{11}}. \quad (4.3)$$

In eq. (4.2) the sign is chosen so that $|\Gamma| \leq 1$. The propagation factor for a wave traveling through a slab with thickness d is defined as

$$P = e^{-\gamma d} = e^{-(\alpha + j\beta)d}, \quad (4.4)$$

with

γ propagation constant

$\alpha = \text{Re}(\gamma)$ attenuation constant

$\beta = \text{Im}(\gamma)$ phase constant.

γ can also be expressed as

$$\gamma = j\frac{2\pi}{\lambda_0} \sqrt{\epsilon_r \mu_r - \frac{\lambda_0}{\lambda_c}}, \quad (4.5)$$

where λ_0 is the free space wavelength and λ_c is the cut-off wavelength of the transmission line. The propagation factor, P , can be expressed in terms of S_{11} , S_{21} and Γ :

$$P = \frac{S_{11} + S_{21} - \Gamma}{1 - (S_{11} + S_{21})\Gamma}. \quad (4.6)$$

According to [9] the complex permittivity, ϵ_r , and the complex permeability, μ_r , can be extracted from P and Γ :

$$\epsilon_r \mu_r = n^2 = - \left[\frac{\lambda_0^2}{2\pi d} \ln \left(\frac{1}{P} \right) \right]^2 + \frac{\lambda_0^2}{\lambda_c^2}, \quad (4.7a)$$

$$\mu_r = \frac{1 + \Gamma}{1 - \Gamma} \sqrt{\frac{n^2 - \lambda_0^2/\lambda_c^2}{1 - \lambda_0^2/\lambda_c^2}}, \quad (4.7b)$$

with n as the refractive index. Here we recognize the normalized impedance, z

$$z = \frac{1 + \Gamma}{1 - \Gamma} \quad (4.8)$$

which can be expressed in the scattering parameters [12]:

$$z = \pm \sqrt{\frac{(1 + S_{11})^2 - S_{21}^2}{(1 - S_{11})^2 - S_{21}^2}}. \quad (4.9)$$

The sign ambiguity can be solved due to the passivity condition which requires that $\text{Re}(z) \geq 0$ [15]. With the expression for the normalized impedance, (4.8), equation (4.4) can be rewritten to contain only the scattering parameters and thus makes the step of calculating Γ redundant.

$$P = \frac{1 - S_{11}^2 + S_{21}^2}{2S_{21}} + \frac{2S_{11}}{\left(z - \frac{1}{z}\right) S_{21}}. \quad (4.10)$$

Even though this method is relatively straightforward and simple it unfortunately suffers from two drawbacks [14]. The first lies in eq. (4.7a) since the logarithm of a complex number is not injective. Since it is 2π periodic, it does not have a unique inverse. This problem is rather easy to solve with some a-priori knowledge about the slab thickness so that the phase can be compensated for.

The second problem with NRW lies in eq. (4.9) when $S_{11} \approx 0$ and $S_{21} \approx 1$. This occurs when the wavelength of the signal corresponds to an integer multiplied by half a wavelength in the slab, and the slab has low losses. When this happens the expression gets numerically unstable (it is undefined). The instability can be avoided with different methods. The simplest is when dealing with slabs which are nonmagnetic ($\mu_r = 1$) then the product $\epsilon_r \mu_r$ in eq. (4.7a) equals ϵ_r . This expression is stable.

As stated in the beginning of this section the NRW method is constructed for planar, linear, homogeneous and isotropic samples. In the advances of metamaterials, which are not homogeneous, new methods have been presented. In [13] effective boundaries (edges

of the slab) are introduced which is where the scattered field can be thought of as planar waves again.

To some extent, it is possible to measure the constitutive parameters in an anisotropic material slab. Anisotropy, which was described in section 2.1.2, is when the material has different properties in different directions. Hence, the simple scalar relation in eq. (2.13) does not hold but the full matrix representation in eq. (2.11) must be utilized. In [10] a method for biaxial materials is presented. Biaxial means that all off-diagonal elements in eq. (2.11) are zero. Then the six parameters, ϵ_{xx} , ϵ_{yy} , ϵ_{zz} , μ_{xx} , μ_{yy} and μ_{zz} , can be determined. One limitation is that the biaxial materials principal axes must coincide with axes $(\hat{x}, \hat{y}, \hat{z})$ of the waveguide.

5

The algorithms

All algorithms presented require two things from the DUT/MUT (Device/Material Under Test); it has to be reciprocal ($S_{21} = S_{12}$) and symmetrical ($S_{11} = S_{22}$). For a material slab these requirements impose that the refractive index has to be symmetrically distributed. The slab edges do not necessarily have to be planar but should also be symmetric.

The LNN and Extended LNN uses one network (MUT or DUT) and makes four different measurement (cf. Figure 5.1); one Line measurement and three measurements where the DUT is placed at three different positions (Network). The difference between LNN and Extended LNN is not huge, but the Extended LNN should be more stable since the distances between different positions of the object slab are not so crucial. For the LNN method the distance between the positions must be equal.

The TTN method only requires two measurements; one Through and one measurement with the DUT (Network) placed in the middle. This greatly simplifies calibration in certain setups, e.g. in free-space measurements. The method looks really promising, but the setup must fulfill some initial conditions, e.g. it must have a fairly flat frequency response which means that the setup should not respond differently at different frequencies.

5.1 Calibration standards

It has been stated that the algorithms in this report are all of self-calibration type. This means that the obstacle being measured is one of the calibration standards. The VNA measures the scattering matrix, $[\mathbf{S}]$, but in this chapter we are working with the transfer scattering matrix, $[\mathbf{T}]$, since the networks are cascaded.

The self-calibration object is here denoted by $[\mathbf{Q}]$ and the aim of the algorithms is to calculate the four parameters (q_{ij} , $i, j = 1, 2$) of the matrix. In all methods the slab has been implemented as a zero length two-port network. When the parameters of $[\mathbf{Q}]$ have been determined, one has

$$[\mathbf{Q}] = \begin{pmatrix} q_{11} & q_{12} \\ q_{21} & q_{22} \end{pmatrix}, \quad \text{Network} \quad (5.1)$$

$$[\mathbf{L}] = \begin{pmatrix} k & 0 \\ 0 & k^{-1} \end{pmatrix}, \quad \text{Line} \quad (5.2)$$

where $k = e^{-\gamma l}$.

In the TTN calibration a third standard is used; the Through measurement. Its transfer matrix is

$$[\mathbf{T}] = \begin{pmatrix} 1 & 0 \\ 0 & 1 \end{pmatrix}, \quad \text{Through} \quad (5.3)$$

When all the q parameters have been determined they will be converted to scattering parameters and then the NRW will be used to extract the material data of interest, e.g. n , Z , ϵ_r and μ_r .

5.2 Line-Network-Network

Four measurements need to be done in the LNN calibration. The four schematic setups are shown in Figure 5.1. The $[\mathbf{G}]$ and $[\mathbf{H}]$ networks include all the errors; the propagation in the medium, the errors originating in the antennas and the imperfect connections or transitions.

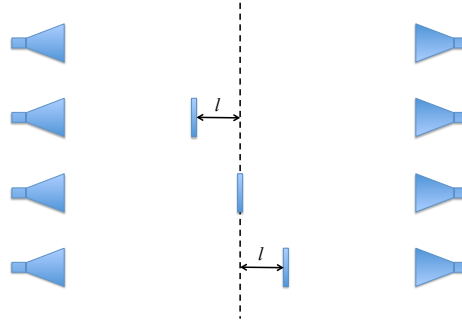


Figure 5.1: The four different LNN calibration standards.

$$[\mathbf{M}_L] = [\mathbf{G}] [\mathbf{L}] [\mathbf{L}] [\mathbf{H}]^{-1} \quad (5.4a)$$

$$[\mathbf{M}_{N1}] = [\mathbf{G}] [\mathbf{Q}] [\mathbf{L}] [\mathbf{L}] [\mathbf{H}]^{-1} \quad (5.4b)$$

$$[\mathbf{M}_{N2}] = [\mathbf{G}] [\mathbf{L}] [\mathbf{Q}] [\mathbf{L}] [\mathbf{H}]^{-1} \quad (5.4c)$$

$$[\mathbf{M}_{N3}] = [\mathbf{G}] [\mathbf{L}] [\mathbf{L}] [\mathbf{Q}] [\mathbf{H}]^{-1} \quad (5.4d)$$

$$\beta_1 = \text{trace} \left([\mathbf{M}_{\mathbf{N}1}] [\mathbf{M}_{\mathbf{L}}]^{-1} \right) = \text{trace} ([\mathbf{Q}]) \quad (5.5a)$$

$$\beta_2 = \text{trace} \left([\mathbf{M}_{\mathbf{N}1}] [\mathbf{M}_{\mathbf{N}2}]^{-1} \right) = \text{trace} \left([\mathbf{Q}] [\mathbf{L}] [\mathbf{Q}]^{-1} [\mathbf{L}]^{-1} \right) \quad (5.5b)$$

$$\beta_3 = \text{trace} \left([\mathbf{M}_{\mathbf{N}1}] [\mathbf{M}_{\mathbf{N}3}]^{-1} \right) = \text{trace} \left([\mathbf{Q}] [\mathbf{L}] [\mathbf{L}] [\mathbf{Q}]^{-1} [\mathbf{L}]^{-1} [\mathbf{L}]^{-1} \right) \quad (5.5c)$$

Evaluating the traces in eqs. (5.5) yields the following equations [28, 29]

$$\beta_1 = q_{11} + q_{22} \quad (5.6a)$$

$$\beta_2 = 2q_{11}q_{22} - q_{12}q_{21}(k^2 + k^{-2}) \quad (5.6b)$$

$$= 2 - q_{12}q_{21} [2 \cosh(2\gamma l) - 2] \quad (5.6c)$$

$$\beta_3 = 2q_{11}q_{22} - q_{12}q_{21}(k^4 + k^{-4}) \quad (5.6d)$$

$$= 2 - q_{12}q_{21} [2 \cosh(4\gamma l) - 2] \quad (5.6e)$$

Dividing eqs. (5.6e) and (5.6c) gives an expression for the complex phase constant γl , or if the mechanical length l is known the propagation constant γ .

$$\cosh(2\gamma l) = \frac{1}{2} \frac{2 - \beta_3}{2 - \beta_2} - 1 \quad (5.7)$$

One of the initial requirements was that the obstacle should be reflection-symmetrical which in transfer parameters gives

$$q_{12} = -q_{21} \quad (5.8)$$

which is inserted into eq. (5.6c) and gives the equation

$$q_{21} = \pm \sqrt{\frac{\beta_2 - 2}{2 \cosh(2\gamma l) - 2}}. \quad (5.9)$$

Since $[\mathbf{Q}]$ is the transfer scattering matrix of a two-port reciprocal network the following relation (from section 2.3.2) holds

$$q_{11}q_{22} - q_{12}q_{21} = 1. \quad (5.10)$$

Combining eq. (5.10) and the first in eqs. (5.6) results in

$$q_{11} = \frac{\beta_1}{2} \pm \sqrt{\frac{\beta_1^2}{4} + q_{21}^2 - 1} \quad (5.11)$$

and then q_{22} is easily calculated from eq. (5.6a).

$$q_{21} = \pm \sqrt{\frac{\beta_2 - 2}{2 \cosh(2\gamma l) - 2}} \quad (5.12a)$$

$$q_{12} = -q_{21} \quad (5.12b)$$

$$q_{11} = \frac{\beta_1}{2} \pm \sqrt{\frac{\beta_1^2}{4} + q_{21}^2 - 1} \quad (5.12c)$$

$$q_{22} = \beta_1 - q_{11} \quad (5.12d)$$

5.3 Extended Line-Network-Network

This calibration method only differs from the previous LNN in that the $[\mathbf{L}]$ network can differ. The measurement setups are shown in Figure 5.2. The equations will be different and more signs have to be chosen.

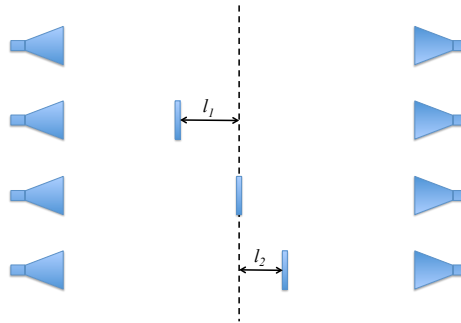


Figure 5.2: The four different Extended LNN calibration standards.

$$[\mathbf{M}_L] = [\mathbf{G}] [\mathbf{L}_1] [\mathbf{L}_2] [\mathbf{H}]^{-1} \quad (5.13a)$$

$$[\mathbf{M}_{N1}] = [\mathbf{G}] [\mathbf{L}_1] [\mathbf{L}_2] [\mathbf{Q}] [\mathbf{H}]^{-1} \quad (5.13b)$$

$$[\mathbf{M}_{N2}] = [\mathbf{G}] [\mathbf{L}_1] [\mathbf{Q}] [\mathbf{L}_2] [\mathbf{H}]^{-1} \quad (5.13c)$$

$$[\mathbf{M}_{N3}] = [\mathbf{G}] [\mathbf{Q}] [\mathbf{L}_1] [\mathbf{L}_2] [\mathbf{H}]^{-1} \quad (5.13d)$$

$$\beta_1 = \text{trace} \left([\mathbf{M}_{\mathbf{N1}}] [\mathbf{M}_{\mathbf{L}}]^{-1} \right) = \text{trace} ([\mathbf{Q}]) \quad (5.14a)$$

$$\beta_2 = \text{trace} \left([\mathbf{M}_{\mathbf{N3}}] [\mathbf{M}_{\mathbf{N2}}]^{-1} \right) = \text{trace} \left([\mathbf{Q}] [\mathbf{L}_1] [\mathbf{Q}]^{-1} [\mathbf{L}_1]^{-1} \right) \quad (5.14b)$$

$$\beta_3 = \text{trace} \left([\mathbf{M}_{\mathbf{N2}}] [\mathbf{M}_{\mathbf{N1}}]^{-1} \right) = \text{trace} \left([\mathbf{Q}] [\mathbf{L}_2] [\mathbf{Q}]^{-1} [\mathbf{L}_2]^{-1} \right) \quad (5.14c)$$

$$\beta_4 = \text{trace} \left([\mathbf{M}_{\mathbf{N3}}] [\mathbf{M}_{\mathbf{N1}}]^{-1} \right) = \text{trace} \left([\mathbf{Q}] [\mathbf{L}_1] [\mathbf{L}_2] [\mathbf{Q}]^{-1} [\mathbf{L}_2]^{-1} [\mathbf{L}_1]^{-1} \right) \quad (5.14d)$$

$$\beta_1 = q_{11} + q_{22}, \quad (5.15a)$$

$$\beta_2 = 2q_{11}q_{22} - q_{12}q_{21} (k_1 + k_1^{-1})^2, \quad (5.15b)$$

$$\beta_3 = 2q_{11}q_{22} - q_{12}q_{21} (k_2 + k_2^{-1})^2, \quad (5.15c)$$

$$\beta_4 = 2q_{11}q_{22} - q_{12}q_{21} (k_1k_2 + k_1^{-1}k_2^{-1})^2. \quad (5.15d)$$

Reciprocity makes it possible to simplify it further

$$\beta_1 = q_{11} + q_{22}, \quad (5.16a)$$

$$\beta_2 = 2 - q_{12}q_{21} (k_1 - k_1^{-1})^2, \quad (5.16b)$$

$$\beta_3 = 2 - q_{12}q_{21} (k_2 - k_2^{-1})^2, \quad (5.16c)$$

$$\beta_4 = 2 - q_{12}q_{21} (k_1k_2 - k_1^{-1}k_2^{-1})^2. \quad (5.16d)$$

Define α_1 and α_2 as

$$\alpha_1^2 = \frac{\beta_2 - 2}{\beta_3 - 2} = \frac{(k_1 - k_1^{-1})^2}{(k_2 - k_2^{-1})^2}, \quad (5.17a)$$

$$\alpha_2^2 = \frac{\beta_2 - 2}{\beta_4 - 2} = \frac{(k_1 - k_1^{-1})^2}{(k_1k_2 - k_1^{-1}k_2^{-1})^2}. \quad (5.17b)$$

Using these equations one can solve for k_1 and k_2 , resulting in

$$k_2^2 + k_2 \left(\frac{\alpha_2}{\alpha_1^2} - \alpha_2 - \frac{1}{\alpha_2} \right) + 1 = 0, \quad (5.18a)$$

$$k_1 = \frac{-\alpha_2}{\alpha_1 (\alpha_2 k_2 - 1)}. \quad (5.18b)$$

Now the q_{ij} -parameters can be calculated:

$$q_{12} = \pm \sqrt{\frac{\beta_2 - 2}{(k_1 - k_1^{-1})^2}} \quad (5.19a)$$

$$q_{21} = -q_{12} \quad (5.19b)$$

$$q_{11} = \frac{\beta_1}{2} \pm \sqrt{\frac{\beta_1^2}{4} + q_{12}^2 - 1} \quad (5.19c)$$

$$q_{22} = \beta_1 - q_{11} \quad (5.19d)$$

One of the articles ([31]) containing this method unfortunately had an error in one of the equations (eq. (17)). In the numerator under the square root it should read $\beta_2 - 2$ and not $2 - \beta_2$. This appears to be a simple misprint, because in another article ([30]) the equation is correct.

5.4 Through-Through-Network

The measurements that need to be done is shown in Figure 5.3. The TTN is very similar to the TLN (Through-Line-Network) calibration method. The TTN method imitates the [L] standard by making two Through measurements at different frequencies. This puts an important requirement on the setup. The system needs to have a flat frequency response, i.e. the behaviour of the system (including antennas) should not vary too much when varying the frequency. What the frequency shift does is to make the phase differ, which would be the case if an extra line was inserted in the system.

The frequency shift should be chosen so that the electrical length changes by approximately 90° ($\pi/4$ rad) [32]. This requirement implies that the setup needs to be sufficiently long so that the shift in frequency is not larger than necessary.

There are two ways to obtain the [L] network. The first is to make two through measurements and the second is (if the frequency sampling is high enough) to make one measurement and let the algorithm shift the frequency.

The actual frequency that we are measuring at will here be called f_i and the neighbouring frequency is $f_i + \Delta f$ where Δf is chosen according to above mentioned requirements.

To be consistent with the articles (but not with the rest of this report), the following notations for the transfer scattering matrices are used:

$$[\mathbf{T}] = \Sigma \mathbf{C}_{\mathbf{T}}(f_i) = \begin{pmatrix} 1 & 0 \\ 0 & 1 \end{pmatrix}, \quad \text{Through} \quad (5.20)$$

$$[\mathbf{L}] = \Sigma \mathbf{C}_{\mathbf{L}}(f_i) = \Sigma \mathbf{C}_{\mathbf{T}}(f_i + \Delta f) = \begin{pmatrix} k(f_i + \Delta f) & 0 \\ 0 & (k(f_i + \Delta f))^{-1} \end{pmatrix}, \quad \text{Through} \quad (5.21)$$

$$[\mathbf{Q}] = \Sigma \mathbf{C}_{\mathbf{N}}(f_i) = \begin{pmatrix} q_{11} & q_{12} \\ q_{21} & q_{22} \end{pmatrix}, \quad \text{Network.} \quad (5.22)$$

The error networks are still $[\mathbf{G}]$ and $[\mathbf{H}]$. With these definitions the cascade of matrices for the different measurements looks like (cf. Figure 5.3):

$$[\mathbf{M}_1] = [\mathbf{G}] \Sigma \mathbf{C}_{\mathbf{T}}(f_i) [\mathbf{H}]^{-1} \quad (5.23a)$$

$$[\mathbf{M}_2] = [\mathbf{G}] \Sigma \mathbf{C}_{\mathbf{T}}(f_i + \Delta f) [\mathbf{H}]^{-1} \quad (5.23b)$$

$$[\mathbf{M}_3] = [\mathbf{G}] \Sigma \mathbf{C}_{\mathbf{N}}(f_i) [\mathbf{H}]^{-1} \quad (5.23c)$$

Then these are combined to form

$$\beta_{21} = \text{trace}([\mathbf{M}_2][\mathbf{M}_1]^{-1}) = \text{trace}(\Sigma \mathbf{C}_{\mathbf{L}} \Sigma \mathbf{C}_{\mathbf{T}}^{-1}) \quad (5.24a)$$

$$\beta_{31} = \text{trace}([\mathbf{M}_3][\mathbf{M}_1]^{-1}) = \text{trace}(\Sigma \mathbf{C}_{\mathbf{N}} \Sigma \mathbf{C}_{\mathbf{T}}^{-1}) \quad (5.24b)$$

$$\beta_{32} = \text{trace}([\mathbf{M}_3][\mathbf{M}_2]^{-1}) = \text{trace}(\Sigma \mathbf{C}_{\mathbf{N}} \Sigma \mathbf{C}_{\mathbf{L}}^{-1}) \quad (5.24c)$$

$$\beta_{21} = k + k^{-1} \quad (5.25a)$$

$$\beta_{31} = q_{11} + q_{22} \quad (5.25b)$$

$$\beta_{32} = q_{11}k^{-1} + q_{22}k. \quad (5.25c)$$

The first equation in (5.25) yields

$$k = \frac{\beta_{21}}{2} \pm \sqrt{\frac{\beta_{21}^2}{4} - 1}. \quad (5.26)$$

The last equation in (5.25) then gives:

$$q_{22} = \frac{k\beta_{32} - \beta_{31}}{k^2 - 1}. \quad (5.27)$$

The remaining equation can then be solved for

$$q_{11} = \beta_{31} - q_{22}. \quad (5.28)$$

To solve for q_{12} and q_{21} , the symmetry ($q_{12} = -q_{21}$) and reciprocity ($\det(\Sigma \mathbf{C}_{\mathbf{N}}) = 1$) of the network has to be used (see section 2.3.2).

$$q_{21} = \pm \sqrt{1 - q_{11}q_{22}} \quad (5.29)$$

$$q_{12} = -q_{21} \quad (5.30)$$



Figure 5.3: The TTN calibration standards. The top Through measurement is used twice, at two different frequencies.

5.5 Choosing signs

At some places in all the mentioned algorithms, quadratic equations needs to be solved. This means that there will be a sign ambiguity in these equations. This is where the need for some a-priori knowledge comes in. The concerned equations are (5.12), (5.18), (5.19), (5.26) and (5.29).

Information about the **[L]**-network is needed to guess the sign for k . Most often these calibration methods are used in air, and thus the material parameters for the **[L]**-network is known. The only thing that needs to be taken care of is the approximate distance between the different positions.

Then information about the **[Q]**-network is needed to solve for the q_{ij} parameters. This means that the material that is beeing tested can not be totally unknown. The information that is needed is the approximate thickness, d , and refractive index, n .

6

Computer simulation models

To be able to test that the algorithms worked, scattering parameters were needed. To get these scattering parameters simulations were made of three different measurement setups. The three setups were: parallel plate waveguide, tapered coaxial fixture and straight coaxial cable. This chapter will go through the simulations that were made. The commercial FEM program COMSOL Multiphysics was used.

All simulations cover the frequency range $f \in [1, 20]$ GHz (or $\lambda \in [0.3, 0.015]$ m).

6.1 Parallel plate waveguide



Figure 6.1: Photograph of the actual waveguide [46].

In Figure 6.1 a photograph shows the set-up which is going to be simulated, and in Figure 6.2 are the dimensions presented. This simulation is numerically demanding to

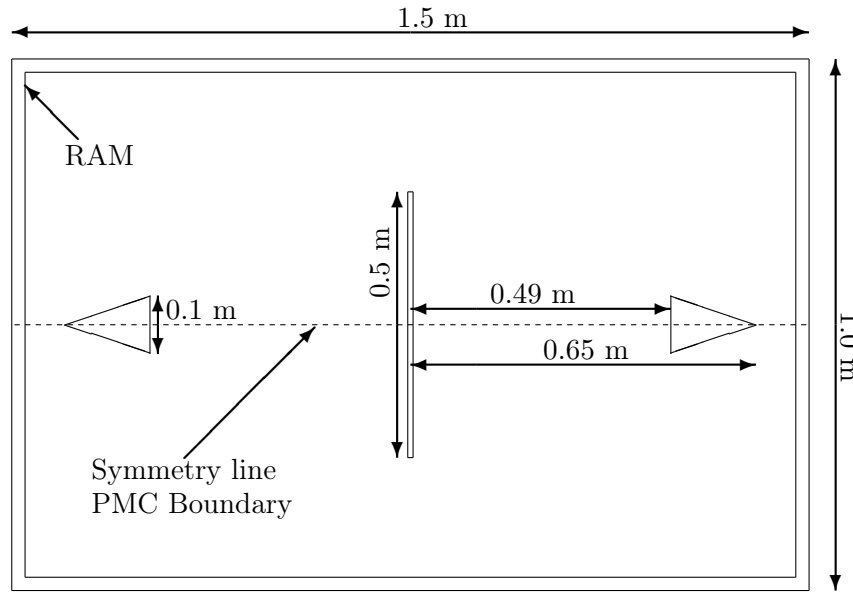


Figure 6.2: The simulated 2D geometry of the parallel plate waveguide. The object in the middle is the material slab used as self-calibration standard. In the simulation it was 2 mm thick. RAM is an abbreviation of Radar-Absorbant Material. The purpose is to have as little field as possible scattered back towards the obstacle. In COMSOL RAM was simulated with a *scattering boundary condition*.

do since the geometry is large, $1\text{ m} \times 1.5\text{ m}$, compared to the wavelengths being simulated. The shortest wavelength is only 1.5 cm long. To capture the behaviour of a wave, a rule of thumb is to have at least 10 elements per λ . This means that the largest allowed element size is very small compared to the geometry that is being simulated. These calculations will require very large amounts of memory if a full 3D simulation was to be done. So the first approximation was to simulate the setup in 2D. The second was to simulate the horn antennas as simple ports which excite a wave.

With these approximation we lose the higher order modes that could propagate in the waveguide (cf. section 2.2.3). The antenna approximation also greatly simplifies the behaviour of a real antenna.

The third trick used was the symmetry in the setup. This is where the mathematical tool of magnetic currents on boundaries are used (cf. eqs. 2.19 in section 2.1.3). This way we reduce the amount of elements by a factor of 2. It is important to remember that this whole toolbox of the PMC boundary (mirroring) is our way of describing nature with our mathematical models.

Figures 6.2-6.4 illustrate the simulation that was set up in COMSOL, and some typical results. A simulation took 20-40 hours depending on the mesh and number of frequency points. For the LNN and Extended LNN algorithms, mentioned in chapter 5, four simulations needs to be performed, resulting in about 160 hours of simulations assuming no failures during simulations.

In the end some unfortunate problems were discovered. The step in frequency were too big, the result of this is shown in Figure 6.5. Another error that was found was a typo

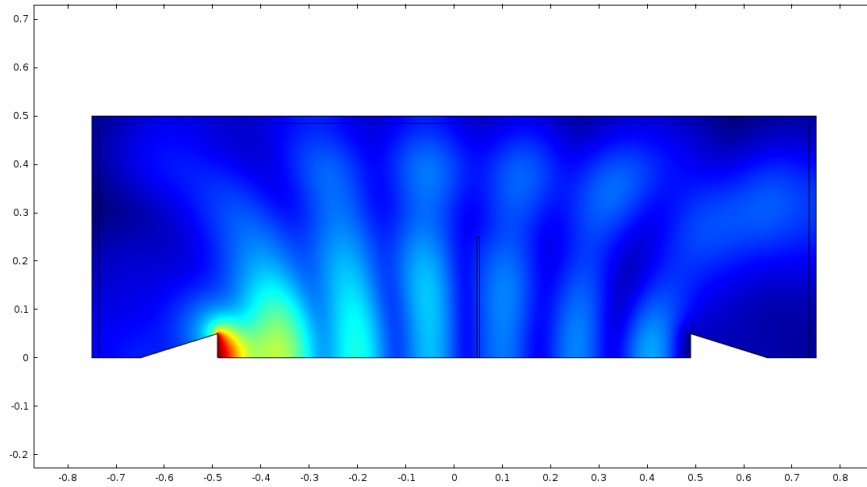


Figure 6.3: The solution from COMSOL calculated at 1 GHz. Here it is clearly shown that it is not yet a plane wave at the obstacle.

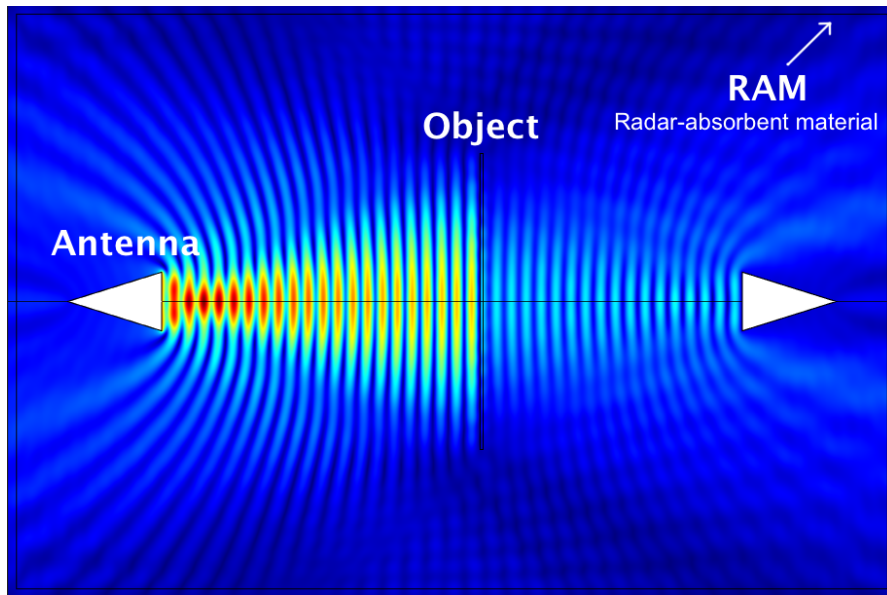


Figure 6.4: The solution from COMSOL calculated at 6 GHz. At around 5 GHz the wave start to appear as plane waves at the obstacle.

made in the COMSOL configuration of the simulation; the propagation constant for the antennas was set in an erroneous way which resulted in a mismatched antenna. This error resulted in a large reflection directly after the port and the effect of this is shown in Figure 6.6 where the reflections (S_{11} and S_{22}) are large. Both these problems should only make the setup worse and were unfortunately detected at the end of the project so there was no time left to perform the lengthy simulations once more.

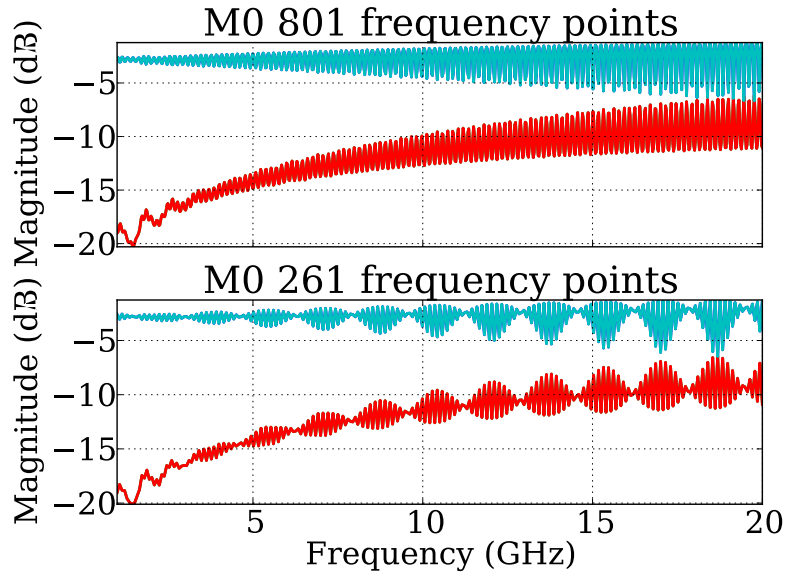


Figure 6.5: Top: 801 frequency points. Bottom: 261 frequency points. The red curve is S_{11} and the blue curve is S_{21} .

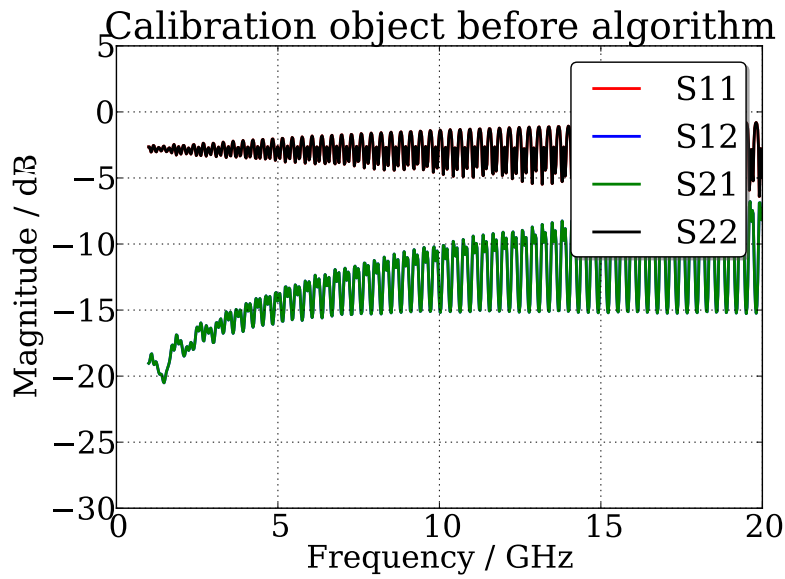


Figure 6.6: The scattering parameters for the object in the middle position. The typo in the COMSOL configuration that resulted in a large reflection directly at the port. Since the simulation is symmetric $S_{11} = S_{22}$ and $S_{12} = S_{21}$ and thus only two lines can be distinguished in the figure.

6.2 Tapered coaxial fixture

The tapered coaxial cable is a lot easier than the parallel plate due to the much smaller size. The first simulations that were made were 2D axis-symmetric, but effects from all higher order modes that can propagate will only appear in a full 3D simulation. The simulated geometry is shown in Figure 6.7 and 6.8 with dimensions presented in section 2.2.4. The total length of the fixture is 11 cm and the tapering parts are 2 cm each. The middle section has a length of 5 cm.

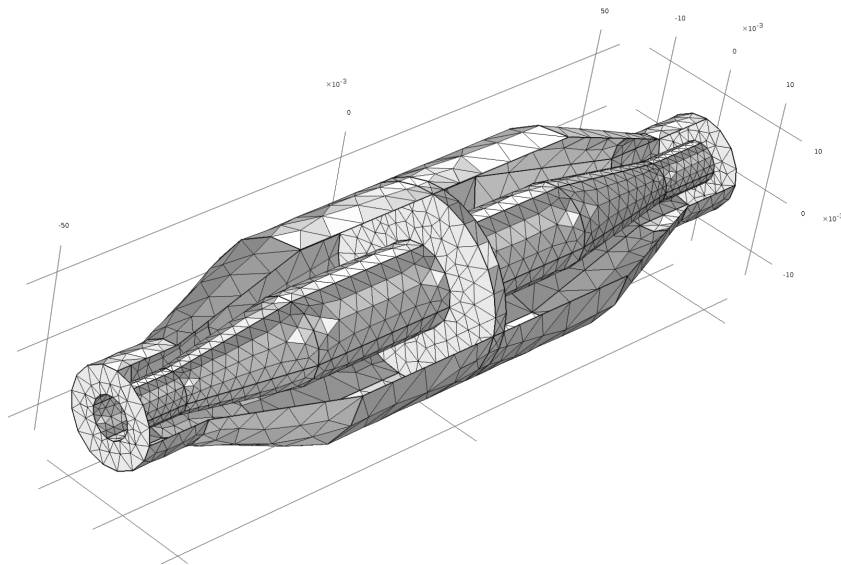


Figure 6.7: The geometry and mesh for the tapered coaxial cable.

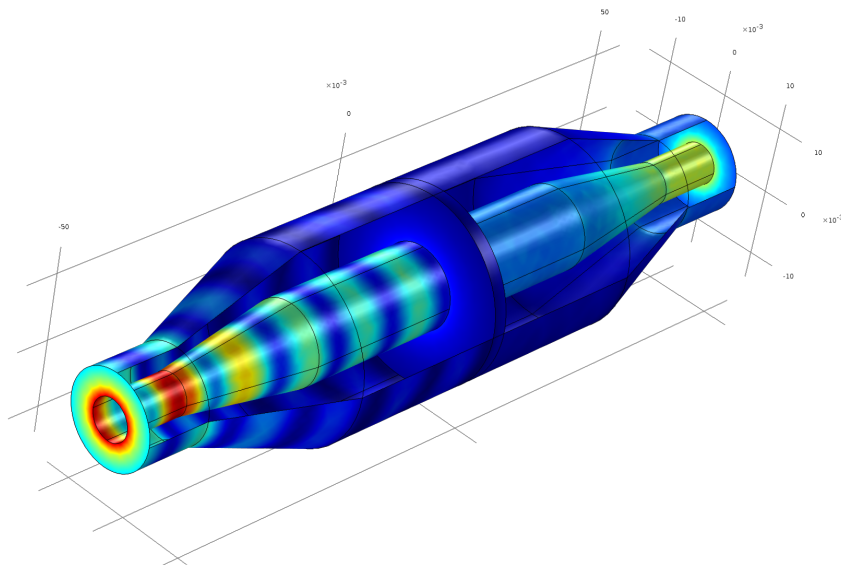


Figure 6.8: Result from a simulation at 15GHz.

6.3 Straight coaxial cable

The straight coaxial waveguide is even easier and the dimensions are the same as the thin parts on the tapered coaxial fixture, i.e. $r_{\text{inner}} = 3.05$ mm and $r_{\text{outer}} = 6.97$ mm. This simulation was also made in both 2D and 3D. The length of the waveguide were set to 11 cm and 1 m and used in the result to compare against the parallel plate and tapered coaxial waveguides. The 2D setup in COMSOL is shown in Figure 6.9.

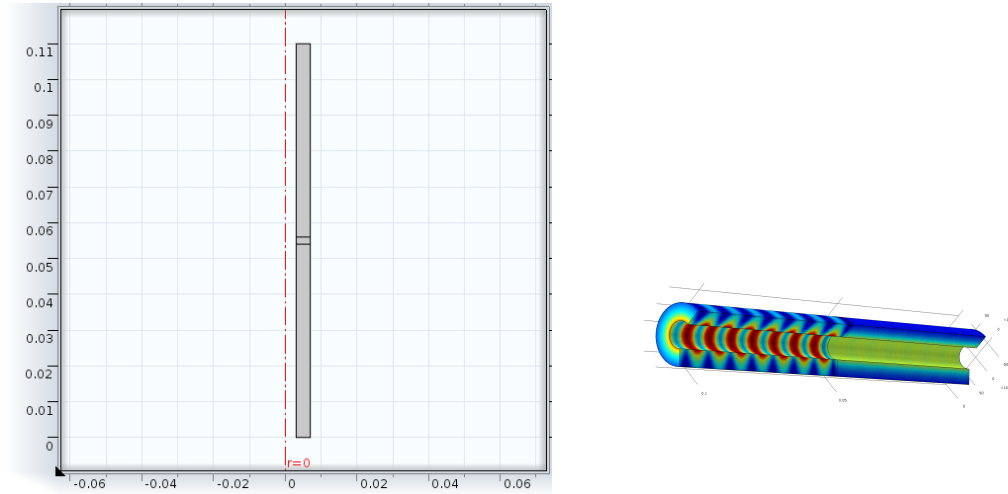


Figure 6.9: **Left.** The symmetrical geometry for the straight coaxial fixture. **Right.** A simulation result at 15 GHz.

Simulated samples

Different setups were simulated to test the algorithms, the setups are

- Set-up 1: Parallel plates, $L = 0.98$ m
- Set-up 2: Tapered coaxial fixture, $L = 0.11$ m
- Set-up 3: Straight coaxial fixture, $L = 1.0$ m

where L is the distance between the antennas/ports. After simulations were done on set-up 1 it became clear that the simulation was under-sampled in frequency (see Figure 6.5). Set-up 1 were then simulated again, with different material parameters (see Table 7.1, 1b). At this point the typo in the propagation constant for the parallel plate was not detected yet. The sample thickness, that has been used in all the set-ups, is 2 mm thick. The simulated samples are presented in Tables 7.1 and 7.2.

Set-up	Self-calibration object			
-	$\text{Re}(\epsilon)$	$-\text{Im}(\epsilon)$	$\text{Re}(\mu)$	$-\text{Im}(\mu)$
1a	2.8	0.0	1.0	0.0
1b	2.8	0.2	1.0	0.0
2	2.8	0.0	1.0	0.0
3	2.8	0.0	1.0	0.0

Table 7.1: The simulated calibration objects material parameters.

Set-up	Post calibration MUT			
-	$\text{Re}(\epsilon)$	$-\text{Im}(\epsilon)$	$\text{Re}(\mu)$	$-\text{Im}(\mu)$
1a	3.4	0.1	1.4	0.0
1b	3.4	0.2	1.5	0.1
2	3.4	0.1	1.5	0.0
3	3.4	0.1	1.5	0.0

Table 7.2: The simulated material slabs material parameters.

8

NRW applied on scattering parameters

To illustrate the importance of a good calibration, the result of applying the NRW algorithm directly on the simulated scattering parameters is shown in this chapter. The only correction that has been made is the move of the planes from the antenna to the edge of the slab. A sample has been put in the middle in each of the three setups. The properties of the sample are: $\epsilon_r = 2.8 - 0.0j$ and $\mu_r = 1.0 - 0.0j$, i.e. it is a lossless nonmagnetic slab. The sample has a thickness of 2 mm. The scale on the y-axis in these plots have *not* been kept fixed in this chapter so it will be easier to see the difference. It should also be mentioned that no additional noise has been added.

Figures 8.1-8.3 shows the relative permittivity and permeability when the NRW algorithm has been applied directly on uncalibrated data from the three simulated setups; parallel plate waveguide, tapered coaxial fixture and the straight coaxial fixture. From these figures it should be clear that, in these set-ups, further calibrations need to be done too achieve higher accuracy in the results.

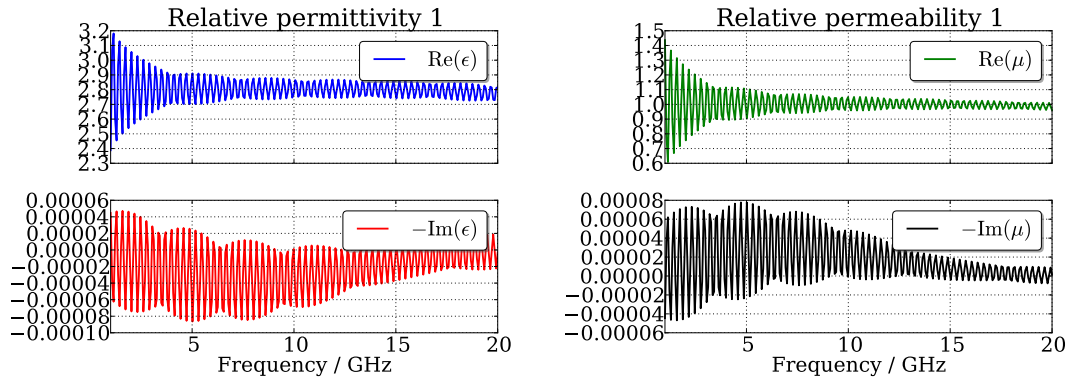


Figure 8.1: The NRW algorithm has been applied directly on uncalibrated data from the parallel plate waveguide simulation. Note that the scale differs from the Real and Imaginary parts.

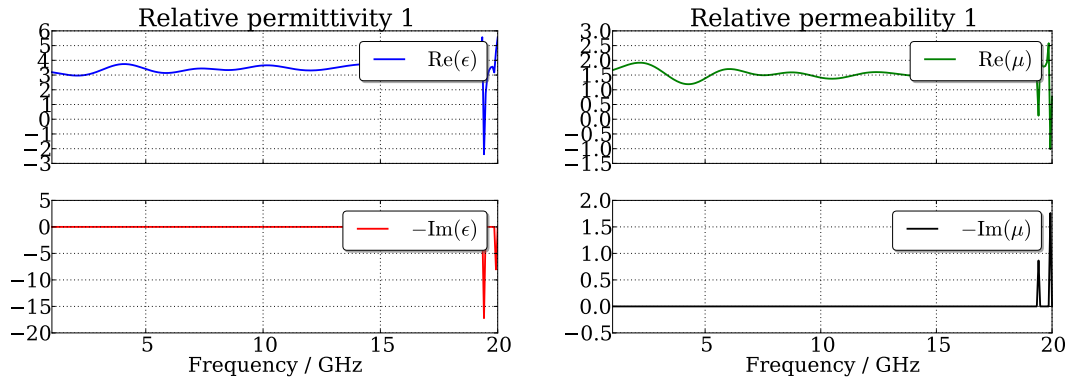


Figure 8.2: The NRW algorithm has been applied directly on uncalibrated data from the tapered coaxial fixture simulation. Note that the scale differs from the Real and Imaginary parts.

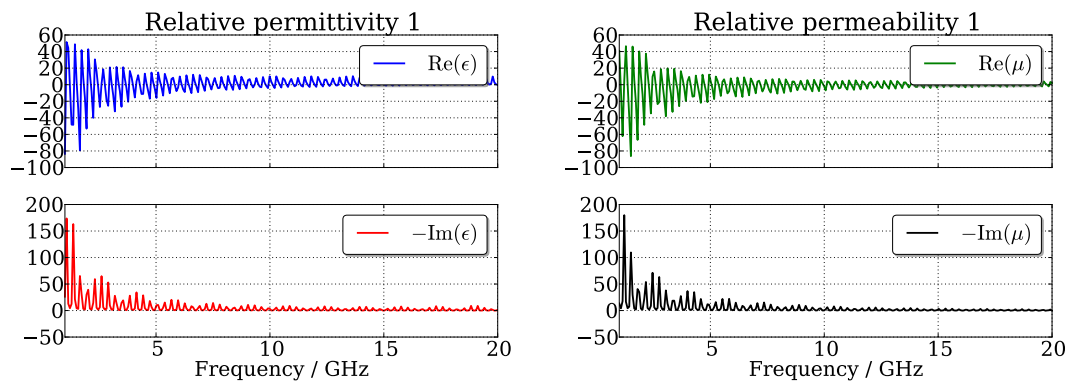


Figure 8.3: The NRW algorithm has been applied directly on uncalibrated data from the straight coaxial fixture simulation. Note that the scale differs from the Real and Imaginary parts.

9

Results and discussion

In this chapter the results of the algorithms will be presented. There are many plots generated during the thesis, and only a selection of them are presented in this chapter, but in appendices A-C all are presented for completeness.

9.1 General

The algorithms have been tested on three different setups (see chapter 7), all simulated in the commercial FEM software COMSOL Multiphysics. When the NRW algorithm has been applied, there have been no assumption about the magnetic properties of the material. The true, simulated, material parameters are presented in Tables 7.1 and 7.2.

As mentioned in chapters 6 and 7 there have been a few problems along the way (under sampled and a typo in the configuration of the simulation). It turns out that all three algorithms managed to calibrate despite this error. For the LNN this can be seen by comparing Figures 6.6 and 9.1. Thus, the results should be able to be used when comparing the methods applied on the different setups, but to eliminate any uncertainties regarding the simulations, they should of course be performed again.

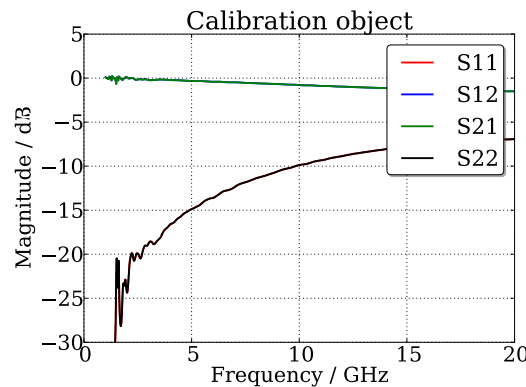


Figure 9.1: The scattering matrix from Figure 6.6 calibrated with the LNN self-calibration algorithm.

In this chapter we will only use the results from the long straight coaxial fixture (Section 2.2.4, and set-up 3 in chapter 7) as a base for the discussions. The same conclusions apply directly to the other set-ups. As previously mentioned, all the figures and plots, from all the simulations, are presented in Appendices A-C.

9.2 LNN and Extended LNN

The sample is put in a 1 meter long straight coaxial fixture. In Figure 9.2 the extracted material parameters, ϵ_r and μ_r are shown. This should be compared to Figure 8.1, then the effect of a good calibration becomes clear.

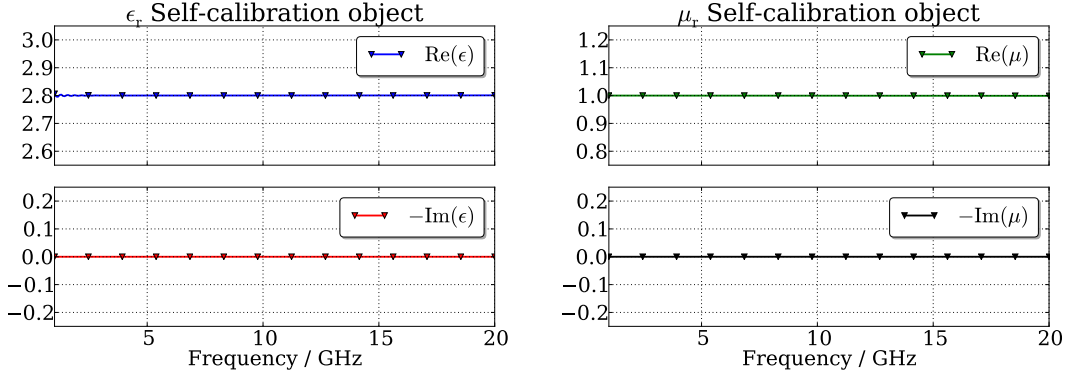


Figure 9.2: The relative permittivity and permeability with the LNN algorithm.

Since the LNN algorithm assumes that the distance, l , between the different calibration steps are equal, Figure 9.3 demonstrates what happens if $l_1 \neq l_2$. In this specific case the sample was only put 0.5 mm out of position.

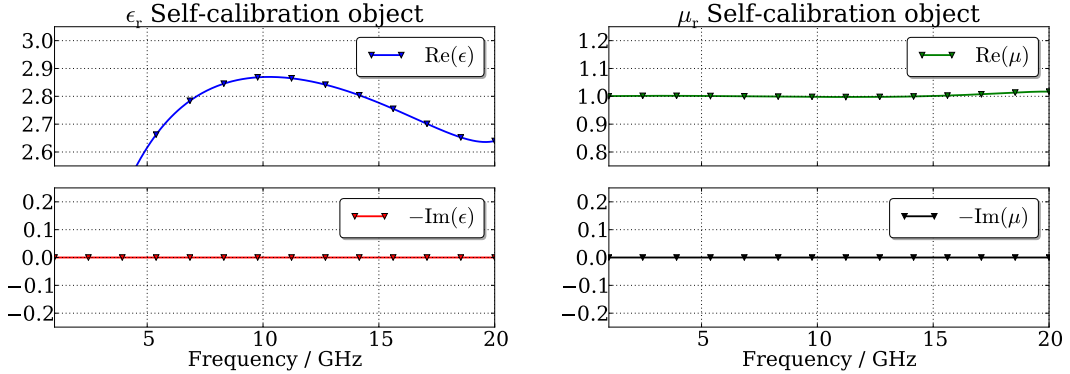


Figure 9.3: The relative permittivity and permeability with the LNN algorithm. In this calibration the L standard varies ($l_1 \neq l_2$).

The Extended LNN algorithm does not assume $l_1 = l_2$, and therefore handles the case of a misaligned sample better, which is shown in Figure 9.4

Since the results from the simulations are, in some sense, free from noise, random noise was added to the scattering matrices before the calibration algorithms were applied. This

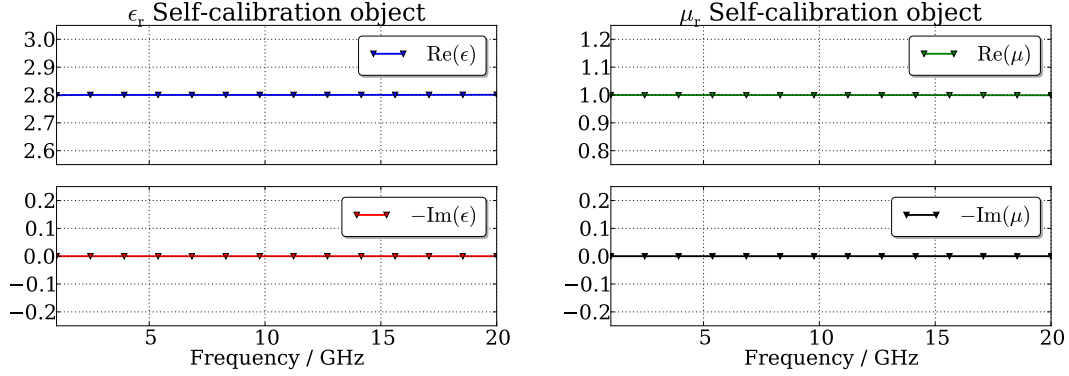


Figure 9.4: The relative permittivity and permeability with the Extended LNN algorithm. In this calibration the L standard varies ($l_1 \neq l_2$).

is done to get a sense of how sensitive the algorithms are. The amplitude of the noise were discussed in section 3.3. The results of the added noise is shown in Figure 9.5.

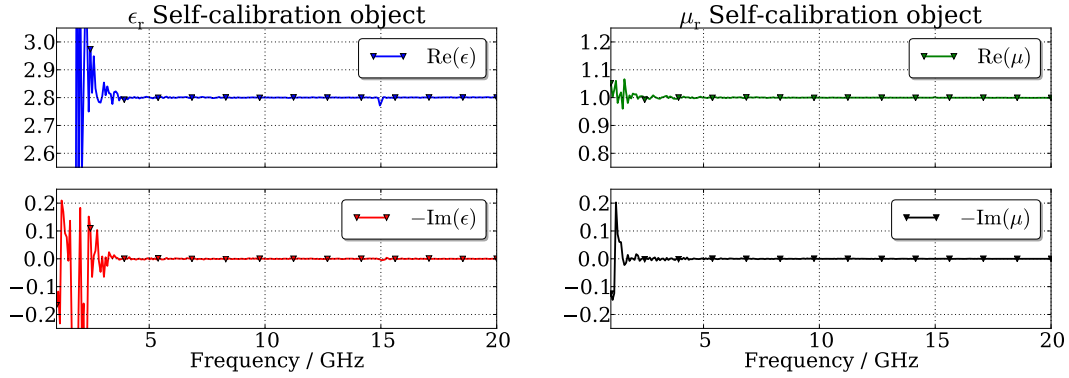


Figure 9.5: The relative permittivity and permeability with the Extended LNN algorithm. After the simulation finished, random noise were added to the data.

If there is uncertainty in the material parameters of the calibration slab, or if the slab itself is constructed with some desired properties, then it is also interesting to see how the algorithms behave when the a-priori knowledge is erroneous. The a-priori guess of the material parameters that is needed was set 20% off. To add to the realism the added noise were kept. The result of this guess is shown in Figure 9.6, and as seen the algorithms are not very sensitive on the initial guess.

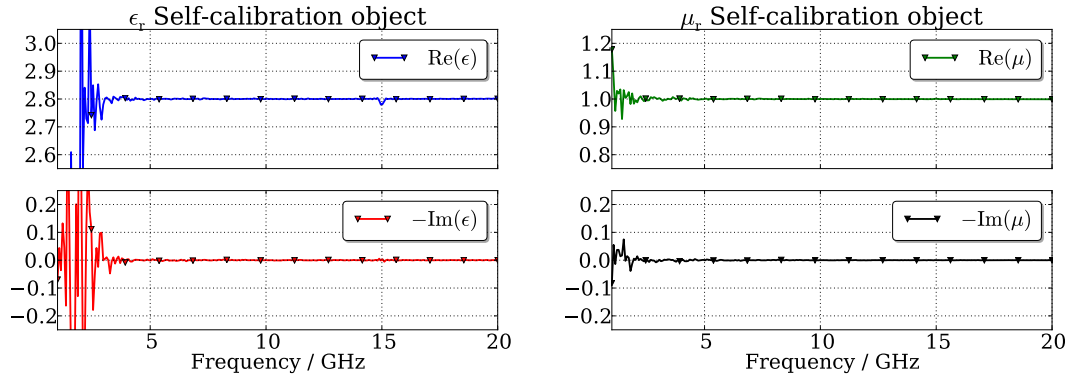


Figure 9.6: The relative permittivity and the relative permeability with the Extended LNN algorithm. After the simulation finished, random noise were added to the data. Then when the algorithms were applied an intended erroneous guess on the a-prior information were made.

9.3 TTN

The TTN algorithm has advantages over the other two self-calibration methods, such as the position of the slab does not have to be precisely known and only two measurements have to be performed; Through and Network. Of course, these advantages does not come without any limitations. The measurement setup has to frequency invariant, for example the antennas must have the same characteristics on a broader bandwidth. A setup with a distance of 1 meter between the antennas, will need a frequency shift of 75 MHz to achieve a phase shift of approximately 90° .

In Figure 9.7 the material parameters are shown after a TTN calibration has been performed. Only two simulations were made; one through measurement and one with the sample in the middle. To obtain the Line standard that was described in section 5.4, a frequency shift of 73.1 MHz was achieved by shifting the results of the through-simulation in frequency. In the 1 m long straight coaxial fixture this corresponds to phase shift of 87.78° .

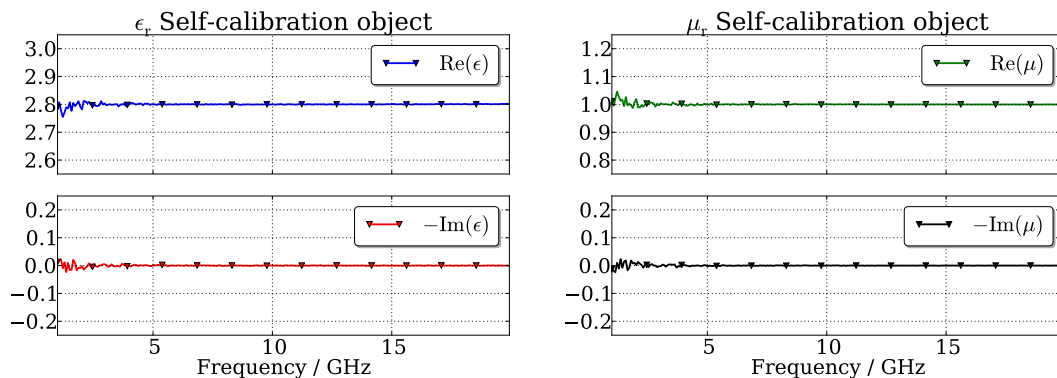


Figure 9.7: The relative permittivity and permeability with the TTN algorithm. After the simulation finished, random noise were added to the data. Then when the algorithms were applied an intended erroneous guess were made.

9.4 Statistics

Since the simulations are deterministic (except for numerical noise), noise has been added to the scattering parameters before the calibration methods were applied. Gaussian noise was added on both the real and imaginary parts. After the self-calibration, the NRW algorithm was applied which gives the relative permittivity and the relative permeability. This procedure was repeated $2 \cdot 2000$ times to generate statistics on the results. On the first 2000 samples a normal distributed noise was added with standard deviation 0.0001, $\mathcal{N}_1 = \mathcal{N}(0, 10^{-4})$, which corresponds to what have been observed in real measurements. To test how the algorithms handle more noise another 2000 calibrations were performed this time the normally distributed noise had a standard deviation of 0.001, $\mathcal{N}_2 = \mathcal{N}(0, 10^{-3})$. The results are shown in Figures 9.8 - 9.10. The mean value and standard deviation at 10 GHz are presented in Tables 9.1 and 9.2 where $E[\cdot]$ denotes the mean value and $\sigma[\cdot]$ denotes the standard deviation.

@10 GHz	LNN	E-LNN	TTN
$E[\epsilon_r]$	$2.79378 + 0.00882j$	$2.80009 - 0.00001j$	$2.80005 - 0.00003j$
$E[\mu_r]$	$0.99956 - 0.00041j$	$0.99983 - 0.00000j$	$1.00002 + 0.00002j$

Table 9.1: The mean value of ϵ_r and μ_r at 10 GHz. Here \mathcal{N}_1 has been used.

@10 GHz	LNN	E-LNN	TTN
$\sigma[\text{Re}(\epsilon_r)]$	0.00127	0.00194	0.00161
$\sigma[\text{Im}(\epsilon_r)]$	0.00125	0.00196	0.00163
$\sigma[\text{Re}(\mu_r)]$	0.00117	0.00120	0.00123
$\sigma[\text{Im}(\mu_r)]$	0.00119	0.00122	0.00120

Table 9.2: The standard deviation of ϵ_r and μ_r at 10 GHz. Here \mathcal{N}_1 has been used.

Just by looking at the figures the TTN algorithm looks like the best choice, in this particular setup, due to the standard deviation at low frequencies for the \mathcal{N}_1 distributed noise. But at 10 GHz there is clearly little difference between the algorithms.

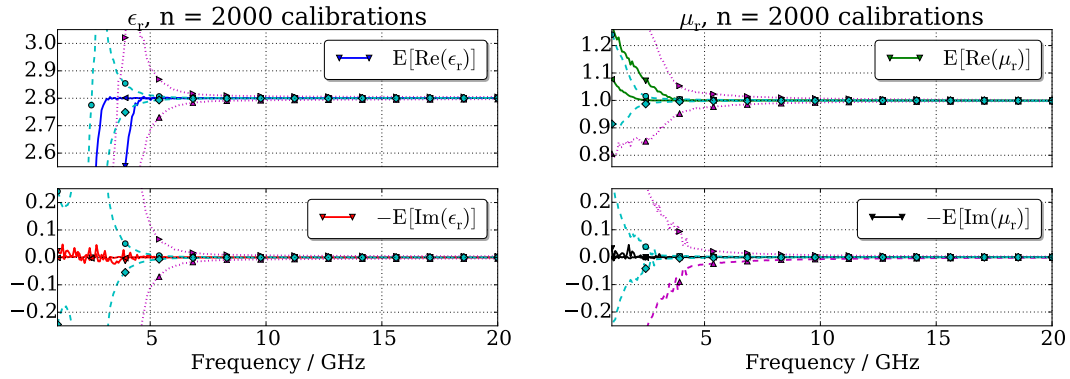


Figure 9.8: The LNN algorithm run 2000 times, then the NRW applied on the 2000 data sets. The dashed (cyan) line is the standard deviation when \mathcal{N}_1 distributed noise were used, and the dotted (purple) line is the standard deviation when \mathcal{N}_2 distributed noise were used.

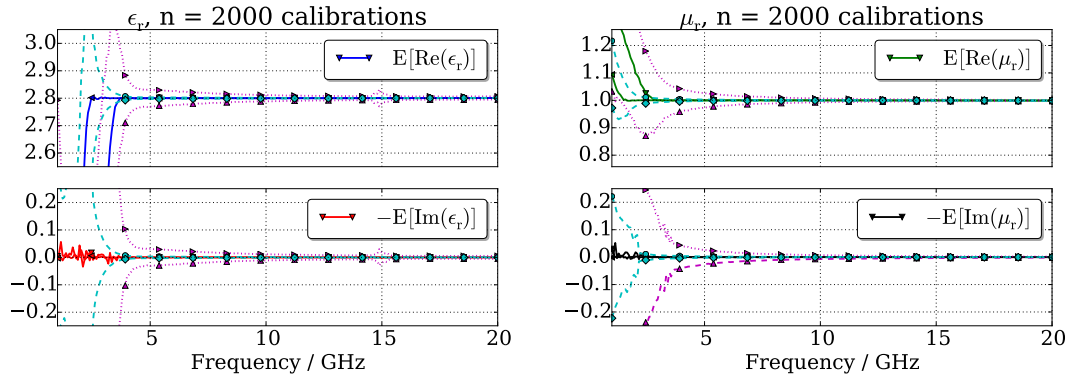


Figure 9.9: The Extended LNN algorithm run 2000 times, then the NRW applied on the 2000 data sets. The dashed (cyan) line is the standard deviation when \mathcal{N}_1 distributed noise were used, and the dotted (purple) line is the standard deviation when \mathcal{N}_2 distributed noise were used.

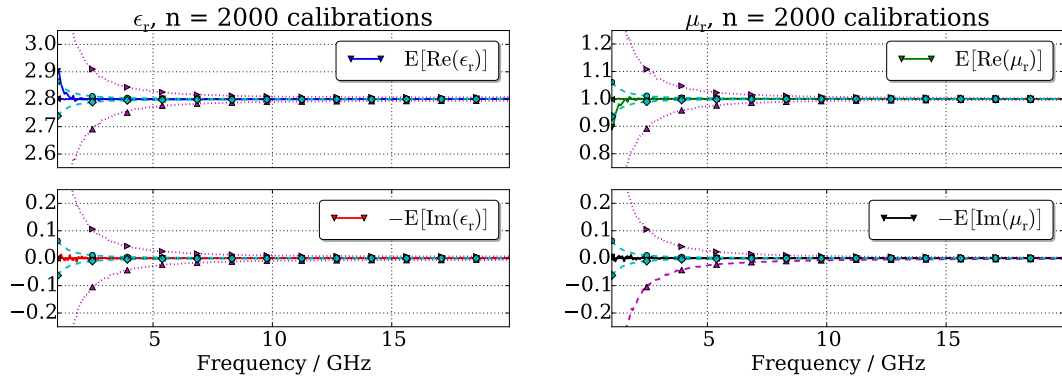


Figure 9.10: The TTN algorithm run 2000 times, then the NRW applied on the 2000 data sets. The dashed (cyan) line is the standard deviation when \mathcal{N}_1 distributed noise were used, and the dotted (purple) line is the standard deviation when \mathcal{N}_2 distributed noise were used.

9.5 Discussion of the self-calibrations

At lower frequencies, around 1-5 GHz, the results get much worse when adding random noise (cf. Figure 9.5-9.10). This can in part be due to the Cramer-Rao bounds which are discussed in [47]. The bounds state the best possible results that can be obtained from a measurement on a specific setup assuming that all systematic errors have been removed through e.g. calibration.

In Figures 9.6 and 9.9 the Extended-LNN algorithm has ripples at 15 GHz. The half wavelength at this frequency is approximately 1 cm, which coincides with sum of the [L]-standards. In the Extended-LNN algorithm a change of sign of the real part of k_2 in equations (5.18) to make them continuous, see Figures 9.11 and 9.12. As discussed in section 5.5 there are several quadratic equations that needs to be solved. It is from here the problems of sign arise. The solution to this is a-prior knowledge like symmetry and passivity.

At higher frequencies there might be new, higher modes of waves propagating in the setup. This problem is clearly visible in the full 3D simulation of the short tapered coaxial fixture (cf. Figure 8.2).

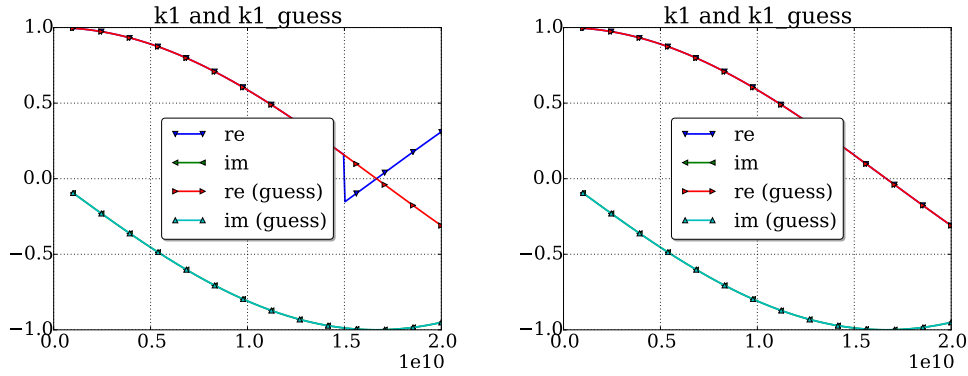


Figure 9.11: The impact of choosing the wrong sign on k_2 in the Extended-LNN algorithm.

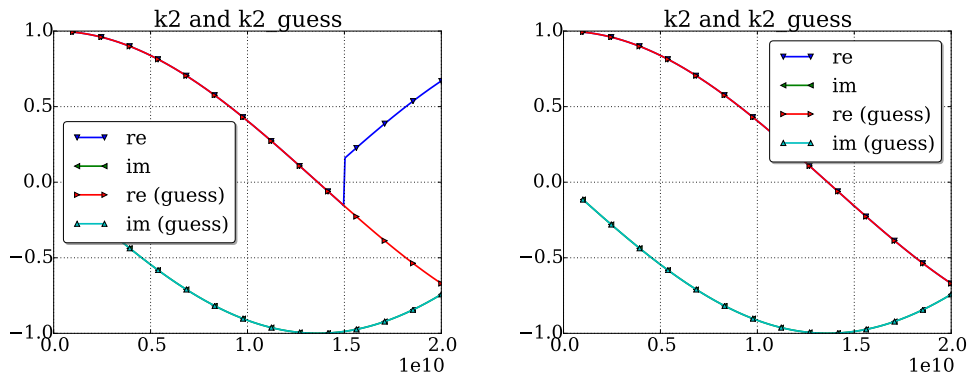


Figure 9.12: The impact of choosing the wrong sign on k_2 in the Extended-LNN algorithm.

9.6 Post calibration DUT

Once the self-calibration has been performed one can replace the calibration slab with another slab, with different material properties. This is shown for the three algorithms in Figures 9.13-9.15. The calibrations were made with noisy data.

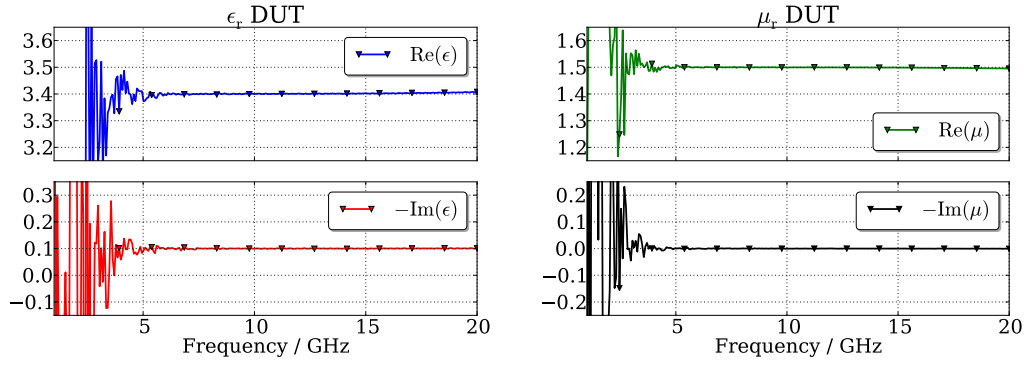


Figure 9.13: The relative permittivity and permeability of another MUT with the LNN algorithm.

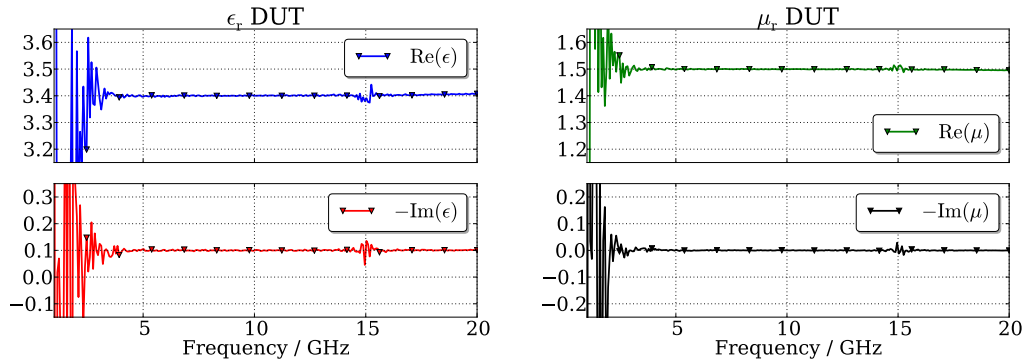


Figure 9.14: The relative permittivity and permeability of another MUT with the Extended-LNN algorithm.

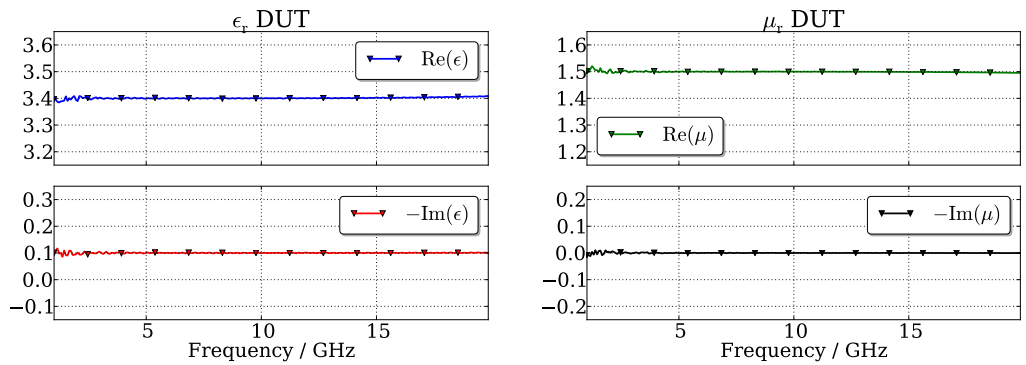


Figure 9.15: The relative permittivity and permeability of another MUT with the TTN algorithm.

9.7 Conclusions

These calibration methods look promising with the results presented in this thesis as a base. They fill a purpose when working with measurement setups that can not be altered in an easy manner, e.g. when the ports/antennas are fixed. The fact that the three investigated algorithms are self-calibration methods and hence the slab or device that is under test is one of the calibration standards eliminates the need for expensive, well-known, standards.

As can be seen in section 9.4 all three algorithms seem stable, if we disregard lower frequencies, that in part might relate to the Cramér-Rao lower bounds. Of course the calibration becomes impossible to do if unwanted higher order modes start to propagate in the setup.

The TTN algorithm has the advantage of being a simple setup (in free space). On the other hand the setup, e.g. antennas, have to have a flat frequency response, and the setup should be quite long (≈ 1 m) to keep the frequency shift as small as possible.

For the NRW algorithm, the thickness of the slab has to be known with high accuracy in order to get good parameters, S_{11} and S_{21} , as input. This accuracy depends on the highest frequency, since a higher frequency leads to greater phase error if the thickness is erroneous. The position of the slab is also important, especially if one wish to use the calibration on a different DUT. Since the error in position is captured in the self-calibration for the calibration object, this DUT is not sensitive to an erroneous a-priori guess.

All the algorithms have been implemented with python, and with a very useful module called scikit-rf [39] which implements electrical networks and an easy way to work with Touchstone files. Another, obvious, benefit is the open-source aspect of python and its modules, which reduces cost of licenses.

In the future, these algorithms should be applied on real measurements to check how stable they are and how sensitive they are to real noise.

Bibliography

- [1] R. W. Anderson and O. T. Dennison, "An Advanced New Network Analyzer for Sweep-Measuring Amplitude and Phase from 0.1 to 12.4 GHz," *Hewlett-Packard Journal*, no. February 1967, pp. 2–9, 1967.
- [2] D. R. Gildea and W. A. Rytand, "Network Analysis in the Range 100 kHz to 110 MHz," *Hewlett-Packard Journal*, no. December 1969, pp. 2–11, 1969.
- [3] R. A. Hackborn, "An automatic network analyzer system," *Microwave Journal*, vol. 11, pp. 45–52, 1968.
- [4] D. K. Rytting and S. Steven Neil, "A System for Automatic Network Analysis," *Hewlett-Packard Journal*, no. February 1970, pp. 2–10, 1970.
- [5] (2010, July). [Online]. Available: http://commons.wikimedia.org/wiki/File:Agilent_N5245A_PNA-X.jpg
- [6] E. Matthews, "The use of scattering matrices in microwave circuits," *Microwave Theory and Techniques, IRE Transactions on*, vol. 3, no. 3, pp. 21–26, 1955.
- [7] K. Kurokawa, "Power waves and the scattering matrix," *Microwave Theory and Techniques, IEEE Transactions on*, vol. 13, no. 2, pp. 194–202, 1965.
- [8] A. M. Nicolson and G. F. Ross, "Measurement of the intrinsic properties of materials by time-domain techniques," *IEEE Transactions on Instrumentation and Measurement*, vol. 19, no. 4, pp. 377–382, November 1970.
- [9] W. B. Weir, "Automatic measurement of complex dielectric constant and permeability at microwave frequencies," *Proceedings of the IEEE*, vol. 62, no. 1, pp. 33–36, January 1974.
- [10] N. J. Damaskos, R. B. Mack, A. L. Maffett, W. Parmon, and P. Uslenghi, "The inverse problem for biaxial materials," *Microwave Theory and Techniques, IEEE Transactions on*, vol. 32, no. 4, pp. 400–405, 1984.
- [11] D. K. Ghodgaonkar, V. V. Varadan, and V. K. Varadan, "A free-space method for measurements of dielectric constants and loss tangents at microwave frequencies," *IEEE Transactions on Instrumentation and Measurement*, vol. 37, no. 3, pp. 789–793, 1989.
- [12] D. R. Smith, S. Schultz, P. Markoš, and C. M. Soukoulis, "Determination of effective permittivity and permeability of metamaterials from reflection and transmission coefficients," *Phys. Rev. B*, vol. 65, p. 195104, Apr 2002.
- [13] X. Chen, T. M. Grzegorzczuk, B.-I. Wu, J. Pacheco, and J. A. Kong, "Robust method to retrieve the constitutive effective parameters of metamaterials," *Phys. Rev. E*, vol. 70, p. 016608, Jul 2004.

- [14] J. Barroso and A. De Paula, "Retrieval of permittivity and permeability of homogeneous materials from scattering parameters," *Journal of Electromagnetic Waves and Applications*, vol. 24, no. 11-12, pp. 1563–1574, 2010.
- [15] O. Luukkonen, S. I. Maslovski, and S. A. Tretyakov, "A stepwise Nicolson–Ross–Weir-based material parameter extraction method," *Antennas and Wireless Propagation Letters, IEEE*, vol. 10, pp. 1295–1298, 2011.
- [16] A. L. de Paula, J. Barroso, and M. Rezende, "Modified Nicolson-Ross-Weir (NRW) method to retrieve the constitutive parameters of low-loss materials," in *Microwave & Optoelectronics Conference (IMOC), 2011 SBMO/IEEE MTT-S International*. IEEE, 2011, pp. 488–492.
- [17] M. C. Ricci, H. Xu, R. Prozorov, A. P. Zhuravel, A. V. Ustinov, and S. M. Anlage, "Tunability of superconducting metamaterials," *IEEE Transactions on Applied Superconductivity*, vol. 17, no. 2, pp. 918–921, 2007.
- [18] M. M. Bait-Suwailam, M. S. Boybay, and O. M. Ramahi, "Electromagnetic coupling reduction in high-profile monopole antennas using single-negative magnetic metamaterials for MIMO applications," *IEEE Transactions on Antennas and Propagation*, vol. 58, no. 9, pp. 2894–2902, 2010.
- [19] D. Shrekenhamer, W. Xu, S. Venkatesh, D. Schurig, S. Sonkusale, and W. J. Padilla, "Experimental realization of a metamaterial detector focal plane array," *Physical Review Letters*, vol. 109, no. 17, pp. 24–28, 2012.
- [20] P. V. Kapitanova, A. P. Slobozhnanyuk, I. V. Shadrivov, P. a. Belov, and Y. S. Kivshar, "Competing nonlinearities with metamaterials," *Applied Physics Letters*, vol. 101, no. 23, pp. 1–4, 2012.
- [21] I. Vakili, "Metamaterial forward scattering measurements in a waveguide," Master's thesis, Lund University, 2011.
- [22] Agilent, *Application Note 1287-2 Exploring the Architectures of Network Analyzers*, Agilent Technologies, 2000.
- [23] —, *Application Note 1287-3 Applying Error Correction to Network Analyzer Measurements*, Agilent Technologies, 2002.
- [24] —, *Application Note 1287-9 In-Fixture Measurements Using Vector Network Analyzers*, Agilent Technologies, 2006.
- [25] —, *Application Note 1364-1 De-embedding and Embedding S-Parameter Networks Using a Vector Network Analyzer*, Agilent Technologies, 2004.
- [26] H. Eul and B. Schiek, "A generalized theory and new calibration procedures for network analyzer self-calibration," *Microwave Theory and Techniques, IEEE Transactions on*, vol. 39, no. 4, pp. 724–731, 1991.
- [27] G. Engen and C. Hoer, "Thru-Reflect-Line: An Improved Technique for Calibrating the Dual Six-Port Automatic Network Analyzer," *IEEE Transactions on Microwave Theory and Techniques*, vol. 27, no. 12, 1979.

-
- [28] H. Heuermann and B. Schiek, "Line network network (LNN): An alternative in-fixture calibration procedure," *Microwave Theory and Techniques, IEEE Transactions on*, vol. 45, no. 3, pp. 408–413, 1997.
- [29] I. Rolfes and B. Schiek, "LRR - A self-calibration technique for the calibration of vector network analyzers," *Instrumentation and Measurement, IEEE Transactions on*, vol. 52, no. 2, pp. 316–319, 2003.
- [30] —, "Calibration methods for microwave free space measurements," *Advances in Radio Science*, vol. 2, no. 1, pp. 19–25, 2005.
- [31] —, "Self-calibration procedures for vector network analyzers on the basis of reflection standards," in *Microwave Conference, 2003. 33rd European*. IEEE, 2003, pp. 93–96.
- [32] B. Will and I. Rolfes, "The TTN-method-a phase shift calibration technique for vector network analyzers," in *Microwave Conference Proceedings (APMC), 2011 Asia-Pacific*. IEEE, 2011, pp. 697–700.
- [33] E. Hinton and B. Irons, "Least squares smoothing of experimental data using finite elements," *Strain*, vol. 4, no. 3, pp. 24–27, 1968.
- [34] A. Taflov, "Application of the finite-difference time-domain method to sinusoidal steady-state electromagnetic-penetration problems," *Electromagnetic Compatibility, IEEE Transactions on*, no. 3, pp. 191–202, 1980.
- [35] R. F. Harrington and J. L. Harrington, *Field computation by moment methods*. Oxford University Press, 1996.
- [36] (2015, March). [Online]. Available: <http://www.eda.org/ibis/>
- [37] IBIS Open Forum, *Touchstone File Format Specification Version 2.0*, Agilent Technologies, 2009.
- [38] [Online]. Available: <https://www.scipy.org/>
- [39] [Online]. Available: <http://scikit-rf-web.readthedocs.org/>
- [40] S. J. Orfanidis, *Electromagnetic Waves and Antennas*. Rutgers University, 2010.
- [41] D. J. Griffiths, *Introduction to Electrodynamics*, 3rd ed. Pearson Benjamin Cummings, 2008.
- [42] D. M. Pozar, *Microwave Engineering*, 4th ed. John Wiley and Sons, Inc., 2011.
- [43] A. Karlsson and G. Kristensson, *Microwave Theory*. KFS AB, 2012.
- [44] J. D. Jackson, *Classical Electrodynamics*, 3rd ed. John Wiley and Sons, Inc., 1998.
- [45] D. Rytting, "Network analyzer error models and calibration methods," Agilent Technologies Presentation.
- [46] I. Vakili, M. Gustafsson, D. Sjöberg, R. Seviour, M. Nilsson, and S. Nordebo, "Sum Rules for Parallel Plate Waveguides: Experimental Results and Theory," *IEEE*
-

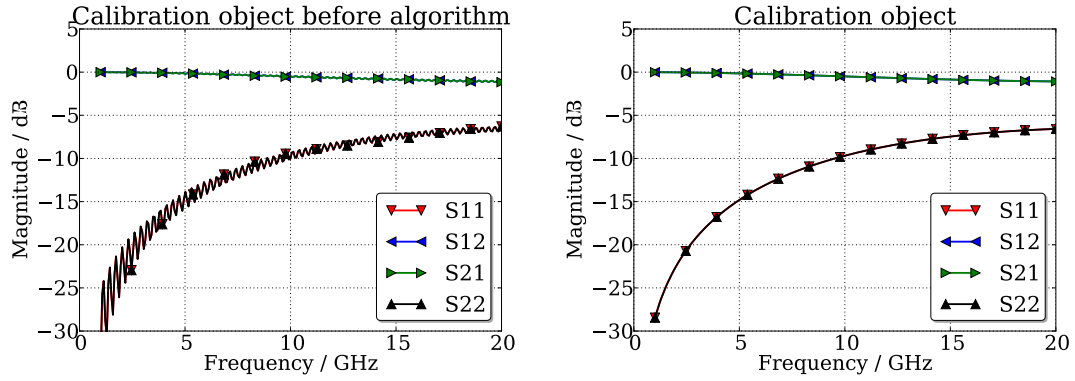
- Transactions on Microwave Theory and Techniques*, vol. 62, no. 11, pp. 2574–2582, 2014. [Online]. Available: <http://dx.doi.org/10.1109/TMTT.2014.2354592>
- [47] D. Sjöberg and C. Larsson, “Cramér–rao bounds for determination of permittivity and permeability in slabs,” *Microwave Theory and Techniques, IEEE Transactions on*, vol. 59, no. 11, pp. 2970–2977, 2011.



LNN

This appendix contains all results for the LNN algorithm. The algorithm was applied on three different, simulated setups; a straight coaxial fixture, a tapered coaxial fixture and a parallel plate waveguide (presented in detail in chapters 6 and 7).

A.1 Straight coaxial cable or fixture



(a) The scattering parameters for the object in the middle position.

(b) The scattering parameters for the object after self-calibration.

Figure A.1: The self-calibration object before and after the procedure.

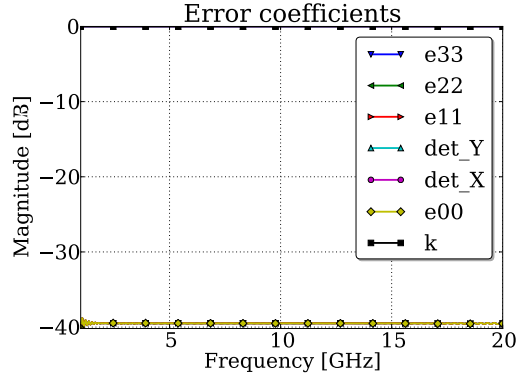


Figure A.2: The error coefficients.

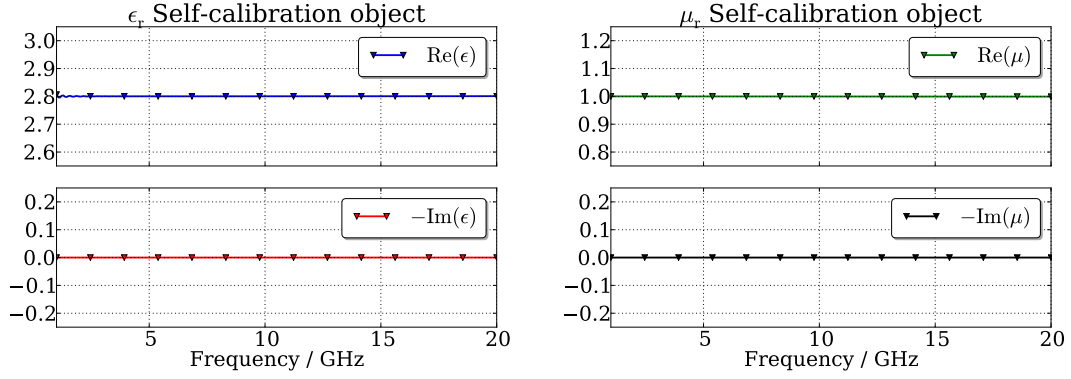
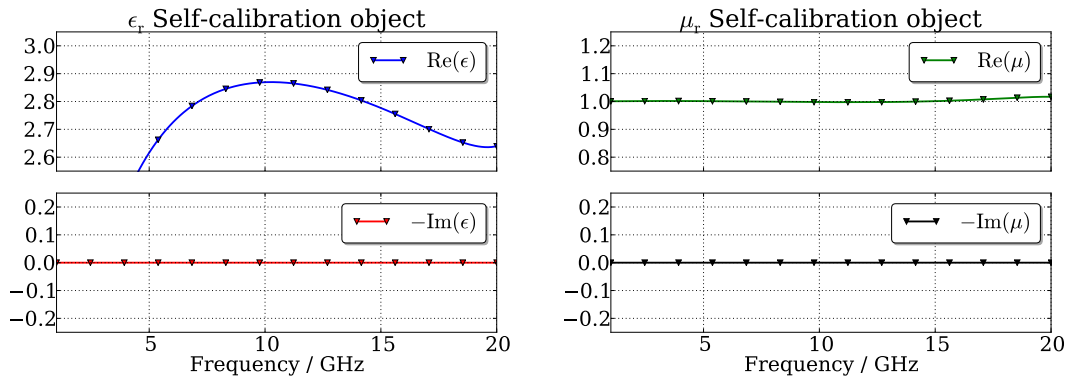


Figure A.3: The relative permittivity and permeability with the LNN algorithm. A 1 m long straight coaxial waveguide setup simulated (full 3D) in COMSOL and no white noise added.


 Figure A.4: The relative permittivity and permeability with the LNN algorithm. A 1 m long straight coaxial waveguide setup simulated (full 3D) in COMSOL and no white noise added. But in this calibration the L standard varies ($l_1 \neq l_2$).

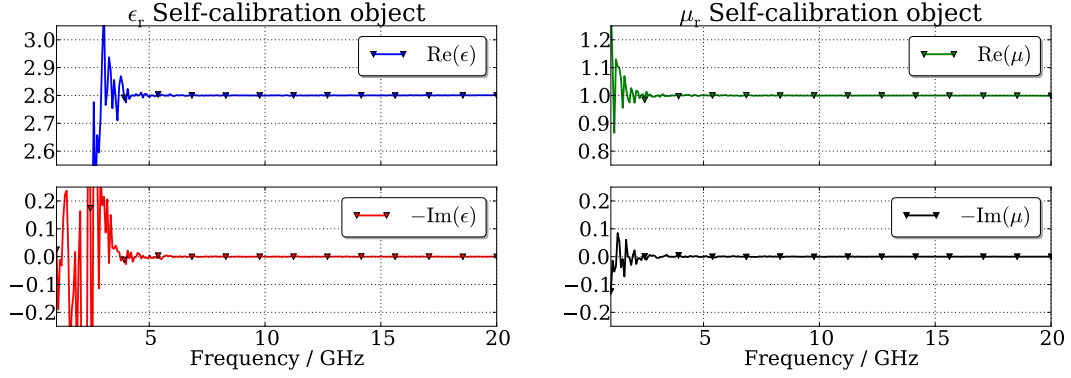


Figure A.5: The relative permittivity and permeability with the LNN algorithm. A 1 m long straight coaxial waveguide setup simulated (full 3D) in COMSOL then numeric white noise added.

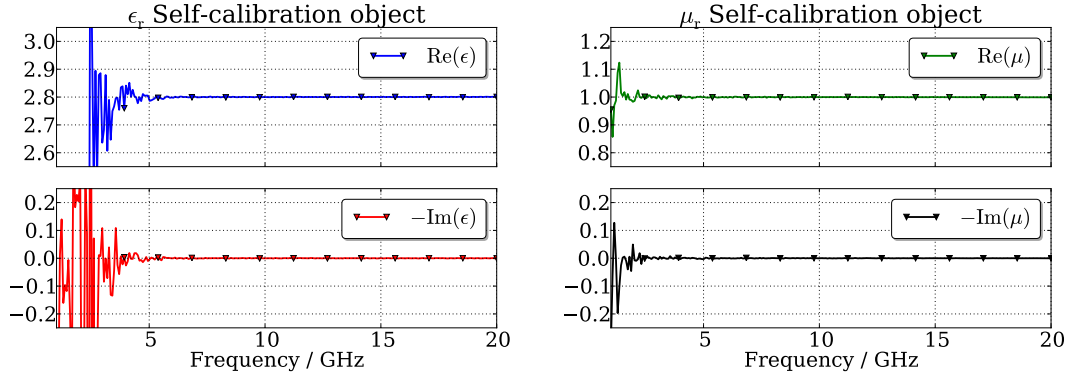


Figure A.6: The relative permittivity and permeability with the LNN algorithm. A 1 m long straight coaxial waveguide setup simulated (full 3D) in COMSOL. In this pair of plots the a-priori information on ϵ_r is 20% off and white noise is added.

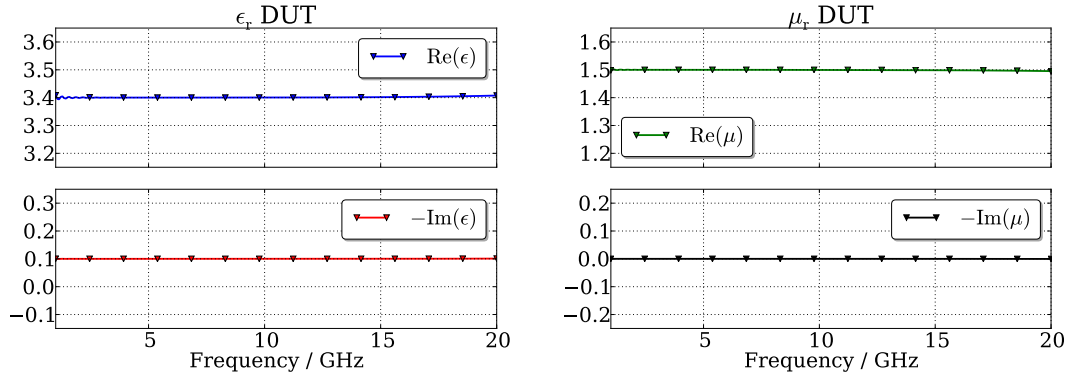
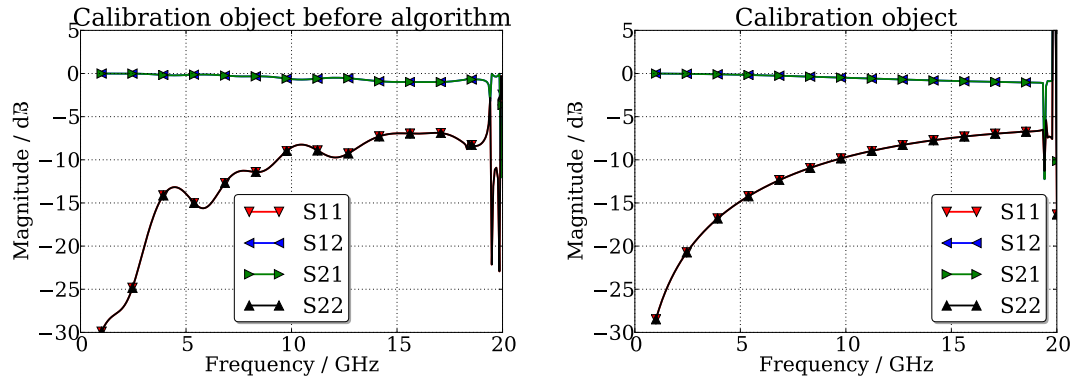


Figure A.7: Once the error networks have been characterized one can remove the sample used during calibration and insert another sample.

A.2 Tapered coaxial cable



(a) The scattering parameters for the object in the middle position.

(b) The scattering parameters for the object after self-calibration.

Figure A.8: The self-calibration object before and after the procedure.

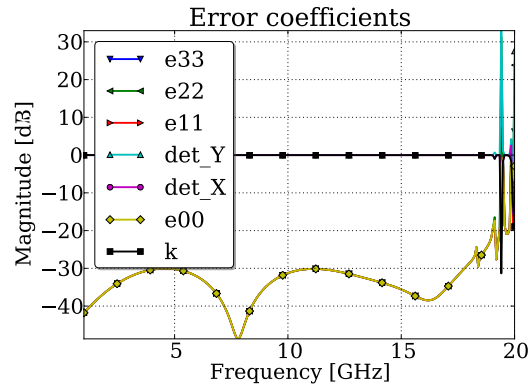


Figure A.9: The error coefficients.

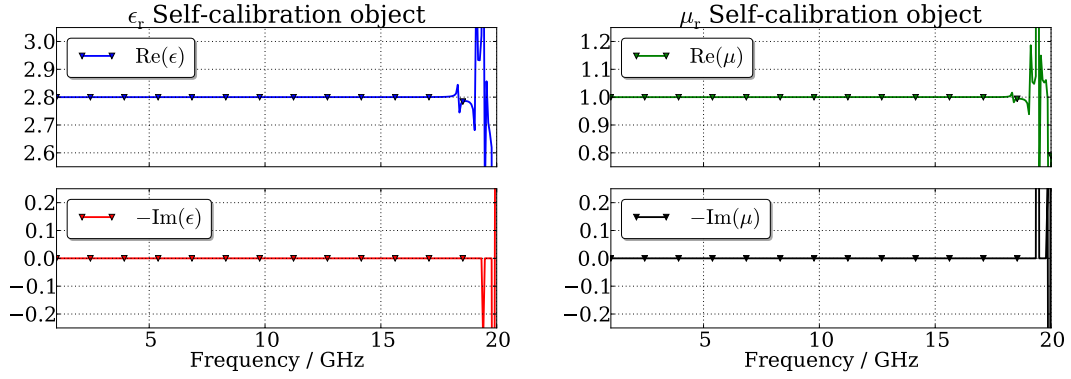


Figure A.10: The relative permittivity and permeability with the LNN algorithm. A 11 cm long tapered coaxial waveguide setup simulated (full 3D) in COMSOL and no white noise added.

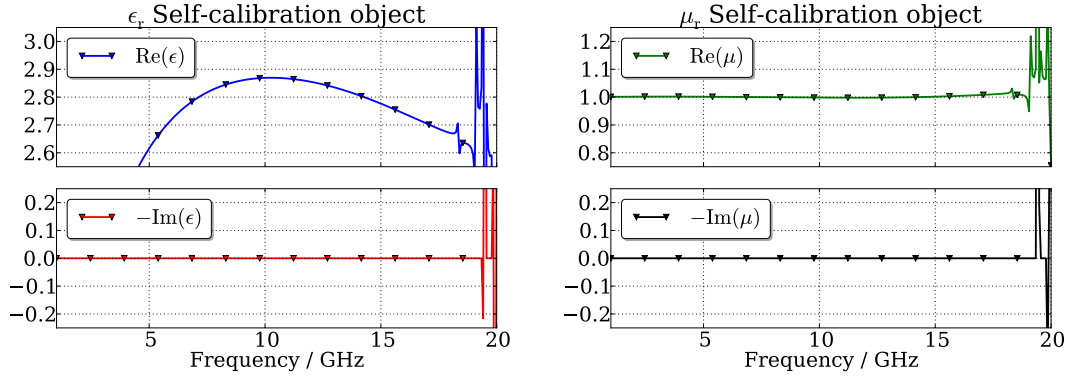


Figure A.11: The relative permittivity and permeability with the LNN algorithm. A 11 cm long tapered coaxial waveguide setup simulated (full 3D) in COMSOL and no white noise added. But in this calibration the L standard varies ($l_1 \neq l_2$).

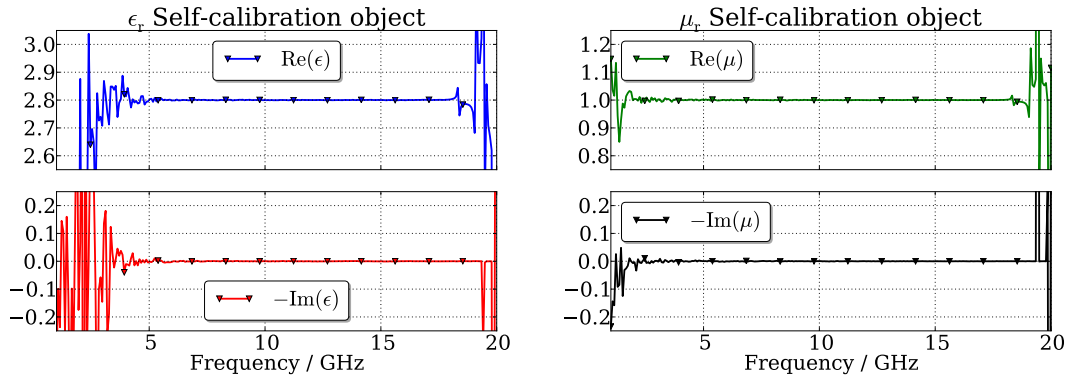


Figure A.12: The relative permittivity and permeability with the LNN algorithm. A 11 cm long tapered coaxial waveguide setup simulated (full 3D) in COMSOL then numeric white noise added.

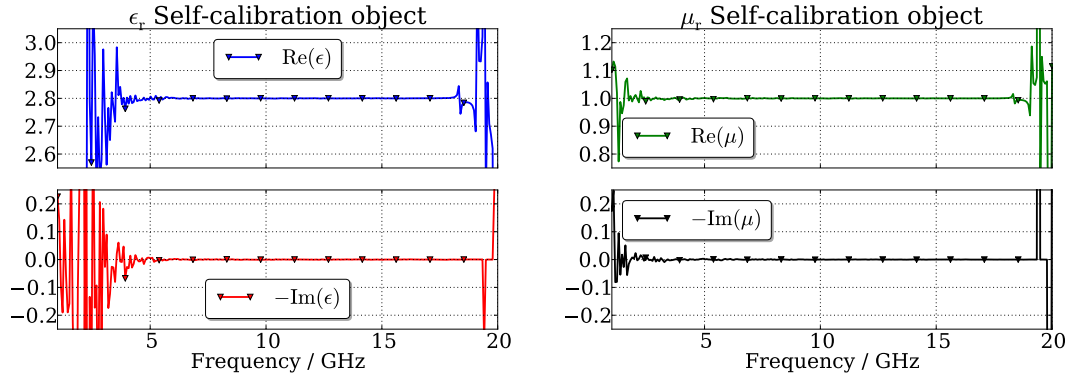


Figure A.13: The relative permittivity and permeability with the LNN algorithm. A 11 cm long tapered coaxial waveguide setup simulated (full 3D) in COMSOL. In this pair of plots the a-priori information on ϵ_r is 20% off and white noise is added.

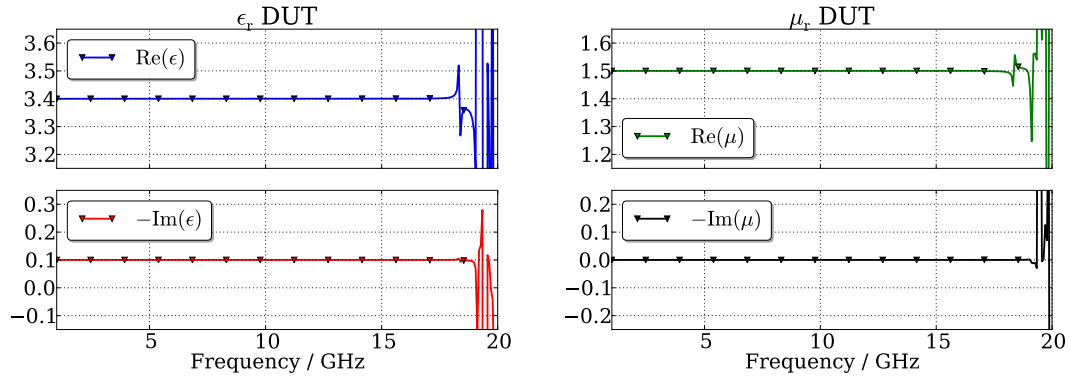
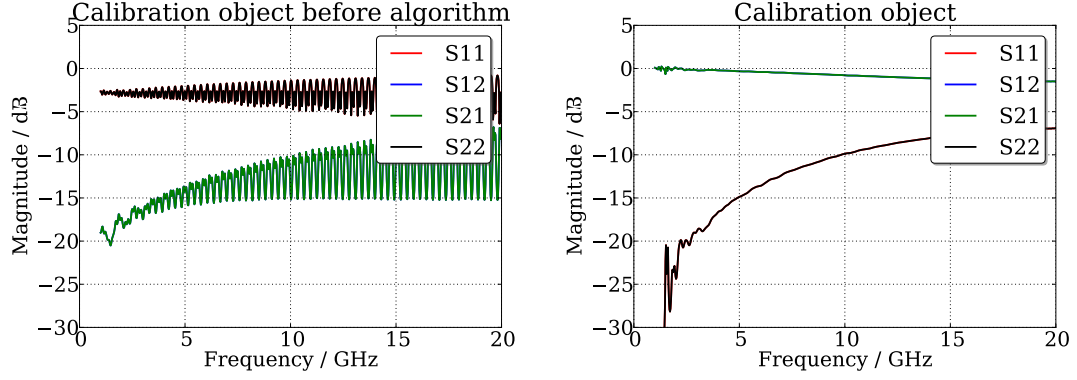


Figure A.14: Once the error networks have been characterized one can remove the sample used during calibration and insert another sample.

A.3 Parallel plates



(a) The scattering parameters for the object in the middle position.

(b) The scattering parameters for the object after self-calibration.

Figure A.15: The self-calibration object before and after the procedure.

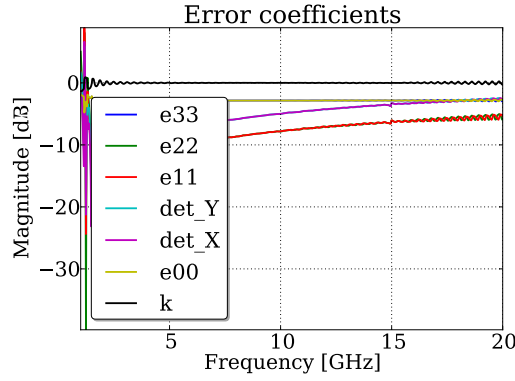


Figure A.16: The error coefficients.

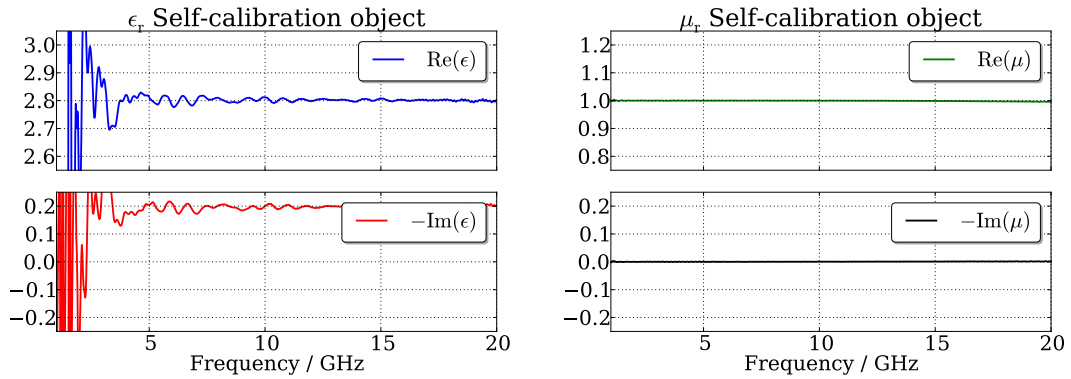


Figure A.17: The relative permittivity and permeability with the LNN algorithm. A parallel plate waveguide setup simulated (2D) in COMSOL and no white noise added.

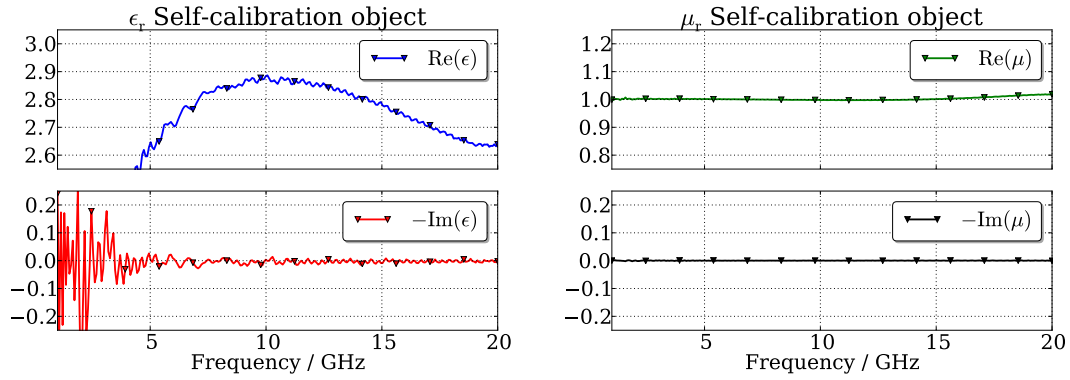


Figure A.18: The relative permittivity and permeability with the LNN algorithm. A parallel plate waveguide setup simulated (2D) in COMSOL and no white noise added. But in this calibration the L standard varies ($l_1 \neq l_2$).

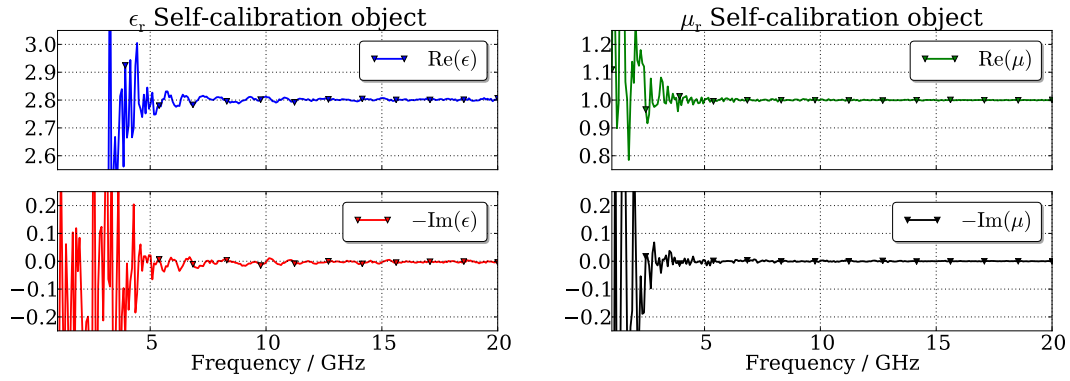


Figure A.19: The relative permittivity and permeability with the LNN algorithm. A parallel plate waveguide setup simulated (2D) in COMSOL then numeric white noise added.

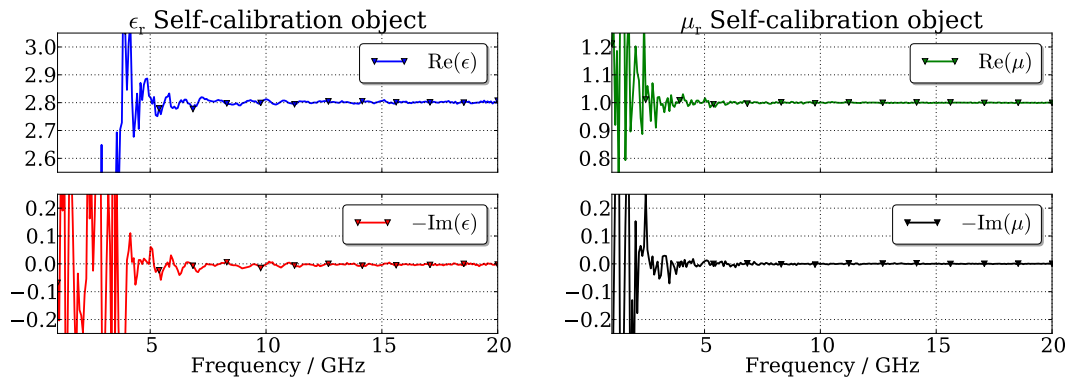


Figure A.20: The relative permittivity and permeability with the LNN algorithm. In this pair of plots the a-priori information on ϵ_r is 20% off and white noise added.

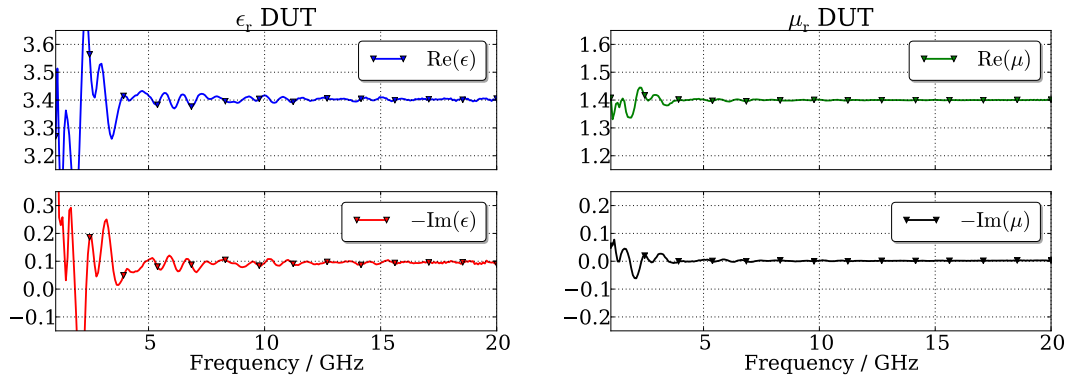


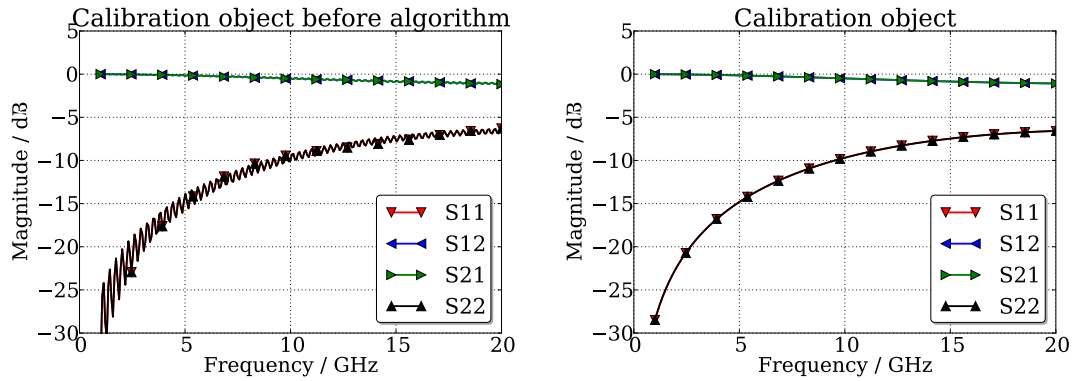
Figure A.21: Once the error networks have been characterized one can remove the sample used during calibration and insert another sample.

B

Extended LNN

This appendix contains all results for the Extended LNN algorithm. The algorithm was applied on three different, simulated setups; a straight coaxial fixture, a tapered coaxial fixture and a parallel plate waveguide (presented in detail in chapters 6 and 7).

B.1 Straight coaxial cable or fixture



(a) The scattering parameters for the object in the middle position.

(b) The scattering parameters for the object after self-calibration.

Figure B.1: The self-calibration object before and after the procedure.

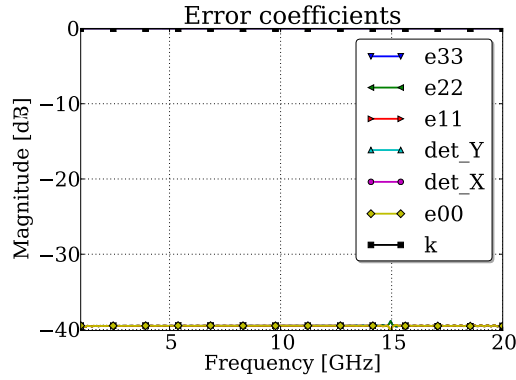


Figure B.2: The error coefficients.

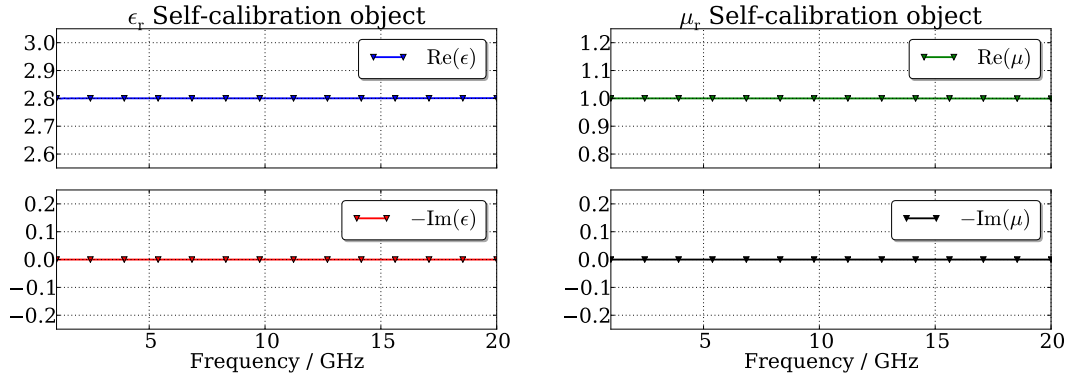


Figure B.3: The relative permittivity and permeability with the Extended LNN algorithm. A 1 m long straight coaxial waveguide setup simulated (full 3D) in COMSOL and no white noise added.

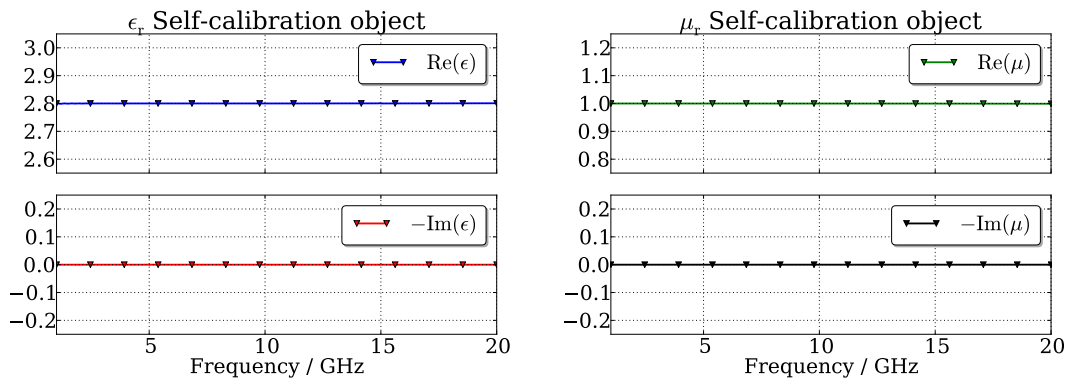


Figure B.4: The relative permittivity and permeability with the Extended LNN algorithm. A 1 m long straight coaxial waveguide setup simulated (full 3D) in COMSOL and no white noise added. But in this calibration the L standard varies ($l_1 \neq l_2$).

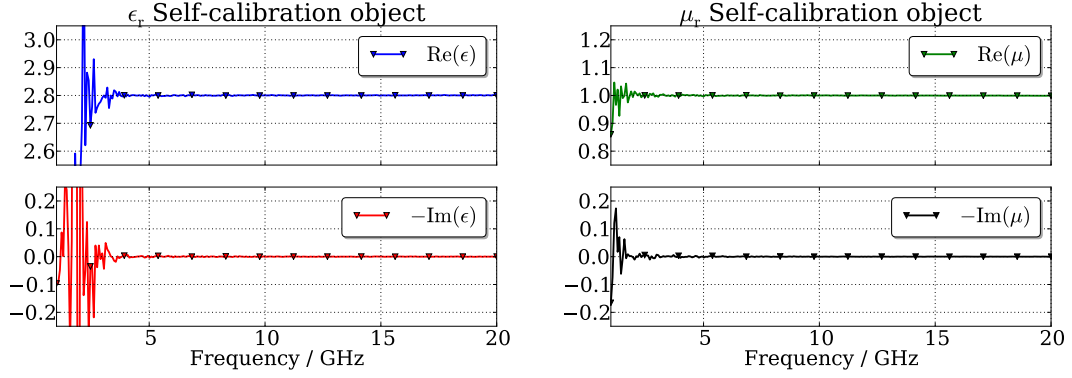


Figure B.5: The relative permittivity and permeability with the Extended LNN algorithm. A 1 m long straight coaxial waveguide setup simulated (full 3D) in COMSOL then numeric white noise added.

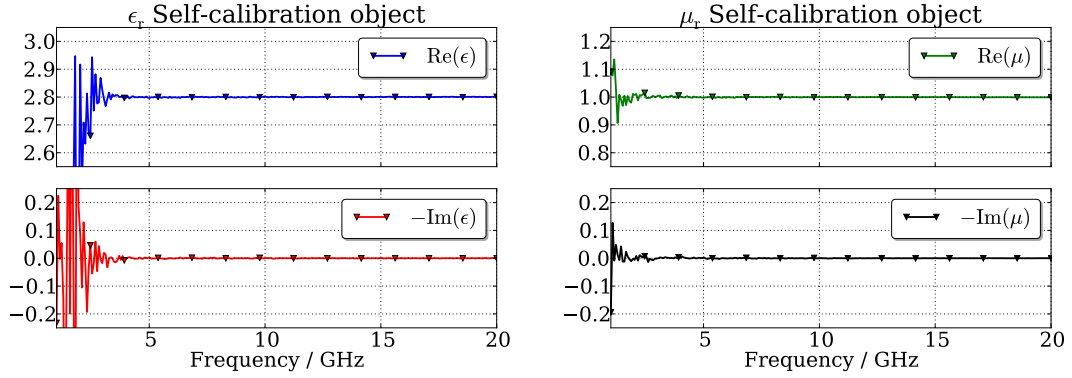


Figure B.6: The relative permittivity and permeability with the Extended LNN algorithm. A 1 m long straight coaxial waveguide setup simulated (full 3D) in COMSOL. In this pair of plots the a-priori information on ϵ_r is 20% off and white noise added.

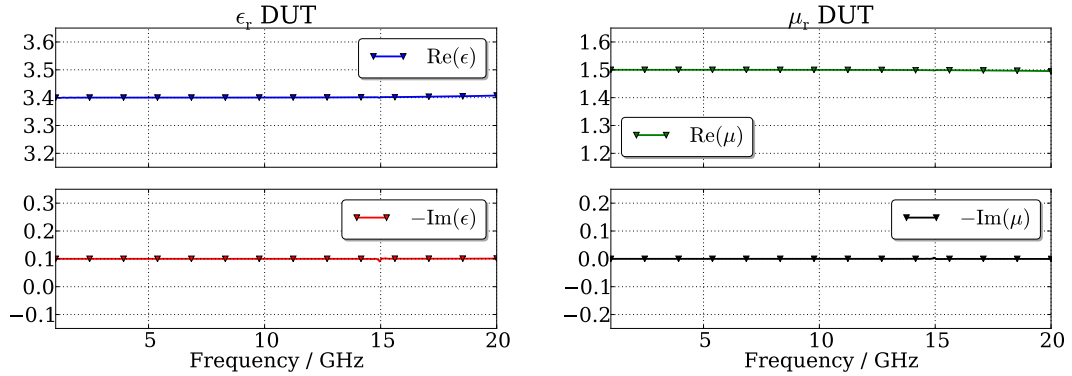


Figure B.7: Once the error networks have been characterized one can remove the sample used during calibration and insert another sample.

B.2 Tapered coaxial cable

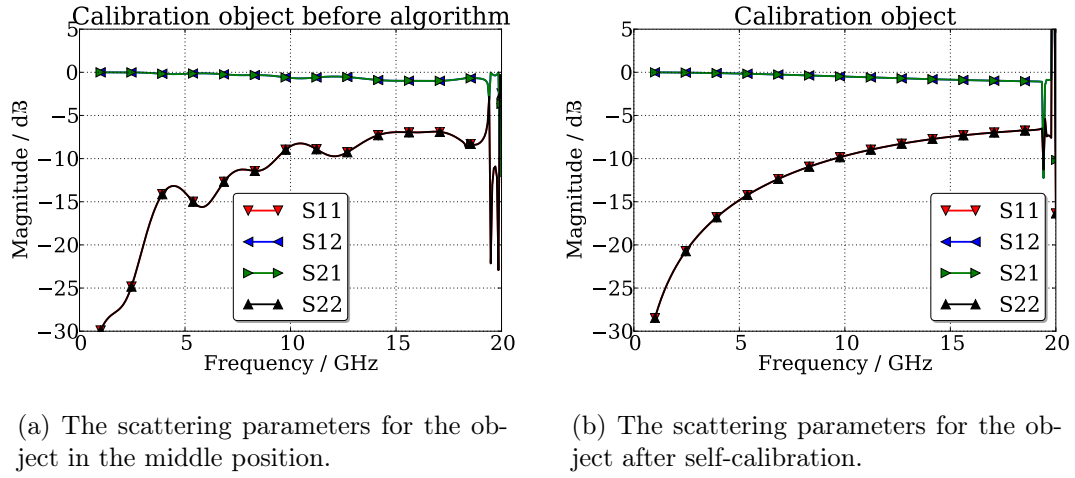


Figure B.8: The self-calibration object before and after the procedure.

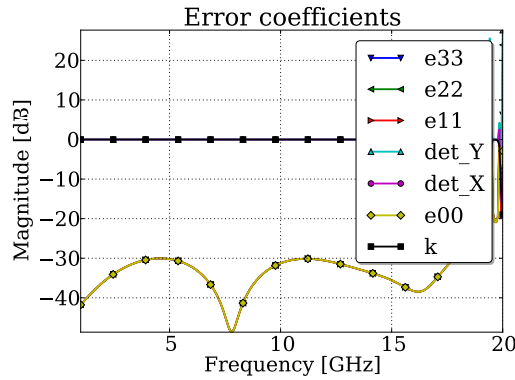


Figure B.9: The error coefficients.

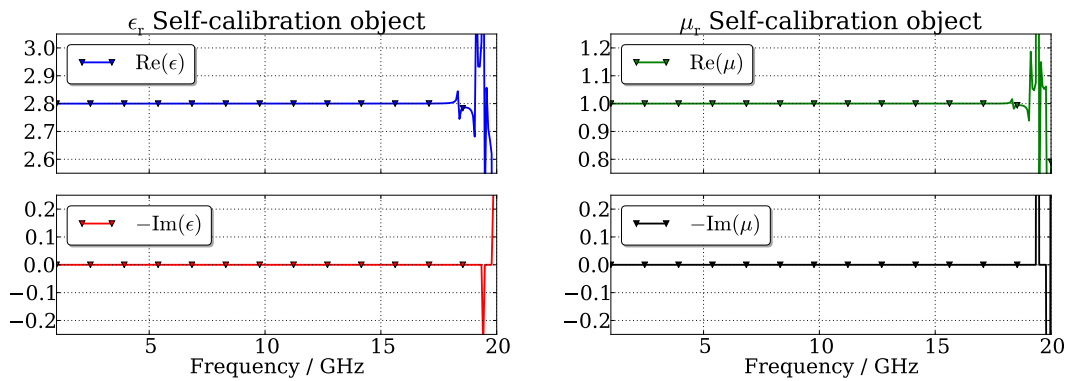


Figure B.10: The relative permittivity and permeability with the Extended LNN algorithm. A 11 cm long tapered coaxial waveguide setup simulated (full 3D) in COMSOL and no white noise added.

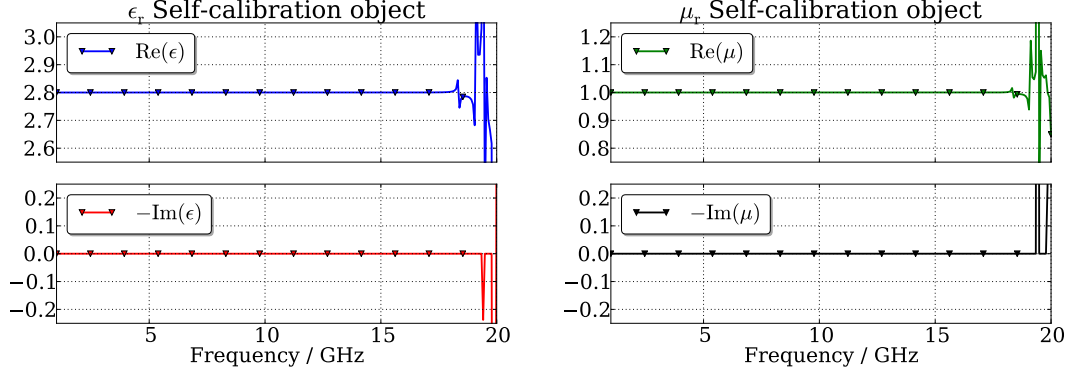


Figure B.11: The relative permittivity and permeability with the Extended LNN algorithm. A 11 cm long tapered coaxial waveguide setup simulated (full 3D) in COMSOL and no white noise added. But in this calibration the L standard varies ($l_1 \neq l_2$).

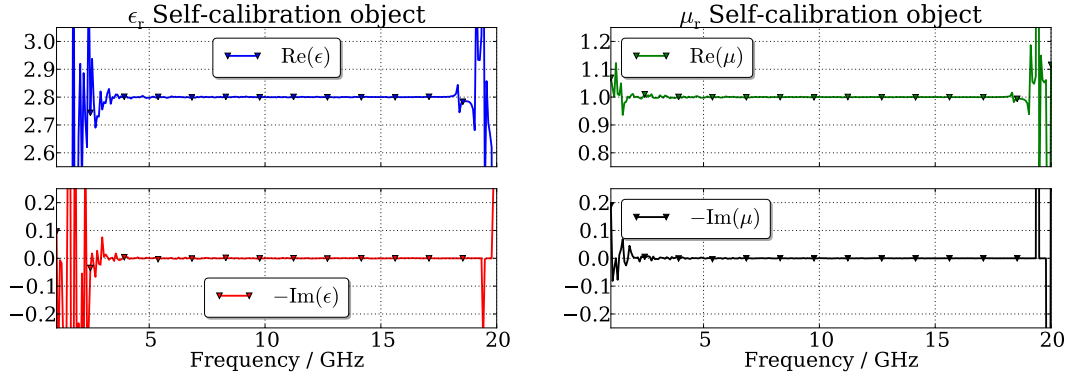


Figure B.12: The relative permittivity and permeability with the Extended LNN algorithm. A 11 cm long tapered coaxial waveguide setup simulated (full 3D) in COMSOL then numeric white noise added.

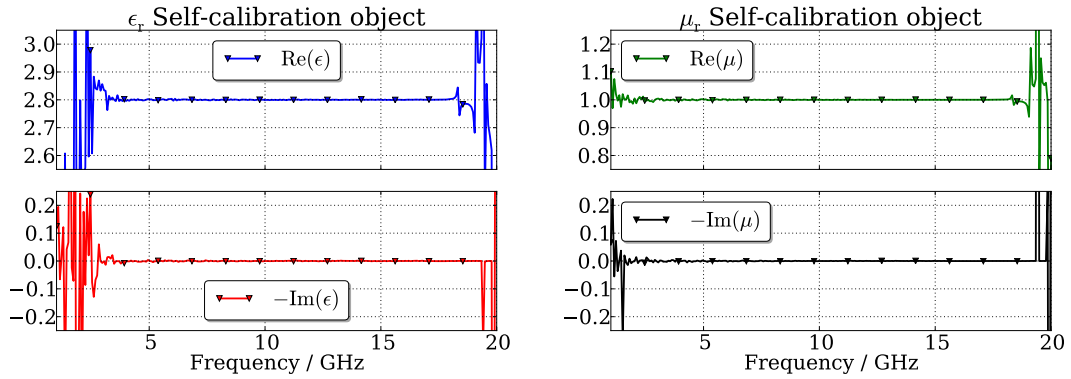


Figure B.13: The relative permittivity and permeability with the Extended LNN algorithm. A 11 cm long tapered coaxial waveguide setup simulated (full 3D) in COMSOL. In this pair of plots the a-priori information on ϵ_r is 20% off and white noise added.

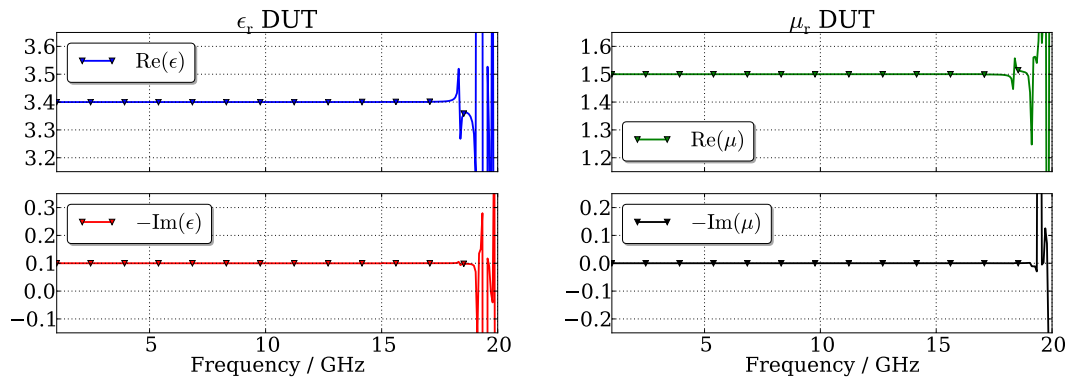
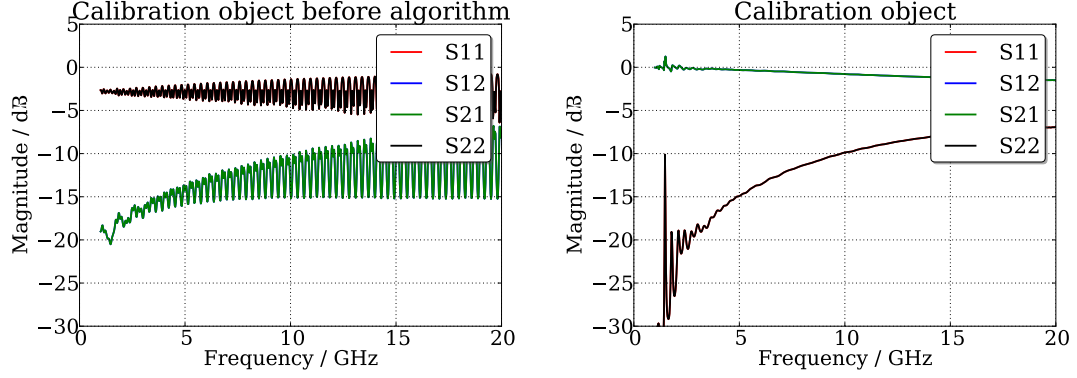


Figure B.14: Once the error networks have been characterized one can remove the sample used during calibration and insert another sample.

B.3 Parallel plates



(a) The scattering parameters for the object in the middle position.

(b) The scattering parameters for the object after self-calibration.

Figure B.15: The self-calibration object before and after the procedure.

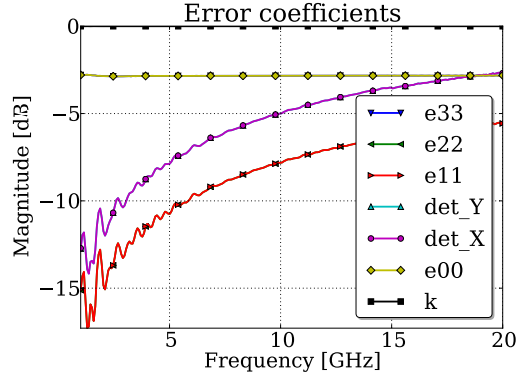


Figure B.16: The error coefficients.

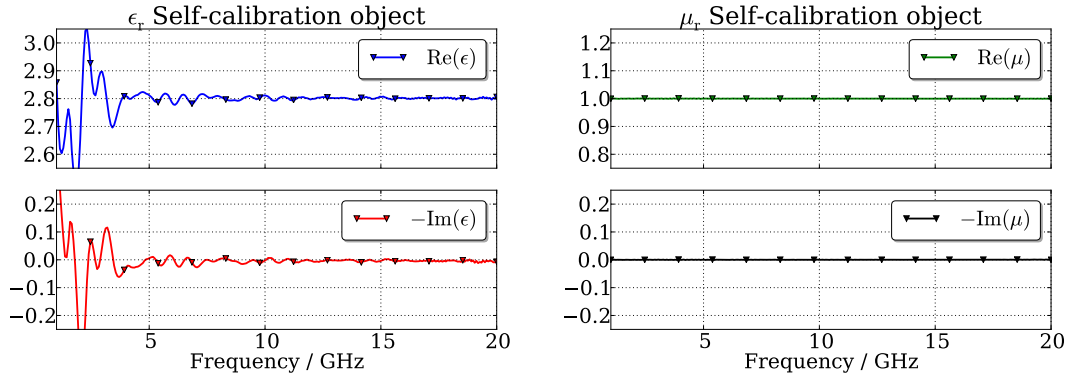


Figure B.17: The relative permittivity and permeability with the Extended LNN algorithm. A parallel plate waveguide setup simulated (2D) in COMSOL and no white noise added.

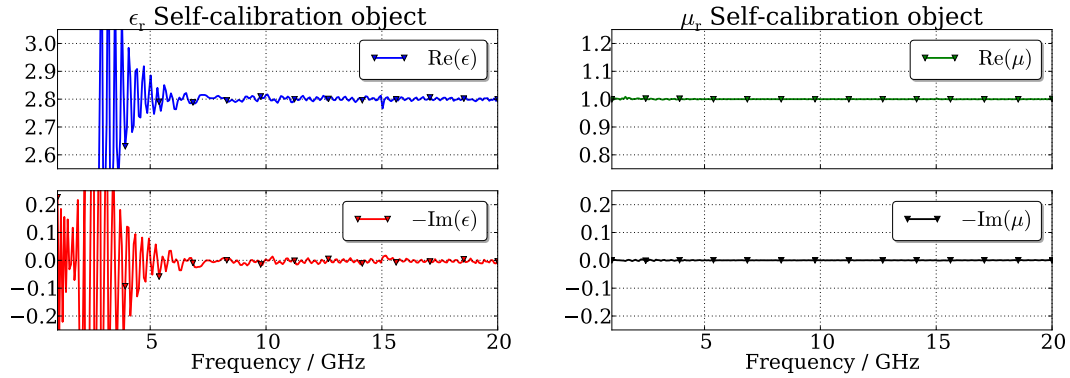


Figure B.18: The relative permittivity and permeability with the Extended LNN algorithm. A parallel plate waveguide setup simulated (2D) in COMSOL and no white noise added. But in this calibration the L standard varies ($l_1 \neq l_2$).

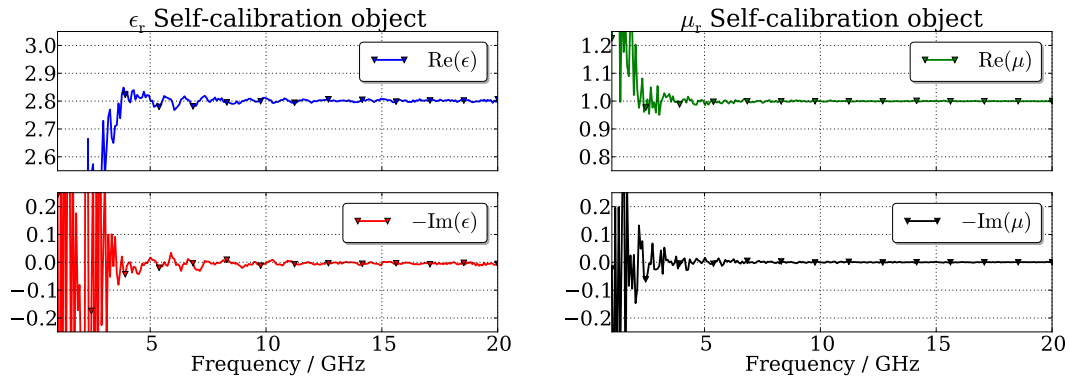


Figure B.19: The relative permittivity and permeability with the Extended LNN algorithm. A parallel plate waveguide setup simulated (2D) in COMSOL then numeric white noise added.

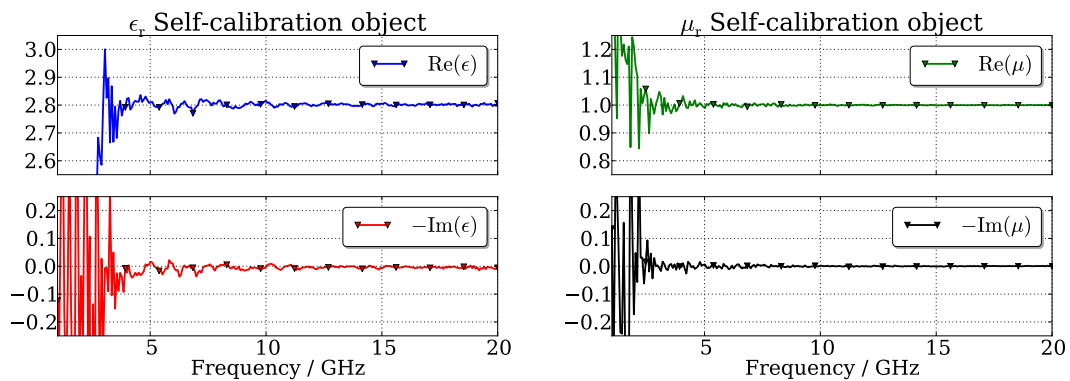


Figure B.20: The relative permittivity and permeability with the Extended LNN algorithm. In this pair of plots the a-priori information on ϵ_r is 20% off and white noise added.

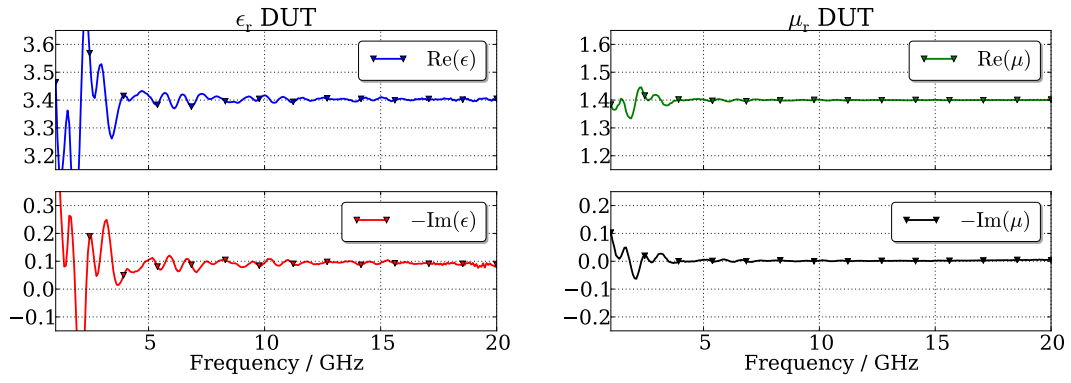


Figure B.21: Once the error networks have been characterized one can remove the sample used during calibration and insert another sample.

This appendix contains all results for the TTN algorithm. The algorithm was applied on three different, simulated setups; a straight coaxial fixture, a tapered coaxial fixture and a parallel plate waveguide (presented in detail in chapters 6 and 7).

C.1 Straight coaxial cable or fixture

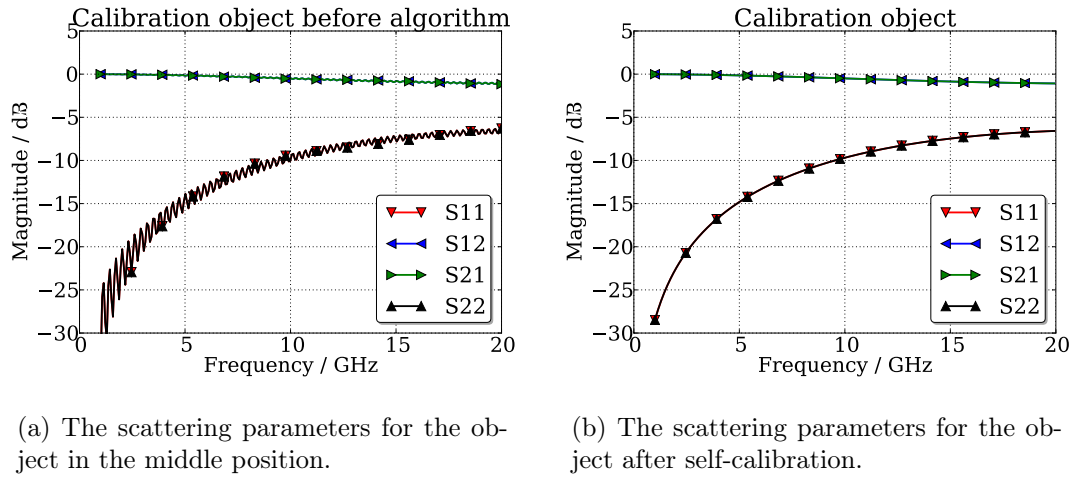


Figure C.1: The self-calibration object before and after the procedure.

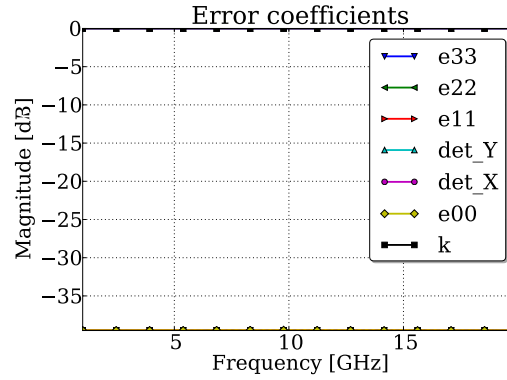


Figure C.2: The error coefficients.

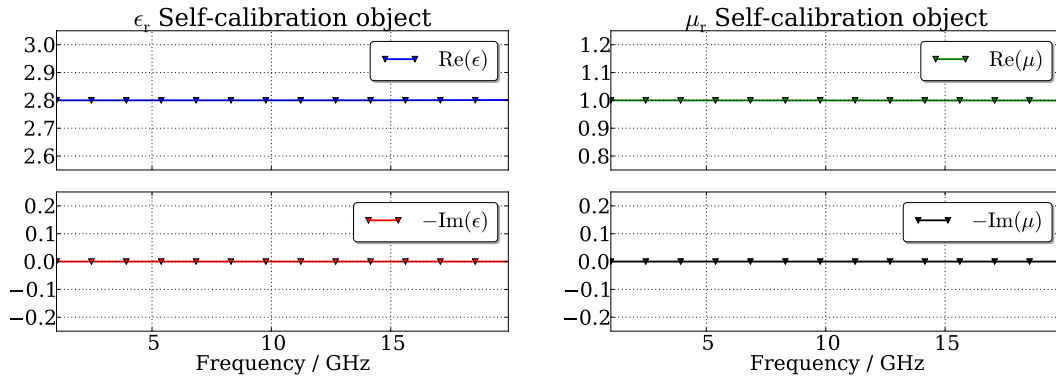


Figure C.3: The relative permittivity and permeability with the TTN algorithm. A 1 m long straight coaxial waveguide setup simulated (full 3D) in COMSOL and no white noise added.

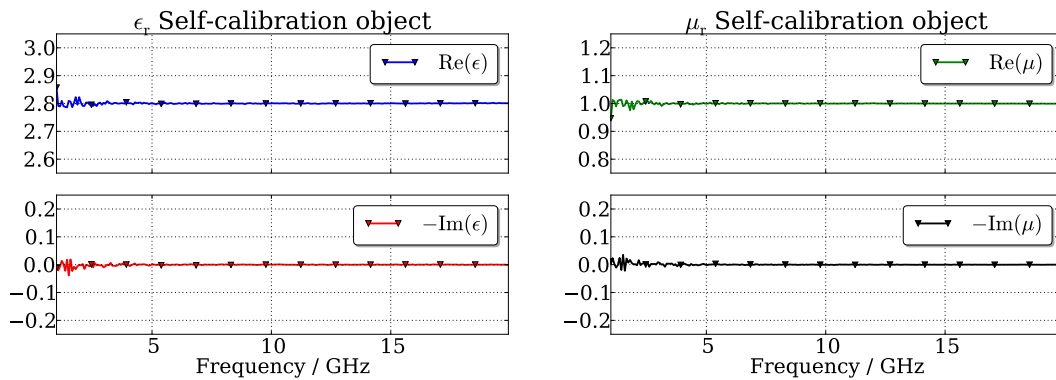


Figure C.4: The relative permittivity and permeability with the TTN algorithm. A 1 m long straight coaxial waveguide setup simulated (full 3D) in COMSOL then numeric white noise added.

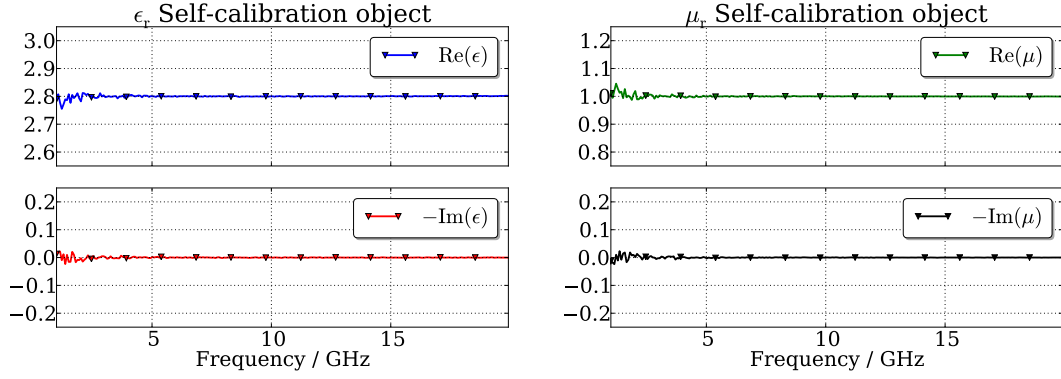


Figure C.5: The relative permittivity and permeability with the LNN algorithm. A 1 m long straight coaxial waveguide setup simulated (full 3D) in COMSOL. In this pair of plots the a-priori information on ϵ_r is 20% off and white noise added.

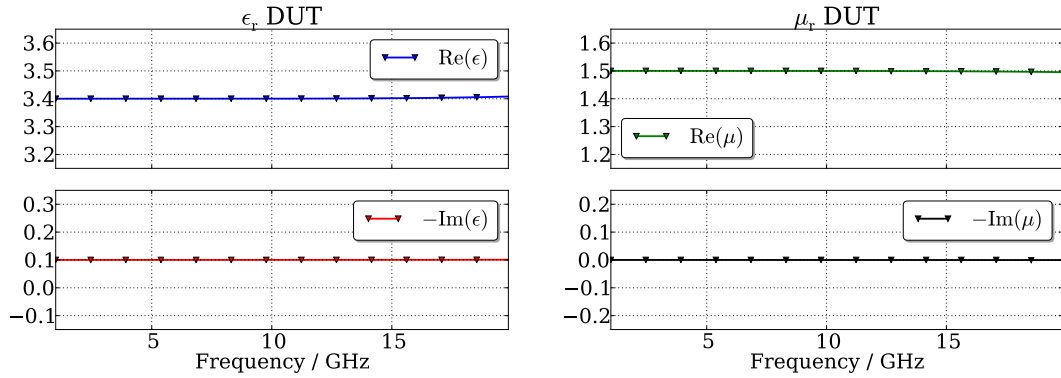


Figure C.6: Once the error networks have been characterized one can remove the sample used during calibration and insert another sample.

C.2 Tapered coaxial cable

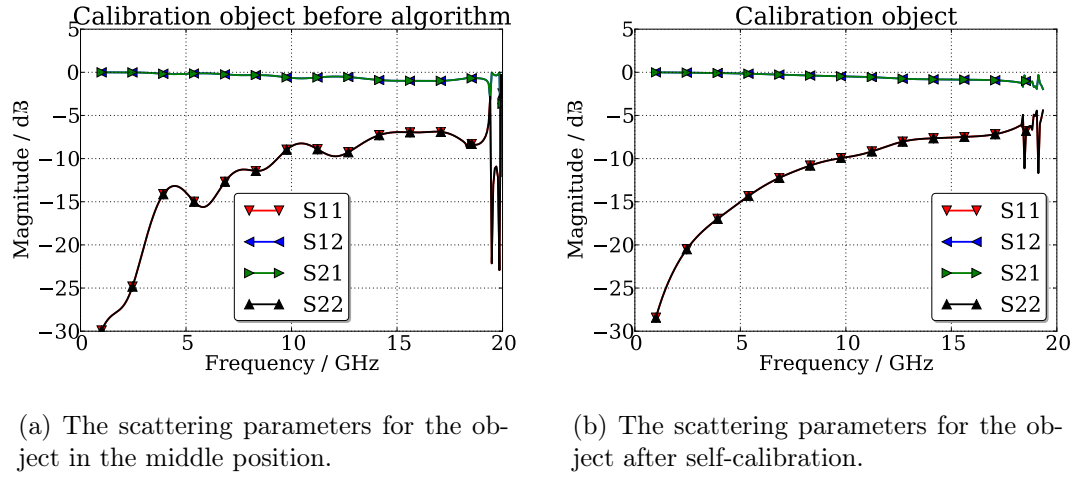


Figure C.7: The self-calibration object before and after the procedure.

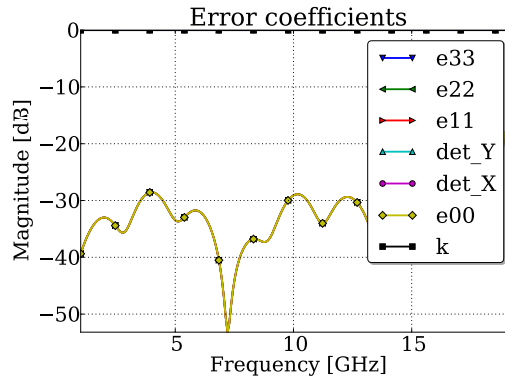


Figure C.8: The error coefficients.

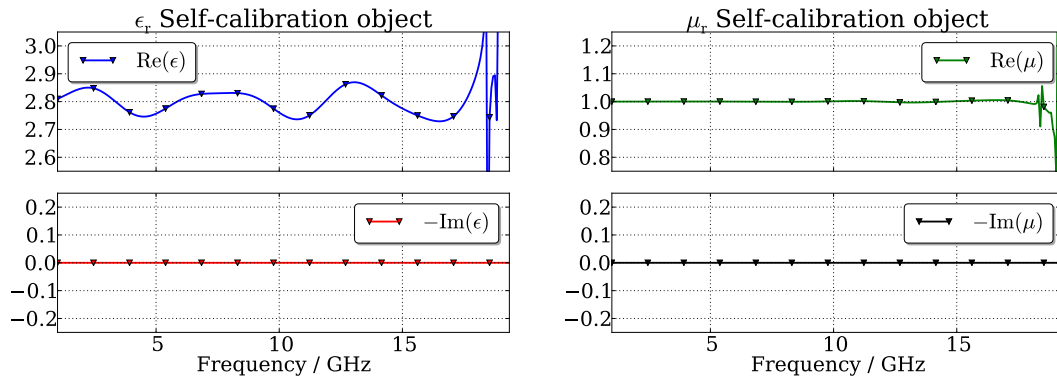


Figure C.9: The relative permittivity and permeability with the TTN algorithm. A 11 cm long tapered coaxial waveguide setup simulated (full 3D) in COMSOL and no white noise added.

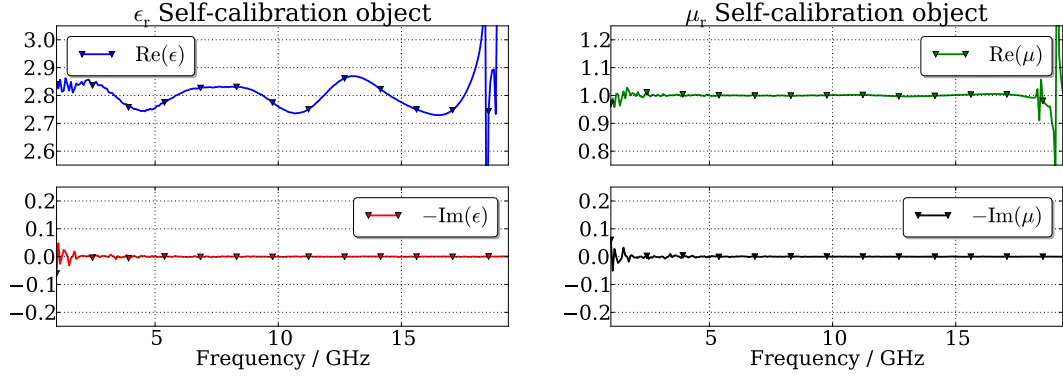


Figure C.10: The relative permittivity and permeability with the TTN algorithm. A 11 cm long tapered coaxial waveguide setup simulated (full 3D) in COMSOL then numeric white noise added.

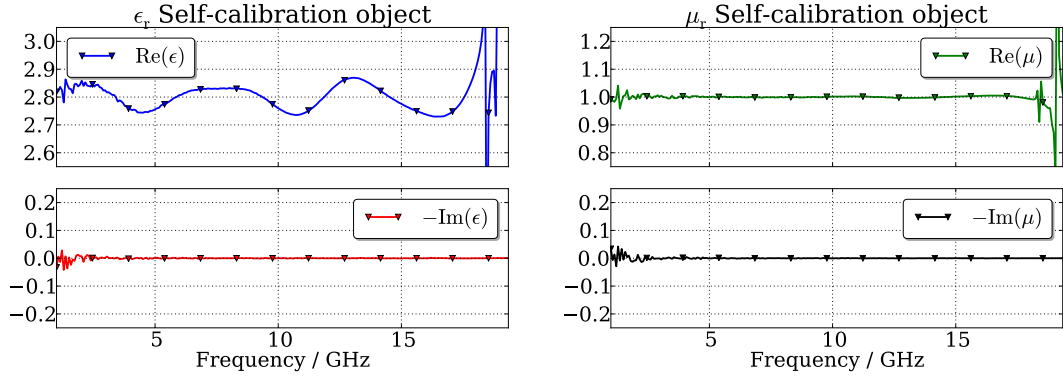


Figure C.11: The relative permittivity and permeability with the TTN algorithm. A 11 cm long tapered coaxial waveguide setup simulated (full 3D) in COMSOL. In this pair of plots the a-priori information on ϵ_r is 20% off and white noise is added.

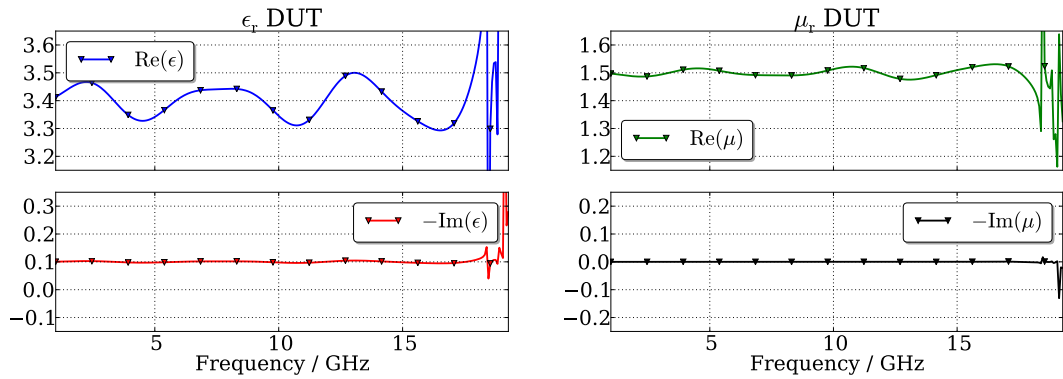


Figure C.12: Once the error networks have been characterized one can remove the sample used during calibration and insert another sample.

C.3 Parallel plates

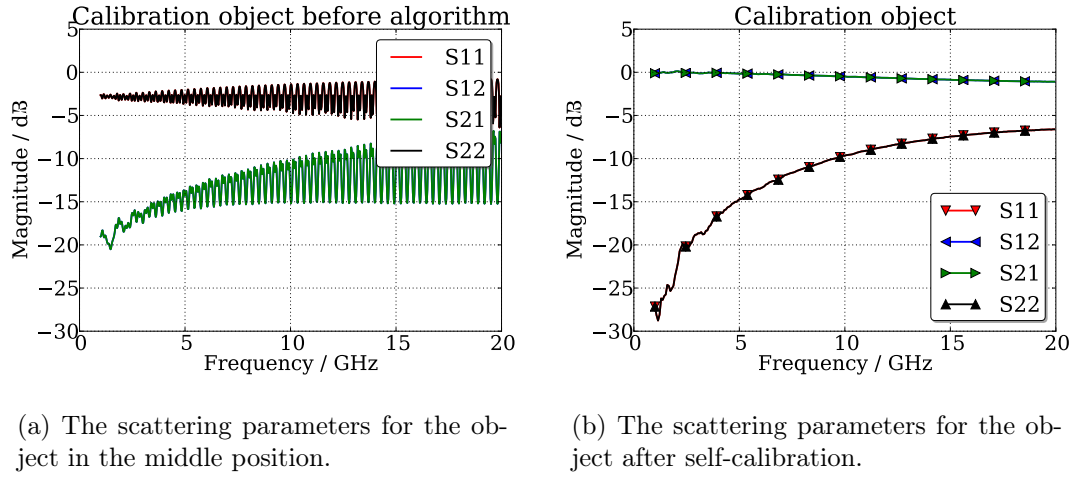


Figure C.13: The self-calibration object before and after the procedure.

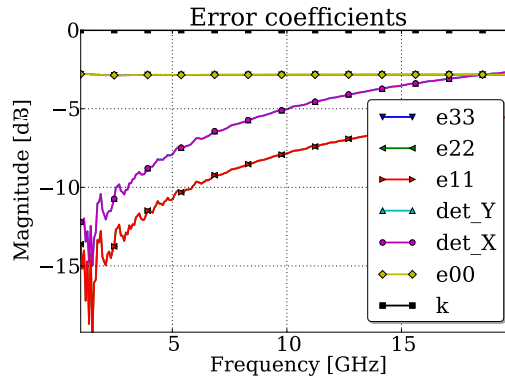


Figure C.14: The error coefficients.

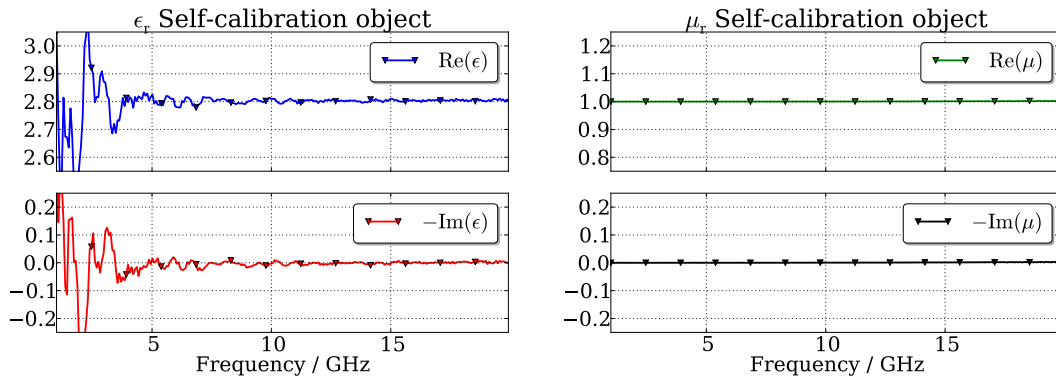


Figure C.15: The relative permittivity and permeability with the TTN algorithm. A parallel plate waveguide setup simulated (2D) in COMSOL and no white noise added.

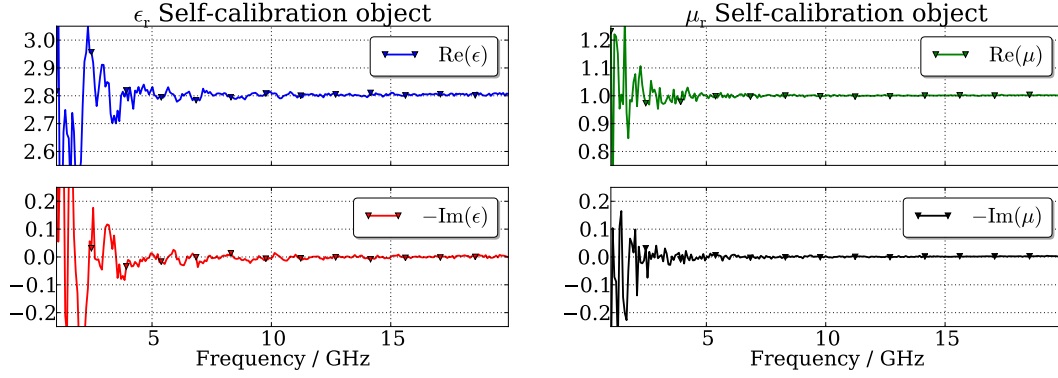


Figure C.16: The relative permittivity and permeability with the TTN algorithm. A parallel plate waveguide setup simulated (2D) in COMSOL then numeric white noise added.

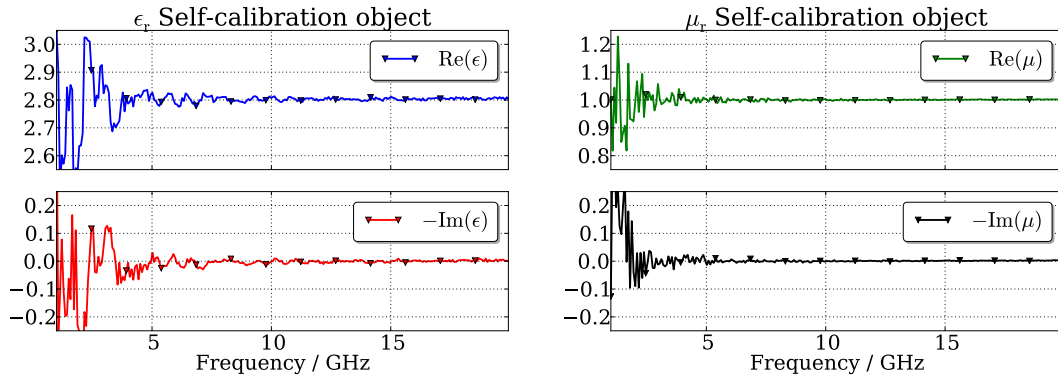


Figure C.17: The relative permittivity and permeability with the TTN algorithm. In this pair of plots the a-priori information on ϵ_r is 20% off and white noise is added.

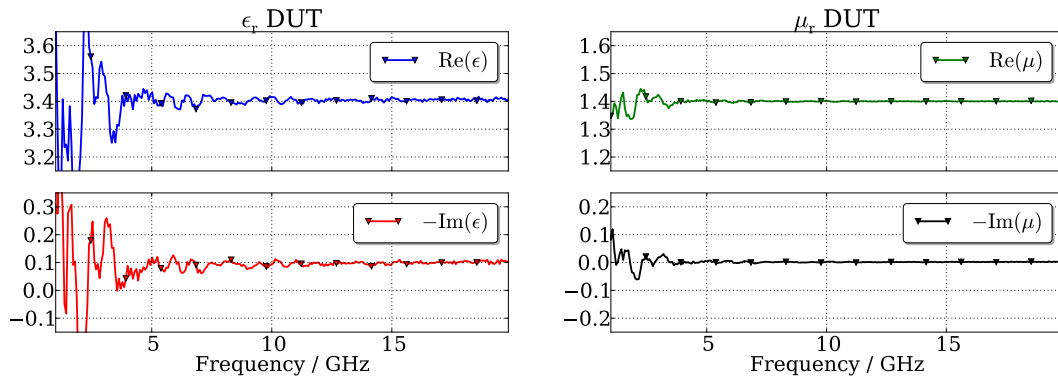


Figure C.18: Once the error networks have been characterized one can remove the sample used during calibration and insert another sample.